SYNCHROTRON RADIATION INLINE PROPAGATION BASED PHASE CONTRAST COMPUTERIZED TOMOGRAPHY (PC-CT) OF HUMAN PROSTATE SAMPLE

A Thesis Submitted to the College of

Graduate and Postdoctoral Studies

in Partial Fulfillment of the Requirements

for the Degree of Master of Science

in the Department of Animal and Poultry Science

University of Saskatchewan

Saskatoon

By

Subash Dhakal

PERMISSION TO USE

In presenting this thesis in partial fulfillment of the requirements for a Postgraduate degree from the University of Saskatchewan, I agree that the Libraries of this University may make it freely available for inspection. I further agree that permission for copying of this thesis in any manner, in whole or in part, for scholarly purposes may be granted by the professor who supervised my thesis work, and the College of Graduate and Postdoctoral Studies or, in their absence, by the Head of the Department or the Dean of the College in which my thesis work was done. It is understood that any copying or publication or use of this thesis or parts thereof for financial gain shall not be allowed without my written permission. It is also understood that due recognition shall be given to me and to the University of Saskatchewan in any scholarly use which may be made of any material in my thesis.

Requests for permission to copy or to make other use of material in this thesis in whole or part should be addressed to:

Dean of the College of Graduate and Postdoctoral Studies
University of Saskatchewan
116 Thorvaldson Building, 110 Science Place
Saskatoon, Saskatchewan, S7N 5C9, Canada

Or

Head of the Department of Animal and Poultry Science
College of Agriculture and Bioresources
51 Campus Drive
University of Saskatchewan
Saskatoon, SK S7N 5A8 Canada

ABSTRACT

The human prostate is an accessory male reproductive gland located below the neck of the urinary bladder. Benign prostatic hyperplasia (BPH) and prostate cancer are the frequently encountered pathological conditions of the prostate. It is estimated that 50% of men will develop BPH by age 50 with the incidence increasing to 90% by age 90. Prostate cancer is the second most common cause of cancer in men worldwide after lung cancer. In this study, we examined the ability of synchrotron radiation propagation phase-contrast computerized tomography (PC-CT) in comparison to ultrasound (US), magnetic resonance imaging (MRI) and histology, to characterize and differentiate various structural features and pathological lesions in 61 prostate tissues from 13 human patients collected during trans-urethral resection of the prostate. We compared the PC-CT, MRI, US and histology images of the same tissues from the same plane to determine if different structures like blood vessels, dilated acini etc. could be observed with each modality. The PC-CT was found to be a powerful imaging technique compared to MRI and US in identifying and resolving small structures located near each other. With PC-CT imaging, the same structures could be correctly identified almost 4 times and 15 times more often than MRI and US respectively. While comparing the ability to identify and resolve the nearby structures in PC-CT images reconstructed from 100%, 50% and 25% of the number of total projections collected (i.e. 2250 projections over 180 degree rotation of a sample on imaging stage), the ranking was as follows: 100% PC-CT>50% PC-CT>25% PC-CT ($p<0.05$). Radiation data recorded during a previous study while imaging dog cadavers with PC-CT were also analyzed. It was found that the average effective radiation dose imparted in a medium-sized dog during PC-CT imaging of one view of 7.8 mm height with 2000 projections in the biomedical imaging and therapy – insertion device (BMIT-ID) beamline of Canadian light source (CLS) beamline was 1,481.7 mSv, which is very high compared to the standard clinical CT examination deposits in human clinical medicine. The dose could be reduced by performing sparse view imaging i.e. 50% projection PC-CT or 25% projection PC-CT, but these amounts are still hazardous, such that a similar protocol used in human would have the potential to induce cancer later in life in approximately 0.5 % of the patients. For PC-CT imaging of human prostate *in situ*, a human positioning device was also designed. Due to the limitation in the weight-bearing capacity of the stage in the beamline, the positioning device was designed to be able to hold only a human pelvis or pelvis phantom up to 50 kg of weight in an

upright position. The results from this work demonstrate that the synchrotron radiation-based inline PC-CT is a promising technique that offers closer-to-histology grade non-invasive diagnostic imaging of prostate tissue. Further study in conducting in-vivo prostate imaging to reduce the radiation dose is the next step to move forward in this direction.

ACKNOWLEDGEMENTS

This thesis is the conclusion of a collective effort from many individuals who I wish to duly acknowledge for their valuable contributions and the inspiration for me in the pursuit of knowledge along the way.

Foremost, I would like to thank God, who has given me this beautiful life.

I express my sincere gratitude to my co-supervisors Dr. Mary Buhr and Dr. Ahmad Al-Dissi along with my advisors Dr. Murray Pettitt and Dr. Sheldon Wiebe for their continuous support and valuable guidelines throughout the period of study. Dr. Fiona Buchanan, my graduate chair, was also equally involved in providing me creative comments and guidance.

I would also like to thank the University of Saskatchewan prostate research team, Dr. Elisabeth Snead, Dr. Jaswant Singh, Dr. Rajni Chibbar, Dr. Ali El-Gayed, and Dr. Kishore Visvanathan for their very constructive ideas and continuous guidance and effort in making the work successful. Their lifelong research experience and subject-specific knowledge really helped me for smooth experimentation and analysis.

I am grateful for the engineers from RMD engineering Inc. for their input in helping me design the pelvis holder. A huge thanks to brilliant scientists at the Canadian light sources, Dr. Adam Webb, Dr. Ning Zhu, Dr. Dean Chapman, and Dr. Sergey Gosilov for their technical support and also for teaching me the synchrotron from the basics to the point of making me run the imaging and data analysis myself.

Thanking the people who were involved in this work, I can't stay without giving my gratitude to Dr. Sarah Parker for her help as a statistician. It would have been almost impossible to detangle the data without her expertise and help.

This research would not have been possible without the financial support from the SHRF through the SHRF Phase 2 Grant. I duly express my gratitude. Finally, I would like to express my sincere thanks to all the family members and friends. This research would not have been successful without their support, love, suggestions and encouraging statements.

TABLE OF CONTENTS

LIST OF TABLES

LIST OF FIGURES

COMMONLY USED ABBREVIATIONS

ADT – Androgen deprivation therapy

BM – Bending magnet

BMIT - Biomedical imaging and therapy

BOO – Bladder outlet obstruction

BPH – Benign prostatic hyperplasia

CCD – Charge-coupled device

CLS – Canadian Light Source

CMOS – Complementary metal-oxide-semiconductor

CT – Computerized tomography

DEI – Diffraction enhanced imaging

DRE – Digital rectal examination

FBP – Filtered back projection

Gy/mGy – Gray/milligray

ID – Insertion Device

PC-CT – Inline propagation phase-contrast computerized tomography

keV – Kilo-electronvolt

LUTS – Lower urinary tract syndrome

MHz- Megahertz

mpMRI- Multiparametric magnetic resonance imaging

MRI – Magnetic resonance imaging

PSA – Prostate-specific antigen

SD – Standard deviation

SDD – Sample to detector distance

SEM – Standard error of the mean

SHRF – Saskatchewan health research fund

Sv/mSv - Sievert/millisievert

TRUS – Transrectal ultrasound

TURP – Trans-urethral resection of the prostate

US – Ultrasonography

WCVM – Western College of Veterinary Medicine

1. Introduction

The human prostate gland is an accessory male reproductive gland located below the neck of the urinary bladder surrounding the most proximal part of the urethra. This tubulo-alveolar prostate gland secretes a slightly alkaline fluid, which helps to nourish as well as to transport the sperm with the help of its smooth muscle contractions during ejaculation. Prostatitis, benign prostatic hyperplasia and prostate cancer are the most frequently encountered pathological conditions of the prostate. It is estimated that 50% of men will develop BPH by age 50 with the incidence increasing to 90% by age 90 (Berry et al., 1984). Prostate cancer is the second most common cause of cancer in men after lung cancer and fifth leading cause of death worldwide (Bray et al., 2018). In Canada, prostate cancer is the most common cancer found in men. Out of all cancer related death, prostate cancer death represents 10.6%. Most of the prostate cancer cases (98%) and almost all prostate cancer death (99%) are found in men with age more than 50 years% (Government of Canada, 2019).

Histology is considered the gold standard method to achieve an accurate diagnosis of prostate cancer but requires obtaining multiple invasive core biopsies with risky complications such as bleeding, infection, pain in the hypogastrium, perineum or urethra as well as urethral obstruction due to blood clots or post-biopsy prostate swelling, which often require multiple urethral catheterization. Therefore, histological examination is only done in the patients who are suspected of having prostate cancer based on non-invasive diagnostic techniques such as examining prostate-specific antigen (PSA) levels in blood and medical imaging like ultrasound (US) and magnetic resonance imaging (MRI). However, each of the above techniques have considerable limitations rendering low diagnostic accuracy.

PSA level is elevated in prostate cancer (Cooner et al., 1990). However, elevated PSA level is also detected in some other conditions like prostatic inflammation, BPH, after recent digital examination and after ejaculation (Herschman et al., 1997; Lee et al., 2012; Sershon et al., 1994; Smith et al., 1996). Approximately 15% of prostate cancer cases are also missed with PSA screening (Thompson et al., 2004). Similarly, MRI has high sensitivity (93%; proportion of true positives out of all tested positive) but low specificity (41%; proportion of true negative out of all tested negative) and US has high specificity (96%) but low sensitivity (48%) (Ahmed et al., 2017).

So, the development of a superior non-invasive diagnostic imaging technique is immensely needed.

In a previous preliminary imaging study on ex-vivo whole dog prostates, we had found that synchrotron-based PC-CT resulted in better visualization of structure details compared to US, CT, and MRI, but not histology. However, in this study, we have applied PC-CT imaging to excised human prostate TURP (Trans Urethral Resection of Prostate) samples from BPH suspected patients to quantify the quality of the PC-CT images compared to US, MRI and histology. We didn't image our tissue samples with the conventional absorption-based CT because the CT images of the prostate glands from the previous study showed very limited amounts of detail. Moreover, the TURP tissue samples are believed to be too thin to absorb x-rays, so to produce useful image characteristics. We have also evaluated PC-CT imaging and image quality following reconstructing with a reduced number of projections (sparse view image reconstruction technique). This is important because imaging with a lower number of projections will reduce image acquisition time and radiation dose, which is critical for the transition towards the clinical application of the PC-CT. Radiation data previously collected by our team during PC-CT imaging of canine cadavers has also been evaluated to determine the radiation dose a cadaver receives during imaging and also to calculate the radiation dose that would be received during corresponding sparse-view imaging. Finally, a design has been developed for a human positioning device (pelvic holder) to hold a human pelvis or pelvis phantom with a real prostate inside it to image in the synchrotron to see how PC-CT images of a prostate inside a human body look like.

2. Literature review

1.1 Prostate gland anatomy, histology, and physiology

The human prostate gland is an accessory male reproductive gland located below the neck of the urinary bladder surrounding the most proximal part of the urethra (Figure 2.1). The gland is posterior to the pubic symphysis and anterior to the rectum (Bhavsar & Verma, 2014) making it accessible to digital rectal palpation for clinical examination. The tubulo-alveolar prostate gland secretes a slightly alkaline fluid which helps nourish and transport sperm during ejaculation (Hunter, 1968; Kumar & Majumder, 1995). In human beings the gland is a walnut-shaped structure with weight ranging from 7 to 16 grams (Leissner & Tisell, 1979). The gland consists of a base and an apex where the base is attached to the neck of the bladder and the apex lies on and is supported by the superior surface of the urogenital diaphragm. The prostate is encapsulated by an outer fibromuscular pseudo-capsule which is incomplete anteriorly at its apex (Ayala et al., 1989; Udeh, 1982). The invasion of this fibromuscular band by neoplastic cells is indicative of malignancy and is considered clinically significant (Ayala et al., 1989). The fibromuscular capsule sends off strands of connective tissue exteriorly which attach to peri-prostatic tissue structures (Ayala et al., 1989).

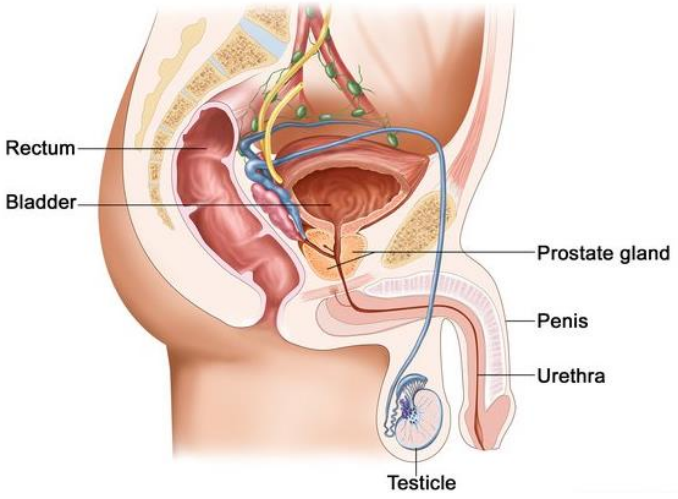

2.1 Schematic diagram showing the location of the prostate gland and its surrounding structure in sagittal section of human male body. (Source "Penile Anatomy-CTHP Image", March 2015. Retrieved from National Cancer Institute, on January 2019, https://visualsonline.cancer.gov/details.cfm?imageid=9988. Reprinted with permission.)

Blood is supplied to the prostate gland by the branches of the internal iliac artery and the gland receives innervation through the prostatic plexus. Lymph from the prostate mainly drains into the internal iliac and sacral lymph nodes (Bhavsar & Verma, 2014). Surgical removal of prostate cancer or the gland itself may affect the nerve supply to the bladder and penis eventually causing problems in urination and sexual function (Michaelson et al., 2008).

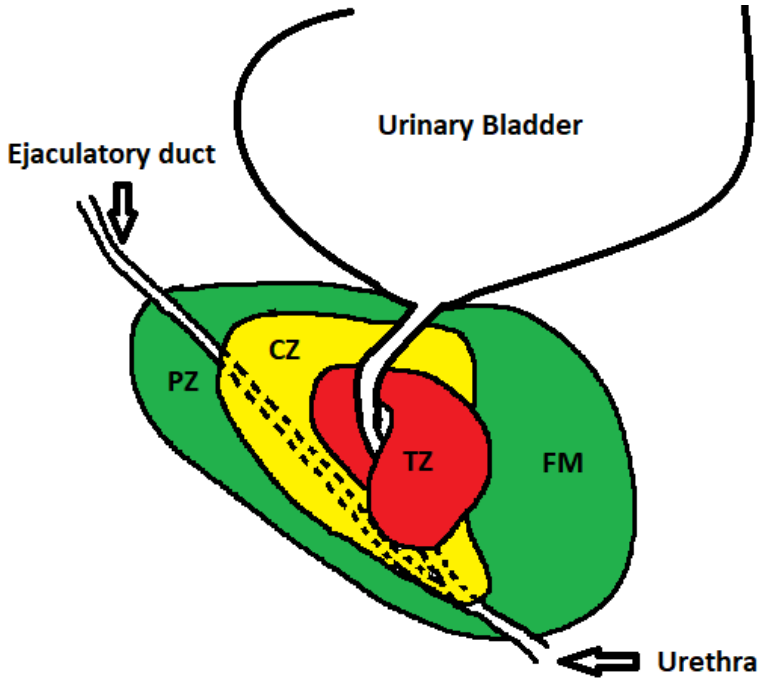

Figure 2.2 Schematic diagram showing different zones of human prostate gland. PZ: peripheral zone, CZ: central zone, TZ: transitional zone and FM: anterior fibromuscular zone (Dhakal Subash, 2019).

Histologically, the prostate gland is divided into four zones; transitional, central, peripheral and anterior fibromuscular (Figure 2.2) (McNeal, 1968). The first three are considered glandular zones and contain supportive stroma while the fourth is non-glandular and only contains fibromuscular stroma. The transitional zone is the most central part of the gland and surrounds the distal part of the pre-prostatic urethra. The central zone is the part of the prostate gland which encircles the ejaculatory ducts and contains 20-25% of the glandular mass of the prostate. The peripheral zone of the prostate gland is the largest comprising about 70-75% of the total glandular mass. This zone

is located on the posterior-lateral aspects of the gland and is the part which is palpated when a digital rectal examination is performed. The smallest zone of the prostate is the anterior fibromuscular zone which is devoid of glandular tissue and is comprised of fibrous connective tissue and smooth muscles (McNeal, 1968). These four zones not only have different embryological origin, anatomical location and biological function but are also susceptible to difference pathological conditions. Around 70% of all prostate cancer cases arise within the peripheral zone and the majority of BPH cases originate from the transitional zone (Lee et al., 2011).

The prostate contains an outer thin circular smooth muscle layer and an inner thick longitudinal smooth muscle layer that continue interiorly and blends with the fibromuscular stroma surrounding and supporting the glandular structures. (Udeh, 1982). There are around 30-50 tubulo-acinar glands within the prostate. This acini-duct system is lined by a layer of basal cells and a layer of secretory columnar epithelium of varying height which later becomes transitional epithelium at the entrance of the prostatic urethra (McNeal, 1988) (Figure 2.3).

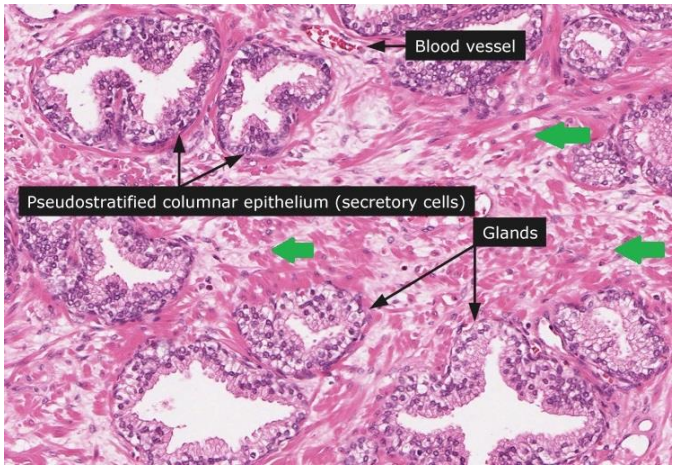

Figure 2.3 Histological image showing a microscopic view of the moral human prostate with clear visualization of fibromuscular stroma (green arrows), acini or glands, and epithelium. (Source "Prostate", Retrieved from The Human Protein Atlas, on January 2020, https://www.v19.proteinatlas.org/learn/dictionary/normal/prostate/detail+1 . Reprinted with permission.)

In humans, the prostate gland contributes 30% of the seminal fluid which not only helps nourish and transport the spermatozoa but also acts as a buffer against the adverse acidic environment of

the female genitalia. This prostatic secretion is rich in citric acid and zinc, the concentrations of which are 75 and 1000 times greater in prostatic fluid than plasma, respectively. The cells of the peripheral zone of the prostate are rich in these two components and are their main source in semen. (Franklin, et al., 2005a)

2.1.Pathological conditions of prostate gland

A prostate with a volume less than 30 cm^3 is considered normal. Prostatic volume can be calculated by measuring prostatic length, width and height utilizing transrectal ultrasound (TRUS) and using the formula:

Prostate size = 0.52 x length x width x height

A prostate with a volume larger than 30 cm^3 is considered to be exhibiting prostatomegaly (Gossner, 2012) which may be due to one of the following pathological conditions: prostatitis, benign prostatic hyperplasia, and prostate cancer. These conditions are the most frequently encountered pathological conditions of the prostate and are the most studied.

2.1.1. Prostatitis

Prostatitis is the inflammation of prostate gland and is classified into 4 different subtypes by the National Institute of Diabetes and Digestive and Kidney Diseases (Krieger et al., 1999). These are acute bacterial prostatitis, chronic bacterial prostatitis, chronic non-bacterial prostatitis/chronic pelvic pain syndrome and asymptomatic inflammatory prostatitis. The nature of pain and the duration of symptoms are often helpful in the initial diagnosis of prostatitis; however, additional tests are often required to confirm diagnosis such as bacterial culture and microscopic analysis of urine to identify bacteria and white blood cells (WBCs), respectively. The first two type of prostatitis, i.e. bacterial acute and chronic prostatitis are usually treated with antibiotics. The most common subtype of prostatitis is chronic non-bacterial prostatitis which represents ~95% of all prostatitis cases. This condition is difficult to diagnose clinically because of its vague symptoms. The diagnosis is also made after urine bacterial culture yields negative results (Krieger et al., 1999). Although it is recommend that antibiotic treatment be reserved for patients with bacterial prostatitis, it has been found that large number of prostatitis patients receive antibiotics (Collins et

al., 1998). The plasma level of prostate-specific antigen (PSA), a marker of prostate disease, often increases in all subtypes of prostatitis but the increase usually does not exceed twice the normal level (Potts, 2001).

2.1.2. Benign prostatic hyperplasia

Benign prostatic hyperplasia is a non-neoplastic condition resulting in increased prostatic size the incidence of which increases with age. The prevalence of BPH is around 8% in the 4th decade of life while it increases to around 50% in the 6th decade and is more than 90% in men older than 70 (Patel & Parsons, 2014). BPH most often arises from the transitional zone of the prostate gland and can result in the proliferation of glandular and stromal tissues with the former being more common. (Roehrborn, 2008; Wasserman, 2006). Budding and branching of the duct-acini system is the hallmark feature of glandular BPH. The hyperplastic gland has a bi-layered epithelial lining with outer cuboidal cells and inner tall columnar cells. In advanced stages of BPH basal cell hyperplasia of ducts and acini is seen which can be visualized utilizing basal cell specific stains (McNeal, 1965, 1988)

The exact cause of BPH is not known although it is widely accepted that androgens play an important role in the development of this condition (Banerjee et al., 2018). Historically double castration was a treatment option in men with BPH because the procedure often resulted in reduction of the size of the lesion. This effect was thought to be related to the loss of androgen stimulation after castration (White, 1895). Androgens, however, may not be the only factor contributing to the development of BPH since most elderly men affected by this condition have low androgen levels (Ho & Habib, 2011).

Despite not being a lethal condition, BPH can significantly reduce the quality of life in the elderly and results in high financial burden from continuous medical intervention. Clincally, BPH is known to result in a constellation of symptoms collectively known as the lower urinary tract syndrome (LUTS), which include difficulty voiding urine with patients reporting feeling the need to urinate frequently but with only little amount or weak stream of urine produced and waking up frequently at night to urinate. Dribbling of urine from the penis after urinating and blood in urine have also been described. More than 50% of BPH patients display LUTS symptoms particularly as they advance in age (McVary, 2006). These symptoms are all related to bladder outlet

obstruction (BOO) secondary to BPH (Jarvis et al., 2014) and are often accompanied with other symptoms such as abdominal pain and pain during micturition. Incomplete urination in turn often results in ascending bacterial urinary tract infections (Truzzi et al., 2008).

2.1.2.1.Diagnosis

The diagnosis of BPH is often based on history and clinical symptoms, physical examination and laboratory testing. If BPH is suspected based on clinical signs, digital rectal examination is performed to assess the size and contour of the prostate gland. A smoothly enlarged symmetric prostate is indicative of BPH while an asymmetric, firm nodular prostate is an indicative of malignancy (Kim et al., 2015).

Routinely used laboratory diagnostic tests for BPH include urinalysis and assessing the levels of PSA in the blood. Urinalysis in the suspected patient is for the evaluation of glucosuria, pyuria, and hematuria and is performed to help differentiate BPH from other possible causes of LUTS. Glucosuria, pyuria, and hematuria are suggestive of diabetes, urinary tract infection and urogenital malignancies respectively (Kim et al., 2015).

PSA is an androgen-regulated glycoprotein produced by the epithelial cells of the prostate gland. After its secretion into the glandular lumen, PSA helps liquefy the semen by cleaving two proteins; semenogelin I and II, responsible for semen coagulation. This in turn eases sperm motility allowing the sperm to swim more freely (Balk et al., 2003).

Normally, PSA is also present in the blood but in a very small amount, and less than or equal to 4 ng PSA/mL blood is considered as normal (Adams, 2013). Disruption of prostatic tissue structure allows leaking of PSA into systemic circulation in a larger amount and will be detected in blood PSA testing (Sardana & Diamandis, 2012). PSA levels rise in BPH cases, thus increased level of PSA will suggest BPH. But, PSA does increase in prostate cancer also, so it is really difficult to differentiate whether the elevation is due to BPH or prostate cancer (Sershon et al., 1994). PSA level also increases after the ejaculation (Herschman et al., 1997; Rajaei et al., 2013) and inflammation of prostate (Lee et al., 2012). Therefore, confirmation of BPH is not possible based only on PSA, but PSA is, of course, a very useful tool for the diagnosis of BPH when used with other techniques.

Other diagnostic tests which are not routinely performed include urine cytology, serum creatinine, trans-rectal ultrasound, post-void residual urine test, cystourethroscopy and urodynamic studies.

Although TRUS has the ability to determine the exact size of the prostate providing an accurate diagnosis of BPH, the technique is not routinely used because it is comparatively painful.

2.1.3. Prostate cancer

Prostate cancer can arise from the uncontrolled multiplication of glandular or stromal cells within the prostate with the former being most common representing 80% of diagnosed cases (Franz et al., 2013). Prostate cancer is the second most common cause of cancer worldwide. The majority of prostate cancer cases (around 99%) are diagnosed in men over 50 years old (Stewart & Wild, n.d.) and arise from the peripheral zone of the prostate (Oh et al., 2003)

Several genes and proteins have been found to be dysregulated in prostate cancer and these include Z1P1 protein (main zinc uptake transporter), PTEN gene (a tumor-suppressor gene), insulin-like growth factors I and II (IGF-I and -II) and epidermal growth factor (EGF) (Oh et al., 2003; Franklin et al., 2005a; Franklin et al., 2005b).

Androgens are thought to play an important role in the development of prostate cancer. Therefore, androgen deprivation therapy (ADT) is commonly used as a treatment option. ADT is performed through antiandrogen medications (androgen receptor blocker) or by chemical castration (androgen production suppressor) and was first introduced in 1941 with dramatic results (Huggins & Hodges, 1941). The use of ADT is, however, controversial, as the continued treatment results in cancer cells eventually becoming resistant after 2-3 years (Sharifi et al., 2005; Harris et al., 2009; Das, 2017).

Dietary habit, lifestyle exercise and genetics. have been found to be associated with the occurrence of prostate cancer (Anand et al., 2008). For example, men consuming a diet deficient in vitamin D or large quantities of red meat have a higher risk of developing prostate cancer (Wigle et al., 2008). Obesity is also a well-known risk factor for prostate cancer (Calle et al., 2003). Additionally, men with one first-degree relative affected by prostate cancer have a two-fold increase in the risk of

developing prostate cancer. The risk increases to fivefold if two first degree relatives are affected (Steinberg et al., 1990; Zhang et al., 2003).

Prostate cancer is a slow growing cancer with no or few symptoms in early stages. Clinical signs can vary among affected men but are often related to the effects of the tumor on the lower urinary tract, the dysfunction of which depends on the severity of and size of the tumor. Common clinical symptoms include difficulty in starting urination, burning sensation during urination, blood in urine and erectile dysfunction. When distant metastasis occurs, other clinical signs can appear related to the site of metastasis (Hamilton & Sharp, 2004; J. et al., 1998).

2.1.3.1.Diagnosis

The diagnosis of prostate cancer starts with the patient's clinical history and the assessment of clinical symptoms. This is later followed by digital rectal examination (DRE) through which the peripheral zone of the prostate (its outer portion) can be assessed by putting a finger inside the rectum. Finding an asymmetric, firm nodule in the prostate is suggestive of prostate cancer (Kim et al., 2015). It has been found that approximately 70% of all prostate cancer cases arise from the peripheral zone of the prostate, while only 20% and 10% arise from the transitional and central zones, respectively (C. H. Lee et al., 2011; Loch, 2007). The sensitivity of DRE in detecting prostate cancer is relatively low. One study reported that DRE could only detect 55.8% of prostate cancer cases (Schroder et al., 1998). The study also suggested that the positive predictive value and sensitivity of DRE are directly related to the PSA level. Another larger meta-analysis of several studies of men older than 50 years of age reported that the sensitivity, specificity, and positive predictive value of DRE was 53.2%, 83.6%, and 17.8% (Mistry & Cable, 2003).

The level of PSA in the blood is often assessed during the initial screening for prostate cancer. It has been suggested that a PSA level above 4.0 ng/ml is suggestive of prostate cancer (Cooner et al., 1990). However, blood PSA level is known to increase in other prostatic diseases and also with age (Wolff et al., 1999). In fact, it has been shown that only 25% of patients with elevated blood PSA level have prostate cancer (Ichael & Arry, 2001; Sardana & Diamandis, 2012). Despite the high PSA level, prostate cancer in asymptomatic patients may not progress at all or progresses in such a slow manner that a patient may remain asymptomatic for rest of his life (Moyer, 2012).

Prostate cancer has been diagnosed in men with normal or low blood PSA level. In fact, it is estimated that 15% of prostate cancer cases are diagnosed in patients with normal or even low blood PSA level (I. M. Thompson et al., 2004).

PSA velocity, PSA density, and complexed PSA (cPSA) to free PSA (fPSA) ratio can also be assessed in people suspected of having prostate cancer where an elevation of these parameters can be indicative of malignancy (Djavan et al., 1999; ElShafei et al., 2013; Jung et al., 2006).

Other non-invasive diagnostic modalities often pursued to diagnose prostate cancer include ultrasound and magnetic resonance imaging (MRI). However, histopathology is considered the gold standard method. Each of the three above diagnostic techniques will be discussed later in more depth. To date, synchrotron radiation phase contrast computerized tomography (PC-CT) has not been utilized to image the human prostate. PC-CT is the focus of this thesis and will be discussed at the end.

2.2.Non-invasive diagnostic techniques:

Trans-rectal ultrasound: This technique uses high-frequency sound wave emitted from a probe inserted inside the rectum facing the prostate. This technique is often performed after suspecting an abnormality in the prostate thorough DRE or after detecting a high PSA level in the blood. The shape and size of the prostate can be assessed accurately using TRUS but the technique has low sensitivity, specificity, and accuracy for the detection of prostate cancer and is often used to obtain a guided prostate biopsy (Harvey et al., 2012a). In most cases of prostate cancer (60-70%), hypoechoic foci are seen in the peripheral zone of the prostate gland. However, it has been shown that only 17–57% of echo-poor foci are malignant (Harvey et al., 2012b; Spajic et al., 2007). It is estimated that 30–40% of prostate cancer cases are isoechoic while hyperechoic cases are rare. Detecting prostate asymmetry, increased vascularity, bulging in the surface of the gland or breach in the capsule can be suggestive of prostate cancer. Hypoechoic spots can also be indicative of prostatitis and infarction (Harvey et al., 2012a; Taneja, 2004). Enhanced ultrasound imaging techniques such as color doppler TRUS and contrast-enhanced TRUS provide better sensitivity and specificity but are still mostly used to obtain a guided biopsy (Heijmink et al., 2006).

Magnetic resonance imaging: This technique utilizes a powerful magnetic field to produce a detailed picture of an imaged organ. MRI uses non-ionizing radiation and is, therefore, considered safer than X-ray imaging in which ionizing radiation is used. Still, MRI cannot be used in patients with biomedical implants (Hartwig et al., 2009). Protons (hydrogen nuclei) are present in every organ in the body incorporated into fat, protein and water. When a strong magnetic field is introduced through an MRI machine, these protons align with that field. When a radiofrequency pulse is introduced through the machine, protons are forced to spin out of equilibrium. Once the radiofrequency pulse is turned off, protons align back with the magnetic field releasing electromagnetic energy. The time protons take to realign with the magnetic field and energy released during that procedure are the basis of organ or tissue differentiation in MRI imaging. The time it takes for protons to revert to resting state can be measured in two different ways producing two different images (i.e. T1-weighted images and T2-weighted images) of the same organ with each having a different quality. (Berger, 2002). T1-weighted images are often used to assess bone and lymph node metastasis of prostatic cancer as well as post-biopsy prostatic hemorrhage. The zonal anatomy of the prostate is better assessed with T2-weighted images which are essential in the detection and staging of prostate cancer (Akin & Hricak, 2007; Sala et al., 2006).

A foci of low signal intensity within the peripheral zone of the prostate is suggestive of prostate cancer. However, other pathological conditions such as inflammation, fibrosis, BPH, scars, and calcifications may also produce low signal intensity (Barentsz et al., 2012; Bonekamp et al., 2011). Additionally, T2 weighted images can't differentiate a cancerous lesion located at the center of the prostate as a low signal spot in this location is likely due to BPH. The above limitations of T2 weighted MRI explain why this technique has low specificity (37–53%) but relatively high sensitivity (75–94%) in detecting prostate cancer (Murphy et al., 2013).

Recent advances in MRI technology utilizing anatomical (T1- and T2-weighted imaging) along with functional (diffusion-weighted imaging, dynamic contrast-enhanced and spectroscopic imaging) sequences resulted in improved diagnostic accuracy of prostate cancer. (Lawrentschuk & Fleshner, 2009; J. Thompson et al., 2013). This multi-parametric MRI (mpMRI) approach is still in the development phase and its interpretation can vary depending on the type of software and MRI machine being used as well as the experience of the radiologist. To date, the most advanced MRI imaging technique is 3-Tesla MRI which offers high spatial resolution and soft

tissue contrast (Pedler, Kitzing, et al., 2015).. MRI still can't replace histology which is regarded as the gold standard approach for the diagnosis of prostate lesions.

2.3.Histology

The most reliable technique to diagnose prostate gland lesions is histopathology which involves taking a biopsy from the prostate gland. A biopsy gun with a hollow-core needle guided by a grayscale TRUS is often used to take multiple cylindrical core biopsies (8-12 usually). The biopsy needle and the ultrasound probe are inserted into the rectum. The needle punctures through the rectal wall to reach the prostate for sampling while it is being viewed via ultrasound (Mitterberger et al., 2010).

Once a diagnosis of prostate cancer is confirmed through histological examination, the lesion in the prepared tissue is graded to determine cancer aggressiveness.

The most common histological grading scheme for prostate carcinoma is the Gleason's grading system in which affected areas within the prostate are assigned a score from 1-5, with 5 being least differentiated (cells appearing immature, not distinguishable as the cells of the tissue it arose from). The scores of the two largest cancerous areas identified from histology are combined to determine the final score for the cancerous lesion, which ranges from 2 to 10. A tumor with a score of 2 is considered least aggressive while a malignant tumor receiving a score of 10 is considered as most aggressive. Tumors receiving a score of 6 or less are considered low grade while 7 is considered intermediate grade and 8, 9 and 10 are considered high grade. (Epstein et al., 2015; Zeller et al., 2007).

Prostate cancer can spread to distant organs such as the lymph nodes, liver, lung, bones and brain, which can be examined using imaging techniques such as multiparametric 3T-MRI, CT scan, and PET imaging.

Although histological biopsies are invaluable in achieving an accurate diagnosis, they are occasionally associated with post-biopsy complications such as infection, bleeding, pain in hypogastrium, perineum or urethra, high body temperature, nausea, vomiting, and the need for bladder catheterization (Eichler et al., 2006; Madej et al., 2012). Though quite uncommon,

physical alteration such as shearing effect as well as the biochemical effect due to fixation, embedding and staining necessary in histology can potentially hinder a correct diagnosis (Li et al., 2017; Troiano et al., 2009). Usually, a small section of tissue is used in the histological examination so there is a possibility of missing the lesion of interest.

2.4.Synchrotron-based Imaging

A synchrotron is a cyclic electrodynamic particle accelerator, which uses changing electromagnetic fields to accelerate charged particles (electrons) to a speed close to the speed of light. The electrons are accelerated in a large circular vacuum path containing radiofrequency cavities which allow them to acquire more energy and speed. The larger the vacuum path and the more frequent radiofrequency cavities there are, the faster the electron acceleration can be. Once electrons achieve the desired speed, the electron beam is passed through a bending magnet or insertion device, the latter are also known as undulators and wigglers. These alter the course of the electron beam causing the release of a highly brilliant and focused radiation with a wide wavelength spectrum ranging from far infrared to hard X-ray. The radiation beam is later directed down a beamline working station known as a hutch where different types of samples can be exposed (Mobilio et al., 2015). Synchrotron radiation has wide research applications in multiple disciplines including, but not limited to, biosciences, environmental sciences, minerals exploration, medical research, agriculture, engineering, and forensics.

The advantage of synchrotron radiation is that the X-ray radiation generated has higher intensity and brilliance, smaller source size, higher collimation, broader energy spectrum with tunability, and higher polarization compared to conventional X-ray. Brilliance refers to the concentration of the photons in a beam. The higher the brilliance, the more these photons can hit an exposed sample in a unit of time which allows for a more detailed examination of that sample. The better-collimated nature of synchrotron radiation refers to its more parallel and focused beam compared to conventional radiation which minimizes ray dispersion especially when the beam travels for a long distance. Synchrotron radiation is a wide mixture of different rays, each with a different wavelength, ranging from far infrared to hard X-ray. Each of these rays can be used alone or with others to study an exposed sample depending on interest and sample characteristics. Monochromators are commonly used to filter out unwanted rays, which allow the synchrotron user

to utilize a ray with a specific wavelength to study a particular sample of interest (Shenoy, 2003; Terasawa & Kihara, 1996).

Canadian Light Source:

The Canadian Light Source (CLS) is housed at the University of Saskatchewan in Saskatoon and is the only synchrotron facility in Canada. It is a third-generation synchrotron facility equipped with a 2.9 GeV storage ring (Bisby & Maitland, 2005; Hallin et al., 2006). The facility opened its doors in 2004 allowing more than 3000 scientists from Canada and the world to use its synchrotron beam for a wide variety of research projects.

Electrons are produced by an electron gun after it is heated to about 1,000 °C in the presence of a very high voltage (~ 200,000 volts). The electron gun is made up of a tungsten-oxide disk (cathode). Electrons are passed to a linear accelerator (LINAC) composed of a series of cavities each having a microwave radio frequency field of 2,856 MHz. These accelerate electrons to a speed close to the speed of light and later inject them into the booster ring. The booster ring is a 103 m long vacuum cylinder containing radiofrequency cavities in which electrons revolve around 1.5 million times within 0.6 seconds to achieve an energy of 2900 MeV making them even faster (Silzer et al., 2004; Grochulski et al., 2017). Electrons are then passed to an outer vacuum ring known as the storage ring which is 170.88 m long with a maximum current of 220 mA. It is composed of 24 alternating straight and curved segments. Two dipole magnets (bending magnets) make up each curved section which maintains the circular movement of electrons through the storage ring. Once electrons pass in between these two dipole magnets, a radiation beam is allowed to exit the storage ring tangentially through a photon port and down a beamline hutch where a sample of interest is exposed. The beamline has three different compartments; the first one is an optic hutch, which has different focusing mirrors and a filtering monochromator allowing for the selection of a desired wavelength of the light. The second hutch is known as the experimental hutch in which a sample is placed and exposed. The last hutch is a working station from where the beam line is operated, and the data is recorded. Within the CLS there are a total of 20 beamlines radiated out of the storage ring, and each can be used to expose samples for various research applications. Of these 20 beamlines, eight are devoted to biological studies, of which the Biomedical Imaging and Therapy (BMIT) facility was used to image our prostate samples. This

unit is generally used for the imaging and therapy of the biological matter (Silzer et al., 2004; Grochulski et al., 2017).

The BMIT facility within the CLS receives two beamlines, the first is from a bending magnet and is referred to as “BMIT-BM 05B1-1” or simply “BMIT-BM” and the second originates from an insertion device, i.e., multi-pole superconducting 4.3 T wiggler and is referred to as “BMIT-ID 05ID-2” or simply “BMIT-ID”. The main difference between these two beamlines is the energy range of the X-rays they produce. The BMIT-ID 05ID-2 beamline has an energy range of 25 - 150 keV while the energy range of BMIT-BM 05B1-1 is only 20 – 40 keV. The maximum penetrable thickness of the BMIT-BM 05B1-1 beam is 10 cm which is suitable for imaging small breed dogs or puppies, cats and tissue samples and was therefore used in our study. The total length of the BMIT-BM) 05B1-1 beamline is 26 m and an exposed sample is often placed in a spot which is approximately 23 m distant from the radiation source. The beam size at this spot is 240 mm x 7 mm. This beamline is a multi-modality synchrotron imaging facility which can be used for conventional absorption imaging, K-edge Subtraction Imaging (KES), Computer Tomography (CT) and In-line Phase Contrast Computerized Tomography (PC-CT) (Grochulski et al., 2017; Wiebe et al., 2015).

Phase-contrast imaging:

Since the discovery of the X-ray by Roentgen more than 120 years ago, there has been continuous development and improvement in clinical imaging techniques - the majority of which utilize an absorption-based imaging approach. Imaged samples or tissues have unique X-ray absorption properties and, therefore, allow different amounts of X-ray to pass through them to a special detector providing a shadow of their image. Tissues with weak or similar absorption properties, such as most soft tissues, cannot be differentiated easily through absorption-based imaging. (Chapman et al., 1997; Jia et al., 2012) and there was a need for a different kind of imaging technique which is not solely based on the absorption imaging technique. The phase-based imaging technique came into being around late 1990 which was based on the contrast generated by the phase shift that occurs between different parts of a sample as the X-ray pass through it. This phase-based imaging is more sensitive to the density difference even though that difference is very small, making it more useful and more informative in imaging soft tissue as compared to the

absorption-based imaging (Chapman et al., 1997). The phase contrast of soft tissue is due to the d (decrement of the real part of the complex refractive index (n) of the tissue) and the phase shift (change in phase angle of a waveform) of the X-ray that happens when the rays transmit through the tissue (Figure 2.4). The noticeable soft tissue contrast by the phase-based imaging is due to the fact that the d for many biological tissues is 1000 times larger than the absorption contrast determining factor (β) of the tissue (Jia et al., 2012).

There are various types of phase-based imaging techniques such as analyzer-based Diffraction Enhanced Imaging (DEI), propagation-based in-line propagation phase-contrast imaging (PC-CT), and grating-based imaging called grating interferometry. Each of them has its own advantages and drawbacks. But the differences are mainly about the complexity of the setup, beam characteristic requirements, field of view and finally the quality of phase information that will be retrieved (Pagot et al., 2005b). The grating interferometry is usually considered highly demanding for optical stability and due to its experimental complexity, it is not available in every synchrotron facility. Compared with the DEI, PC-CT is simple in terms of setup.

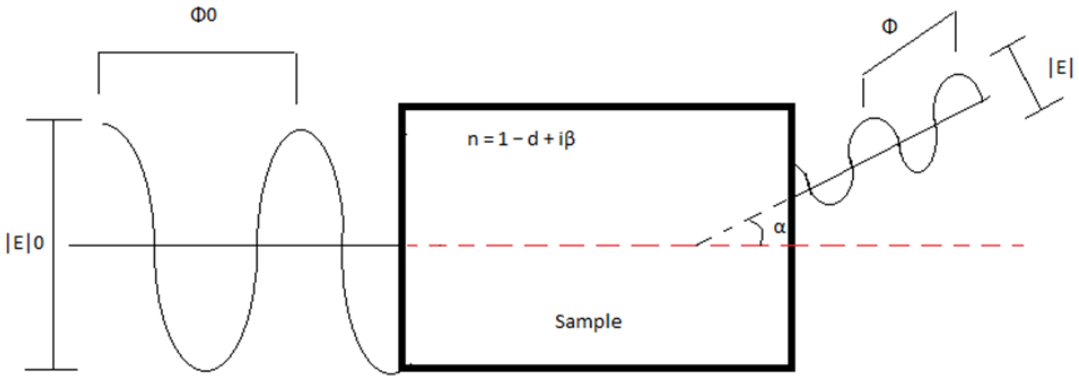

Figure 2.4. Schematic diagram showing the change in phase shift (Φ0- Φ), attenuation of the amplitude (|E|0 - |E|) and the change in propagation direction (α) when the X-rays transmitted through the material having the refractive index n (Dhakal Subash, 2019).

Though DEI has been found to give similar image quality and sometimes even higher image quality compared to PC-CT while imaging breast tumors and phantoms (Fulvia Arfelli et al., 2000; Pagot et al., 2005b; Pisano et al., 2000), and is able to render the phase information more sensitively from tissues with low variation in phase (Pagot et al., 2005b), requirements for perfect

crystals make it difficult to transform the technique to clinical use (Olivo et al., 2009). On the other hand, PC-CT, due to its simplicity and relatively low equipment cost, possesses an excellent probability to be adapted for clinical use. It also gives better spatial resolution in the image as it enhances the high spatial frequencies, although it requires a high spatial coherence of beam which is not a requirement for DEI. Additionally, PC-CT avoids the chance of image quality being degraded typically seen with DEI when the beam passes through the analyzer crystal (Pagot et al., 2005b).

The setup of PC-CT is almost the same as conventional absorption-based imaging except for the space that is allowed to be in between the sample and detector. This distance allows the phase-shifted beam to interfere with the original beam after being transmitted through the sample while it propagates between the sample and detector. The wavefront perturbations thus produced due to this phase effect produces measurable Fresnel fringes (Figure 2.5). These fringes are actually the edge enhancement of the structures inside the imaged object giving the contrast between the structures (Elfarnawany et al., 2017; Olivo et al., 2009). The intensity of fringe increases and also gets broader as the distance between the sample and the detector is increased as shown in figure 2.5. But the primary requirement for the formation of this Fresnel fringe in PC-CT is that the source should generate high lateral spatial coherent X-rays. This is usually achieved in a synchrotron source by the long source (storage ring) to sample distance and/or with the help of focusing optics.

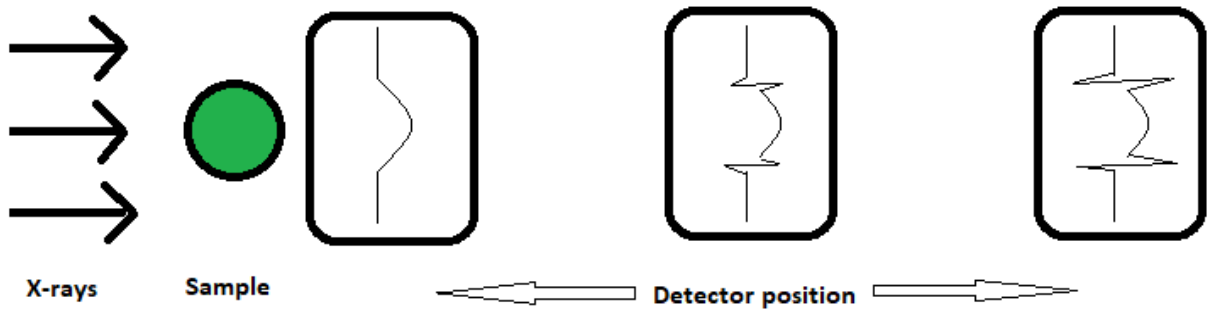

Figure 2.5 Diagram showing the formation of a more prominent fresnel fringe as the detector is moved far away from the sample in the PC-CT setup (Dhakal Subash, 2019).

When the sample is thick, the superimposed projection images of the different structures of the sample will make interpretation of the image more complicated. So, a computed tomography scan

(CT scan) technique can be applied. This technique utilizes a large number of projection radiographic images to produce the cross-sectional tomographic images which enable the visualization of the internal structure layer by layer without actually cutting the sample open. Since this development in 1967, clinical CT scan technology relies on conventional absorption-based imaging. But CT scan technology is not limited only there. Almost every imaging modality in a synchrotron facility can utilize the CT technology for the better extraction of the 3D information of samples. In PC-CT, a large number of projection images collected at an equal interval between 180° are merged with the help of specialized reconstruction algorithms to form tomographic images preserving the soft tissue contrast (Goldman, 2007; Pagot et al., 2005a).

Very few synchrotron imaging studies have been conducted with prostate glands. A group at the University of Saskatchewan conducted a study imaging excised prostate tissue from 20 dogs with eight normal prostates, eight BPH and four prostate cancer (Barboza et al., 2012; J. Montgomery et al., 2013). The imaging was done at the BMIT-BM beamline of CLS Canada. All samples were imaged with US, 16 slice CT, 3T MRI, synchrotron PC-CT, and finally, histopathology was done. US and conventional CT gave fewer structural details and it was almost impossible to distinguish normal with the pathological cases. In the case of MRI, better soft-tissue contrast was noticed, and this was in agreement with the histological findings. There was still insufficient information to distinguish different pathological conditions like BPH and prostate carcinoma. However, PC-CT was giving better soft-tissue contrast making larger microscopic details like urothelial lining, ducts, and acini, adipose tissue, muscular structure, fibromuscular stroma, etc. noticeable in the prostate (Barboza et al., 2012; J. Montgomery et al., 2013). Though the details in PC-CT images were not as clear as in histological images, the findings clearly indicate that this imaging technique is a potentially promising diagnostic tool in the future. There is a need for more studies to replicate and quantify the result and even to improve the quality of imaging.

Pagot et al. (2005b) had performed in-line propagation-based phase-contrast imaging of a phantom simulating breast tissue in which they imaged a 1mm tumor-like mass inserted in 4.2 cm thick wax. The X-ray energy that was used was 18 keV and the detector had an effective pixel size of 7.5 *7.5 um^2. PC-CT was found to give the highest edge visibility for the largest sample to detector distance (SDD) i.e. 8.8 m vs 0.3 m, 1 m, and 4.5 meters. Also, the granular texture related to the

density variation within the structure was visible in an image from a large SDD setup, which was not visible in images from a small SDD setup, though the quantitative contrast was not much different among them. Research conducted at the BMIT-BM beam-line at the CLS (Izadifar et al., 2017a) to determine the effect of propagation distance on the image quality from PC-CT used 25keV X-ray energy and three different propagation distances of 22cm, 76cm and 147cm in accessing hydrogel cardiac patches. They noticed that the edge sharpness was highest with the largest SDD. (Nesterets et al., 2015) conducted a study in which they had imaged a polycarbonate phantom (simulating breast tissue characteristics) of 10 cm diameter with three different X-ray energies (38 keV, 45 keV, and 50 keV) using a Hamamatsu CMOS flat panel detector having a pixel size of 100 *100 um^2. Having the fixed source to detector distance of 142.5 m, they had imaged the phantom altering the SDD to four different values (27cm, 1m, 2m, and 5m). From this study also, it was noticed that the edge sharpness was lowest and was blurred in the smallest SDD i.e. 27cm, while the increase in SDD was giving better phase-contrast fringe and thus edge sharpness, as well as the contrast to noise ratio (CNR) and figure of merits (FOM). The SDD of 5m had given the best phase information ((Nesterets et al., 2015)

All of these above studies with differing SDD values found that the largest SDDs were giving better images in every case. But one study using the table-top micro-CT system for propagation-based phase-contrast imaging of insects and a thin plastic sheet using a micro-focus source and CCD detector (pixel size of 24mm) found that the increase in the SDD initially increased the phase contrast and after a certain point, the image quality degraded. Here the increased propagation distance enhanced the phase information but eventually, penumbral blurring started appearing producing a low-quality image (Gui et al., 2012). Penumbral blurring is blurring of the edge of the object in an image due to the non-perfect source/focal spot (not being a point source) and is usually exacerbated by a long sample to detector distance. The formula to calculate the size of penumbral blurring is given as follows: [source size or focal spot * R2/R1], where R1 is the source to sample distance and R2 is SDD. The blurring increases as the R2 is increased. Theory indicates that to prevent the blurring that causes the image quality to deteriorate, the SDD should be within the range for which the penumbral blurring can fit in one pixel of the selected detector. To allow the larger SDD, we can choose a detector with larger pixel size, but again increasing the pixel size of the detector will lower the resolution (GOROVIKOV Sergey, personal comm., January 16,

2018). In the above-mentioned synchrotron PC-CT related studies, they had never tried the SDD beyond the limit of penumbral blurring.

In the previously discussed (Nesterets et al., 2015) study, the CNR was decreasing with the increase in keV but another quality index, the signal to noise ratio (SNR) was found to be optimal at the X-ray energy of 45keV for most of the material tested. Another study done by Olivo et al. (2009) had used 15, 17, 18, and 30 keV energy X-rays for imaging post-mortem samples of breast tissue with an almost uniform thickness of 2 cm. They had found that the details in the image were clearer when imaged with the 18 keV compared to 17 keV, demonstrating that the higher energy radiation gives greater details. But at the same time, they also found that the image quality degraded when it was imaged with 30 keV. These findings clearly indicate that there is an optimal point for energy. It was also discovered that the quality imaging of the geometric object with a sharp edge is still possible with high energy, which is otherwise not suitable for imaging a complete biological object with a gradual change in the refractive indices of the structures within it.

Another important factor that needs to be considered before implementing an imaging technique for clinical use is the dose imparted while imaging. If PC-CT is depositing a harmful amount of radiation while imaging, then it is not useful beyond ex-vivo imaging. Some studies have also been conducted to determine the clinical feasibility of PC-CT and ways to reduce the dose imparted. One way to reduce the radiation dose is by reducing the number of projections. Normally, it is considered that the number of projections (N) required is determined by $N \sim \pi D/(2P)$ in PC-CT with the FBP algorithm of reconstruction (where D is the thickness of the sample and P the detector pixel size) (Zhao et al., 2012). Studies have been conducted to investigate the possibility of a lower projection number without compromising the quality of images. In the Izadifar et al. (2017) study discussed above, projections were separately collected throughout a 180-degree rotation with four different rotation increments giving total projections of 3000 (standard), 1500, 1000 and 750. They observed that the anatomical features in tomographic images were well visualized even in the images from low projection numbers, i.e. 1500, but it was difficult to identify the microstructures with 1000 and 750 projections. The dose imparted while imaging with 1500 projections was within the range of the dose imparted by a commercially available micro-CT scanner.

Another way to image with a low dose of radiation is to decrease exposure time for each projection. But at the same time, the low exposure time may cause a low signal to noise ratio and thus low image quality of each projection and the resulting tomographic images. This is because the flux of the synchrotron is usually fixed, so the number of photons hitting the sample cannot be increased to compensate for the loss due to the short exposure time. This makes the sparse view technique a preferred one to achieve the goal of reduced radiation rather than reducing the exposure time per projection. But analytical algorithms such as the standard FBP algorithm, used for CT reconstruction will cause serious aliasing artifacts such as streaks to appear in the image when used to reconstruct an incomplete number of projections (Barrett & Keat, 2004; Melli et al., 2016). There is also the possibility of reducing the radiation dose farther by increasing the keV of the radiation source, but the challenge is that optimal value of keV should be determined so that the high keV won't cause at the same time, a reduction in phase contrast (F. Arfelli et al., 1998; Burattini et al., 1995; Zhao et al., 2012).

3. Hypothesis and Objectives

Our general hypothesis was that PC-CT will be closer-to-histology than US and MRI in the terms of having the power of detecting different structural features and small pathological lesions within the prostate. This study had four objectives:

- To examine the ability of synchrotron-based in-line propagation phase-contrast computerized tomography (PC-CT) to characterize and differentiate various structural features and pathological lesions within human prostatic tissue samples in comparison to US, MRI, and histology.
- To evaluate the usefulness of a sparse view image reconstruction technique (reconstruction with 50% and 25% of the total number of the projections) to determine if similar quality images can be obtained compared to reconstructions using 100 % of the projections.
- To quantify the radiation dose received by the patient (canine cadavers) during PC-CT imaging and to analyze the corresponding dose with a sparse view technique. The goal was to reduce the radiation to the patient during PC-CT imaging.
- To develop a human positioning device for PC-CT imaging of human prostate in situ.

4. Materials and Methods

4.1.TURP sample processing

The prostate tissue samples were from patients who underwent TURP due to BPH or suspected BPH at the Royal University Hospital (RUH), University of Saskatchewan. Samples were de-identified as to patient identification and medical history and the use of human samples was approved by the University of Saskatchewan Biomedical Research Ethics Board (Bio-REB). TURP is a standard surgical procedure in BPH management where the hyperplastic growth of the prostate from the area surrounding the prostatic urethra is scraped out and the area electro-cauterized. Resect-scope, which is an instrument containing a camera with a surgical instrument, is used for this purpose which will be inserted through the penis to reach up to the enlarged prostate. Although the patients were treated for BPH, clinical diagnosis for those excised TURP tissues from the patients were never received. TURP samples were used for this study as they were readily available, and biopsy samples of the prostate and whole human prostates were not available. The provided TURP samples (each with ~1 cm length, ~0.5 cm width, and ~0.3 cm thickness) were already fixed with 10% buffered formalin immediately after surgery. The tissues were stored in the formalin for varying period of length ranging from months to a year in between surgery and the experiments. The samples were taken out of the formalin and embedded into clear gelatin within x-ray lucent polypropylene plastic jars (Nalgene snap-cap vials of 3.3 cm (91.5ml), 4.5 cm (141.5ml), and 4.8 cm (179.1ml) diameters with same thickness of 1mm, Nalge Nunc International, New York, USA), (Figure 4.1; Table 4.1) for imaging. The jars used were already proven to be radio-transparent from a previous experiment conducted by our team. The gelatin embedding was done to provide the TURPs specific orientation, immobilize them while imaging, enable imaging of the same TURPs by other imaging modalities in the same orientation and to allow for slicing of histological samples in the same plane as the imaging. Gelatin was used as it is transparent for x-rays, ultrasound imaging, and MRI. The gelatin used was unflavored, clear Knox® gelatin (Smith® Foods, Ltd, Winona, ON Canada). To embed the tissue samples from each patient in gelatin blocks, the gelatin was prepared as follow; one pouch (7.2 gm) of gelatin was poured over 50 ml of cold water and stirred well. After that, 50 ml of boiling water was added and stirred until all the gelatin granules were completely dissolved. Once the solution became froth

less, the warm solution was added to fill one-half of the plastic jar (i.e. ~40 to 50 ml). Once that gelatin solidified at room temperature in around half an hour, TURP tissues typically three in a layer, were placed over the solidified gelatin in the jar. Additional warm (~50 to 55 degrees Celsius) gelatin was poured over to cover the tissues and allowed to solidify again at room temperature. Lead arrow markers were placed on the outer surface of the jar to indicate the tissue location for synchrotron imaging as shown in Figure 4.1. The jars were stored at refrigeration temperature for varying time ranging from two weeks to 11 months waiting for imaging shifts at CLS.

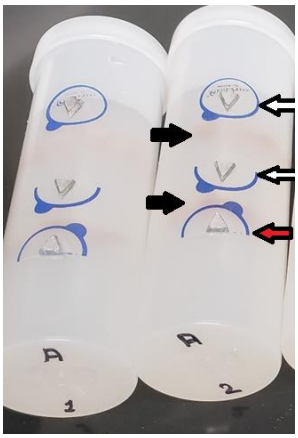

Figure 4.1 Jars of samples with lead arrow markers (white filled arrows: upper lead markers, red filled arrow: lower lead marker) indicating tissue locations (solid black arrows).

Table 4.1 Diameter of the sample jars used for imaging.

Samples imaged	Diameter of Jar
T2	3.3 cm
T9-18894	4.5 cm
T13	4.8cm
T14	4.8 cm
T1755K15248	3.3 cm
T1	3.3 cm
T7	3.3 cm
T3-14sph	3.3 cm
T9-18660	3.3 cm
T6	3.3 cm
T15-sph-18340	3.3 cm
T1a	3.3 cm
T7a	3.3 cm
T3a	3.3 cm
T9a	3.3 cm
T6a	3.3 cm
Tt15a	3.3 cm

4.2.Inline propagation PC-CT imaging and image reconstruction procedures

Two imaging shifts were carried out at the CLS on March 22, 2018 and February 1, 2019. The samples (Table 4.1) were all imaged with the setup in the BMIT–BM hutch as shown in Tables 4.2 and Figures 4.2 and 4.3.

Table 4.2 PC-CT Imaging setup used in our study**.**

Parameter	**Value**	**Reason for choosing**
keV	25	Determined by beamline scientist based on the radiation transmitted through the sample and pixel saturation values
Beam type	Filtered whitebeam (Tin 0.5 mm, Aluminium 4.5 mm)	Greater number of photons
Detector	Hamamatsu Orcha flash AA60 detector, (13.6 um2 pixel size) with Luac scintillator.	Small pixel size and fast readout speed.
Sample to Detector Distance (SDD)	1.5 meter	Wanted to have 1.85 m to maximize phase information without penumbral blurring but as the structural limitation of out BMIT hutch stage which only allows us to choose SDD either between 0 to 1.5 m or 4.5 m to 6 m.
Mode	Step and shoot	Previous experience
Projection #	2250	Minimum projection numbers suggested for this setup. Higher than this value also does not give any beneficial results.

Figure 4.2 BMIT-BM imaging hutch including sample stage (solid black arrow). Black outline allow indicates an inlet window for radiation beam into the hutch.

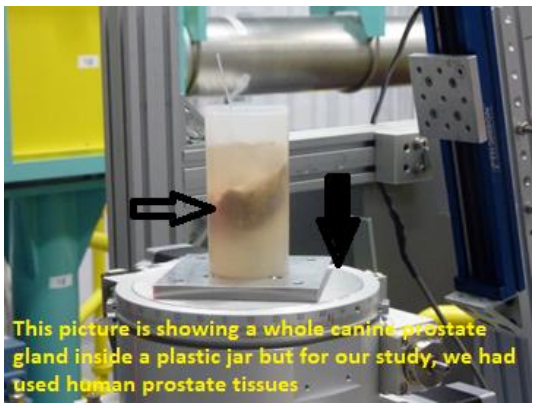

Figure 4.3 Sample jar (containing a whole canine prostate indicated by black outline arrow) on the imaging stage (solid black arrow) in the BMIT-BM hutch, representing our imaging setup except for the type of sample used.

Due to the small height of the beam used (3.1 mm), the whole area of a sample couldn't be imaged at one time. So each 3.1 mm high view was imaged beginning from just below the tip of the upper lead arrow marker (top of TURP samples) and successive views were collected by moving the stage up 3 mm following each view (with a 0.1 mm overlap of the views) until the tip of the lower lead arrow marker (bottom of sample) was reached. The imaging procedure was controlled from the control room just beside the imaging BM hutch using HiPic 9.3 pf7 software from Hamamatsu Photonics (Shizuoka, Japan).

At the beginning and end of imaging, each view 20 dark images (without the beam) and 20 flat images (without sample) were also collected. These were later used to make corrections to the collected tomographic projections prior to reconstruction by subtracting both dark projections and flat projections from original tomographic projections (Wolkowski et al., 2015).

The collected cross-sectional tomography slices were reconstructed into a PC-CT image using a parallel beam geometry filtered back projection (FBP) algorithm using the Linux-based open-source software UFO-KIT with the help of in-house graphic user interface (GUI) developed for use by BMIT users was used.

It is the primary software that BMIT uses for fast reconstruction of CT data.. The following settings were used: regularization value 2.5, filter strength 3 and auto axis of rotation.

4.3.MRI imaging

Imaging of all samples (Table 4.1) was performed at the Western College of Veterinary Medicine on February 11 - 13, 2019. The lead markers on the sample jars were replaced with vitamin E pills as they are visible in the MRI image and metal cannot be used during MRI imaging (Figure 4.4). The MRI machine used in the WCVM was a MAGNETOM Symphony 1.5T machine (wrist array coil; SIEMENS, Munich, Germany). T1-weighted images were collected with following parameters: FOV (field of view) = 70mm, SLT (slice thickness) = 1.3mm, TR (repetition time) = 925ms, TE (echo time) = 115ms, Flip angle = 180 degrees, Matrix = 164x256, Voxel size = 0.3X0.3X1.3mm^3, Bandwidth = 150Hz/Px and Turbo factor = 17 while T2-weighted images were collected with FOV = 70mm, SLT = 1.3mm, TR = 685ms, TE = 14ms, Flip angle = 90 degrees, Matrix = 164x256, Voxel size = 0.3X0.3X1.3mm^3, Bandwidth=130Hz/Px, Turbo factor=17. T1 and T2-weighted MRI images were collected in the same plane as the PC-CT images (Figure 4.5).

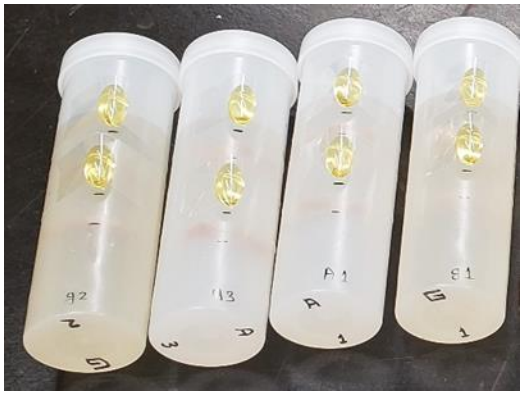

Figure 4.4 Sample jars with vitamin E pills taped on them as MRI markers.

Figure 4.5 Sample jar (indicated by the red arrow) being MR imaged.

4.4.US-Biomicroscope Imaging

The most commonly used clinical ultrasound machine operates with frequency in a range of 2 to 12 MHz. As the frequency becomes higher, the resolution increases simultaneously with reduction of the penetration depth. A Vevo® 3100 Ultrasound Biomicroscope (FUJIFILM VisualSonics, Toronto, Canada) in the Department of Veterinary Biomedical Sciences at the WCVM was used. It is a state-of-the-art ultrasound machine with a probe frequency ranging from 15 to 71 MHz. The depth of penetration is limited, so it is only suitable for imaging tissue samples or smaller laboratory animals such as rats and mice, and not for clinical purposes. For US-Biomicroscopy, the TURP samples still embedded within the gelatin blocks had to be taken out of the plastic jars as the plastic is not transparent for the ultrasound. This was done without disrupting the smooth cylindrical structure of the gelatin blocks by gently inserting a long fine round aluminium stick from a point at periphery between gelatin block and plastic jar and moving it throughout the periphery of the block to loosen the block form the jar. Gentle multiple tapping from the bottom while the jar was in an inverted position caused the gelatin block to come out from the jar. From a test trial with a sample, it was found that the MX400 linear transducer (30 MHz frequency, axial resolution 50 μm, depth of penetration 20 mm, and width coverage of 15.36 mm) was suitable for our samples considering the maximum possible resolution versus the maximum depth of penetration that could be achieved while imaging the gelatin cylinder in cross-section. The excess gelatin along the longitudinal side of the cylinder was removed as much as possible by cutting with microtome blades (Feather Safety Razor Co., Ltd Osaka, Japan) to reduce the cross-sectional

diameter for imaging while still keeping the TURP samples immobilized in the same position and to allow the gelatin block to be subsequently returned to the jar in its original orientation (Figure 4.6). The depth and width coverage capacity of the transducer was still not enough to cover the resulting sample diameter so each cylinder was imaged in two steps: left and right, (starting from top to bottom each time) to cover the whole width and again by inverting the cylinder and imaging from the opposite side (again left and right separately) to cover the remaining depth.

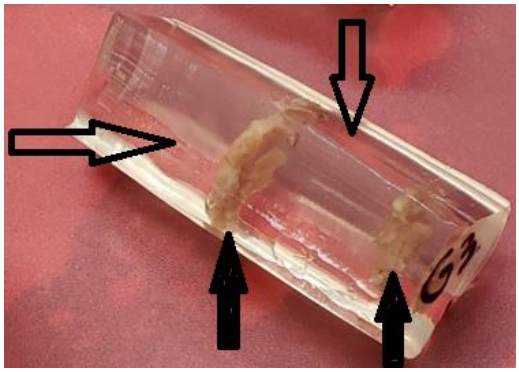

Figure 4.6 TURP samples (solid black arrows) within longitudinally trimmed gelatin block to reduce the imaging depth. Black outline arrows indicate trimmed surfaces.

A water trough with a wax block at the bottom was filled with water the day before imaging to allow the air bubbles to come out of the water. On the imaging days (February 15 -22, 2019), the sample was kept immobile by pinning a needle through the sample cylinder into the wax block (Figure 4.7). The average gain value of 24 dB, three focal points setting at the 8 mm, 10 mm and 12 mm of depth and the step size of 0.04 mm were set constant for all the B-mode sample imaging. The probe tip was submerged in water just above the surface of the sample cylinder and was set to move along the longitudinal axis of the gelatin block while moving along a straight rail to capture the cross-sectional images comparable (in the same plane) as the PC-CT and MRI images.

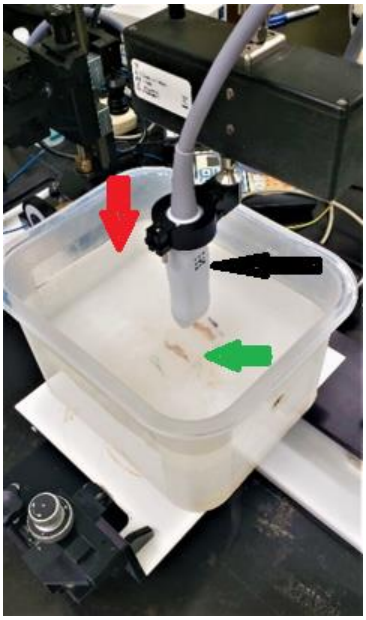

Figure 4.7 US transducer (black arrow) hanging on rail and sample block (green arrow) fixed in place underwater (red arrow). The transducer in the picture is perpendicular to the orientation we had used in our sample imaging. This picture was taken before we had decided the imaging protocol.

After ultrasound imaging was completed, all the sample blocks were placed back into their respective jars without disturbing the orientation and position of the embedded TURP samples. The resulting space between the samples and the jar (as the gelatin cylinders had been trimmed for US imaging) were refilled with liquid gelatin and allowed to solidify at room temperature for around 30 minutes. This was to preserve the firm cylindrical straight structure of the sample block in its original orientation so that the tissues could be subsequently sliced for histology in the same plane as the already captured images from the different imaging modalities. After the gelatin solidified, all samples were refrigerated (2-8 degree Celsius) until histological processing was carried out (i.e. for next two and half months).

4.5.Preparation of histology slides and their selection for comparison

Detailed procedures of histological preparation of the tissues are described in Appendix 1.

Once the histology slides were prepared representative slides were selected making sure TURP samples were not missed nor repeated. As each sliced tissue layer (see Appendix 1) shouldn't be

less than 3 mm in thickness it was decided to randomly choose one slide among the slides made from each 3 mm slice. Once the slide from any given slice was chosen, the flexibility to move a maximum of 2 slides above or below the chosen slide was allowed if the histological preparation of the selected slide was poor or only had a small amount of tissue compared to the adjacent slides. After that, the selected histology images were matched with the sequential PC-CT images to ensure that one slide for each tissue without repetition were taken. In a few cases, a unique TURP sample was not included in any of the histology slides selected. So, the corresponding histology slides were found and added to the list of slides to be compared. In this way, 22 histology slides were selected from 13 patient samples which in total included 61 TURP tissues. A high-resolution digital copy was made for each of the selected slides.

Matched images to the histology slides were selected from each imaging modality and comparisons were performed at the same magnification. The PC-CT images were set to 100% magnification as the reference magnification and the same physical magnification was applied for other modalities. This resulted in a magnification level of 11% magnification for the histology images. Each image was separately evaluated blind to sample identity. The presence of the following structures was evaluated: glandular lobules, dilated acini, smooth muscle, fibrous tissue, adipose tissue, blood vessels, lymphatics, mineralization, and inflamed area. These are structures that were identified in the 11% magnified histology images when a small pre-study examination was conducted with a small practice set of images. If present, their size (longest diameter/length) was determined from the images using “straight” tool from ImageJ (Rasband, 2018.) The presence and size of all structures were compared among the matched images from the different imaging modalities and histology.

Fibrous tissue was evaluated differently than the other structures as it is the basic structure of the prostate tissue. Even when none of the structures listed above were detected, fibrous tissue was still present. So, it was not possible to mark each and every area containing the fibrous tissue. Therefore, it was decided to pick certain locations in images from all modalities and access if those are fibrous area or not. The examination was started with the US images as US images were assumed to be of lowest quality and should reduce bias in examining the areas in the other modalities afterward. It is due to the fact that, because of very bad image quality, we would have almost no confidence from US images in saying the encircled area really a fibrous tissue area. Four

different locations (~1000um) were identified in each of the US images that appeared to be fibrous areas, and the same locations in the corresponding images from the other imaging modalities were also identified. Each of the identified structures in the 11% magnified histology, PC-CT and MRI images were evaluated independently to estimate whether they were fibrous tissue or not. After completing judgement in all modalities, the estimations were cross-checked with the histology images.

4.6. Sparse view image reconstruction and image comparison

For the comparison of the quality of PC-CT images reconstructed from different numbers of projections, 37 randomly selected tissues from the original set of 61 tissues were used, keeping at least 2 from each patient (because of the time constraint). Images were already reconstructed with 100% of the total number of projections (i.e. 2250), so the slices were then reconstructed using 50% of the total projections (every second projection) and 25% of the total projections (every fourth projection) using the same techniques as before. In this way, 111 reconstructed PC-CT images (100%, 50%, and 25% total projections) from 37 tissues were gathered and then renamed and randomized so that their identity was unknown to the observer. Each of the deidentified images was evaluated as before. Following the evaluation, the identity of each image was revealed, and they were compared with their corresponding images within the TURP sample (100% vs 50% and 25% projections) as before.

4.7. Quantifying the radiation dose received by the patient (dog cadaver) during PC-CT imaging at the BMIT-ID beamline.

Prior to this current study, radiation dosimeters and an ionization chamber were utilized to collect radiation exposure data during PC-CT imaging of canine cadavers. Five dog cadavers in a separate study were imaged in the BMIT-ID beamline using a custom-made aluminum and x-ray friendly plastic canine holding device to keep the subject in a vertical position (Figure 4.8). Measuring delivered radiation doses was not a goal of this previous study but the data were collected at that time to minimize the number of cadavers imaged and provide the raw data for this study. A 120 KeV filtered whitebeam (filter: 1mm Al, 1.5 mm Cu) and a Dalsa detector (Teledyne DALSA Waterloo, Ontario) with a $50um^2$ pixel size were used. The subject was 55m from the wiggler source (3.5T) and the sample to detector distance was 2.0 m. The ionization chamber was placed

in the beam between the source and the dog cadaver at 50 m from the source and just after the entry point of the beam into the experimental hutch. The beam width at the subject (55m from the source) was 110 mm in width and ~7.8 mm in height. Three radiation dosimeters were placed on the outside of the canine cadaver-holding device during PC-CT imaging of each cadaver, one at the approximate vertical center of the beam and the other two (upper and lower) 50 mm away from the central one to measure the scatter of the beam. The approximate vertical centre was determined by lasers aligned to the beam. Optically stimulated luminescence (OSL) technology based Luxel®+ dosimeters (LANDAUER, Glenwood, USA) were used. They contain a very thin strip of AI2 O3:C (aluminum oxide) crystalline material which is a key part in measuring the radiation exposure.

Figure 4.8 Three radiation dosimeters (black arrows) attached on the outer surface of the cone (red arrow) containing the dog cadaver. The middle one was centered in the horizontal beam, and the upper and lower dosimeters were 5 cm away from the center dosimeter

The cumulative dose reading from the ionization chamber was recorded immediately after the x-ray exposure. The reading was subsequently corrected for distance as the ionization chamber was 50 meters and the cadaver was 55 meters from the radiation source. The correction was done by multiplying the ionization chamber reading by $(50/55)^2 = 0.86$ (Ning Zhu, BMIT Beamline Scientist, personal communication, October 24, 2019). The cumulative radiation dose recorded in the luxel+ dosimeter was measured at Landaur's laboratory (Landauer, Inc., 2 Science Road,

Glenwood, Illinois, USA) by stimulating the AI2 O3:C (aluminum oxide) crystalline material of the dosimeter by selected frequencies of laser light to cause it to luminesce in proportion to the amount of radiation to which it was exposed. The total time the dosimeter was exposed to radiation was calculated by determining the number of projection images in which the central dosimeter was visible out of the total 2000 projection images. This included projections where the dosimeter was directly exposed to the beam, projections when exposed to the beam at an angle and projections when exposed to the beam after it had travelled through the cadaver. The dosimeter would be radiated more whenever it was directly exposed to the beam compared to when the beam was passing through the dog first and hit the dosimeter afterward. This ratio of visible/total projections for each cadaver was used to derive the corresponding doses the dosimeter would read if the dosimeter had been exposed for all 2000 projections directly to the beam. The calculated dose was then compared with the ionization chamber reading.

The different luxel+ dosimeters for imaging different dog cadavers were exposed to the direct beam for different numbers of projections unlike the standard 2000 projections for the ionization chamber. Therefore, to make the dosimeter readings comparable with the ionization chamber readings and to establish the relationship between these two, it was necessary to derive the corresponding dosimeter exposure if the dosimeters were exposed for all 2000 projections to the beam. Moreover, the central dosimeters for Dog 1 and Dog 5 were only indirectly exposed to the beam i.e. when facing towards the detector. The rays were passing through the dog's body and then only hitting the dosimeters (transmitted exposure). This non-uniformity from cadaver to cadaver was because the starting position of the dosimeters was not the same for imaging each cadaver. These two cases were taken to begin further analytical calculations to finally derive the corresponding dosimeter exposure if the dosimeters were exposed for all 2000 projections to the beam, as discussed in corresponding results section.

4.8.Designing a holder for PC-CT imaging of a human pelvis

The purpose of this work was to design and test a tool to hold a human pelvis or a pelvic phantom for synchrotron PC-CT imaging as a simulation of non-invasive in-situ human prostate imaging. Ultimately, if synchrotron-based X-ray imaging allows for earlier detection of prostate cancer it is

hoped that it may allow for more focal therapy of prostate cancer in men where the disease often only affects a small portion of the prostate gland.

A previous graduate student had already designed and developed a canine positioning device to perform PC-CT prostate imaging of dogs (Figure 4.9). The prostates of several cadavers and six live dogs were successfully imaged in-situ using the canine positioning device. This device had an aluminum base portion to facilitate attachment to the multi-axis positioning table in the BMIT-ID hutch. So, it was decided to design the human-specific device to attach to the aluminum base portion of the canine positioning device in place of the plastic cradle that supported the dogs. This would take advantage of an already manufactured base where the stability performance was already known for that structure. We would be using it as a “pre-base” structure of our holder.

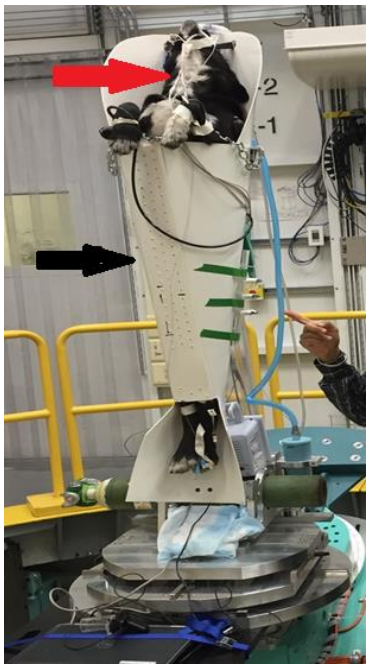

Figure 4.9 Canine positioning device (black arrow) holding a live dog (red arrow) for PC-CT imaging in BMIT-ID at Canadian light source

Before starting to design, the basic requirements of the pelvis holder that we were going to build had to be determined. These specifications were;

- The maximum weight of the holder shouldn't be more than 55kg (assuming the maximum weight of pelvis would be 50 kg, the aluminum base was already around 25kg and the MRT stage on BMIT-hutch could only lift up to a total of 130kg.
- Height of the holder ~45cm.
- Should be able to hold possible exudates from samples.
- The maximum acceptable movement of the holder is less than 6.5 um^2 as the minimum pixel size of the detector we had planned to use was 6.5 um^2.
- The holder's main part through which radiation would pass should be made up of polycarbonate or polyethylene. Other structures should be made up of any light metal like aluminum.
- To make the holder suitable for a smaller as well as a larger pelvis, two polycarbonate or polyethylene holders (one with 50 cm diameter and another with 35 cm diameter) had to be designed.
- The maximum thickness of the holder wall should be 0.3 cm to ensure transmission of at least 90% of the radiation.

In collaboration with RMD Engineering Inc. Saskatoon, funded by Mitacs Accelerate, the pelvis holder was designed using Autodesk Inventor 2017 software (ADI). An aluminum frame was selected for its weight and strength. Ongoing consultations directed various structure and design modifications and confirmed the need to use an artificial pelvis. The University of Saskatchewan prostate research team advised mimicking a real human pelvis with a male pelvic phantom (radiological device) or a pelvic structural model to mimic a real pelvis from a radiological perspective (i.e., with the use of animal flesh around a bony pelvis and placing a real prostate at the centre). The final selection was a single polyethylene/polypropylene holder of 41.8 cm external diameter and 41.2 cm internal diameter, with additional clamps at the lower part of the holder to secure it to the aluminium frame. The final design was approved by the prostate research team in a meeting.

4.9.Data collection and analysis

For objective 1 (prostatic structures in different imaging modalities), the experimental design was a cross-over design. Based on the structures visible in the 11% magnified histology images, the

following structures were analysed and compared among the modalities of detection. Although there is no relationship between the presence of the following structures with the occurrence of prostate cancer, the ability to identify the following structures is an indicator of image quality obtained with the various modalities.

List of different structures and pathological lesions that were recorded.

Glandular lobules
Dilated acini (>350um)
Area of glandular tissue (>1000um)
Smooth muscle (>1000um)
Fibrous tissue (>1000um)
Adipose tissue (>1000um)
Blood vessels (>150um)
Lymphatics (>150um)
area of mineralization
Inflamed stromal area (>1000um)
Inflamed glandular area (>1000um)

A total of 646 data points were collected on the above structures. Of those, 91 were visible either in PC-CT, MRI or US but not in histology. These structures were designated as artifacts, representing false-positive results, based on the assumption that histology is the gold standard reference diagnostic technique for our comparisons. Further, all structures that were found misidentified in the 11% magnified histology images (n=18) when compared to the 100% magnification histology images were designated as correctly identified structures to make the 11% magnified histology an absolute reference diagnostic modality, based on the assumption that the ability to accurately identify structures in the 11% magnified histology is the same as in the 100% magnified histology.

No statistical significance tests were performed on structures with $n \leq 10$; these structures did receive a descriptive analysis. This included mineralization (n=3), adipose tissue (n=4), smooth muscle (9), inflamed stromal area (n=10) and inflamed glandular area (n=6). All other structures

were statistically analysed among different imaging modalities with the McNemar $\chi 2$ test. As histology was assumed to be the gold standard reference diagnostic technique, there was no rationale to compare the difference between the histology images and the PC-CT, MRI or US images. The histology would always be found significantly more powerful unless both modalities compared identified the same number of structures. Consequently, the McNemar $\chi 2$ test was only used for comparing PC-CT with MRI, PC-CT with US, or MRI with US. Two categories of structures were created for each imaging modality for the McNemar $\chi 2$ test: "agreed with histology" and "not agreed with histology". Since "misidentified structures" and "not visualized structures" were both unwanted outcomes from a clinical point of view, they have been placed into the "not identified" category. There were also some structures that were present in histology as individual structures (let's say x in number) but with imaging appeared as a combined structure(s) (let's say y in number) at the same location. The x-y number of structures were included in the same category "not identified". Identified individually as in histology (correctly identified) structures and the combined structures (y) were included in the "agreed with histology" category. The same process was applied for presenting number of structures in Tables 5.2-5.4 as appropriate. The McNemar $\chi 2$ significance test was applied only if the discordant pairs are more than 25 in number.

For size comparisons, three different types of data pairs were compared. The statistical analyses used were based on the type of pairs and the nature of the data. Type one: size comparison of the structures correctly identified in both histology and a specific imaging modality. For example, a comparison of the size of blood vessels correctly identified in histology and PC-CT (Figure 4.9: sizes of "a", "b" and "c" vs sizes of "a'", "b'" and "c'"). This kind of comparison is the dependent sample comparison. Type two (independent samples): histology-measured sizes of structures correctly identified in both histology and a specific imaging modality vs sizes of structures that were misidentified with imaging (Figure 4.10: sizes of "a", "b" and "c" vs sizes of "d" and "e"). Type three (independent samples): histology-measured sizes of structures correctly identified in both histology and a specific imaging modality vs sizes of structures that were not visualized with imaging (Figure 4.10: sizes of "a", "b" and "c" vs sizes of "f" and "g").

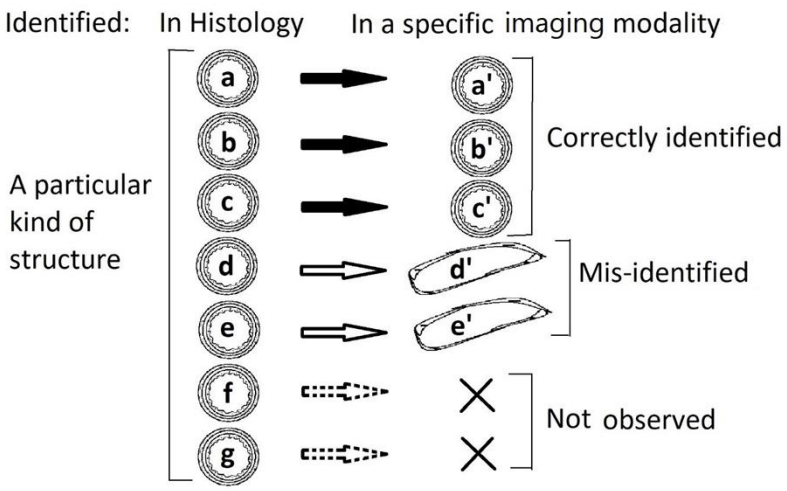

Figure 4.10 Schematic diagram representing the three different kind of pairs of data to be compared for statistical size comparison. The " a "," b " and " c " in the histology are the structures that were also correctly identified in a specific imaging modality represented by " a' ", " b' " and " c' " respectively. The " d " and " e " structures in the histology were mis-identified in the specific imaging modality and represented by " d' " and " e' " respectively. The " f " and " g " represent the structures that were not seen at all in the specific imaging modality. The structures labeled as prime (a', b', etc) refer to the same structures as evaluated with the non-invasive imaging modalities.

GraphPad Prism8 software and GraphPad's free web QuickCalc (GraphPad Software Inc., California, USA) were used for the statistical analysis. Size comparisons were done by either Paired T-test (dependent samples and parametric data), Unpaired T-test (independent samples and parametric data), Wilcoxon Signed Rank test (dependent samples and non-parametric data) or Mann Whitney U-test (independent samples and non-parametric data). The significance tests were applied only if the sample size was at least 3 in each compared group.

For the analysis of the data from the experiment for objective 2 (prostatic structures in different sparse view PC-CT imaging), again no statistical significance tests were performed on structures with $n \leq 10$; these structures did receive a descriptive analysis. This included mineralization (n=2), adipose tissue (n=3), smooth muscle (5), inflamed stromal area (n=8) and inflamed glandular area (n=2). The McNemar $\chi 2$ test was used to compare the PC-CT images reconstructed from different numbers of projections – similar to what was done in the Objective 1 data analysis. The size comparison was done between the structures visible in the matched PC-CT images reconstructed from two different number of projection images. For example, comparison of cyst sizes measured in 100% projection PC-CT and 50% projection PC-CT. The size comparison was done by either

Paired T-test (parametric data) or the Wilcoxon Signed-Rank test (non-parametric data). GraphPad Prism8 software and GraphPad's free web QuickCalc were used for the statistical analysis as before.

5. Results

The spatial resolution achieved with the setup and detector used was 12.49 µm.

5.1.General appearances of different structures in PC-CT

In most of the cases, dilated acini appeared as round or oval structures with a brighter border and homogenous dark inner space (Figure 5.1, 5.3 & 5.4). Blood vessels were most of the time seen as oval or longitudinal structures with a smooth border. Arterial walls were found to be brighter than those of the veins. Blood filled vessels were found to have brighter central spaces while empty vessels were found to have darker central spaces. Glandular lobules were found to have a well-demarcated outline with dark and bright ill-defined small oval structures (regular sized acini) bunched together inside the demarcation (Figure 5.1 & 5.4). The glandular areas were also the same but did not have well-defined demarcation and were usually smaller in size (Figure 5.1).

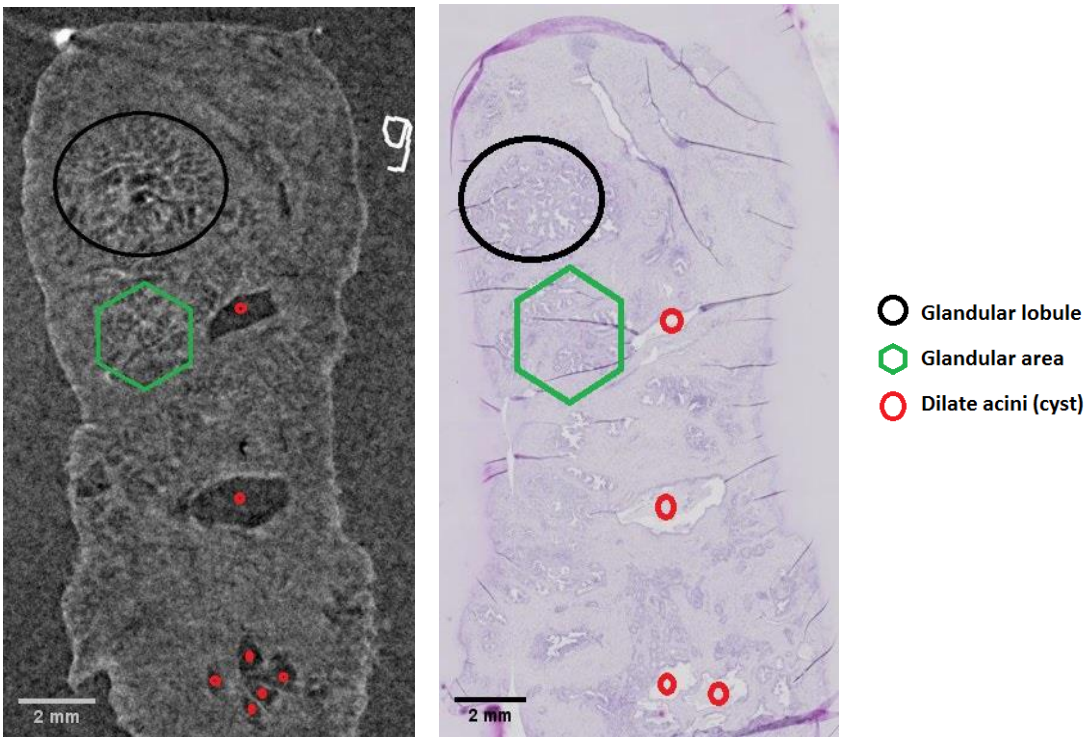

PC-CT Histology

Figure 5.1 PC-CT and histology images of matched samples showing glandular lobules, glandular area, and dilated acini.

Lymphatics were found to have mostly oval or longitudinal but spiked outlines with dark space in the middle. Smooth muscles were found to have black and white longitudinal stripes giving the appearances of Ganga's delta of Bangladesh (Figure 5.2).

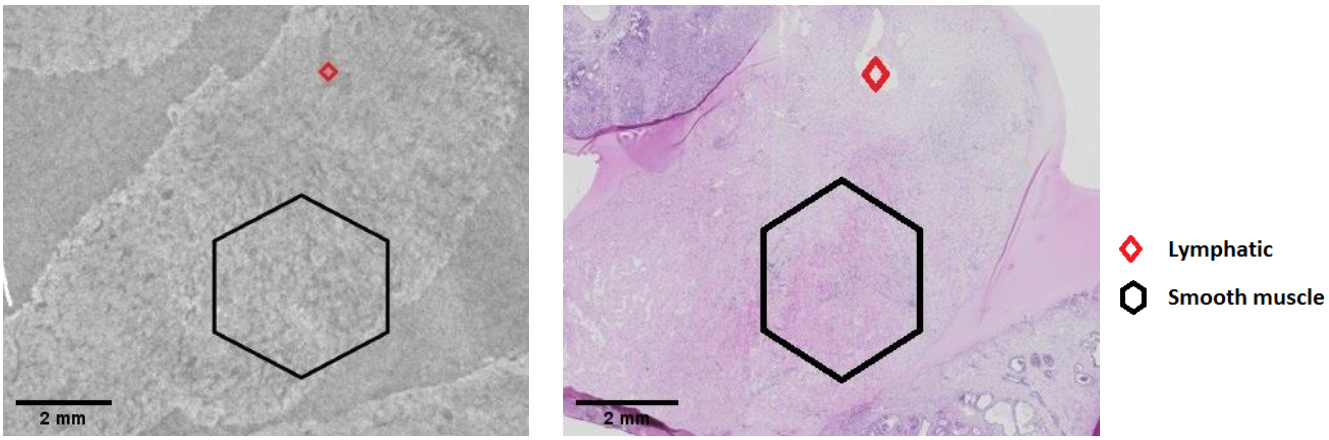

PC-CT Histology

Figure 5.2 PC-CT and histology images of matched samples showing lymphatics and area of smooth muscle.

All the visible mineralization appeared as the bright spots or bright glaring headlights (Figure 5.3).

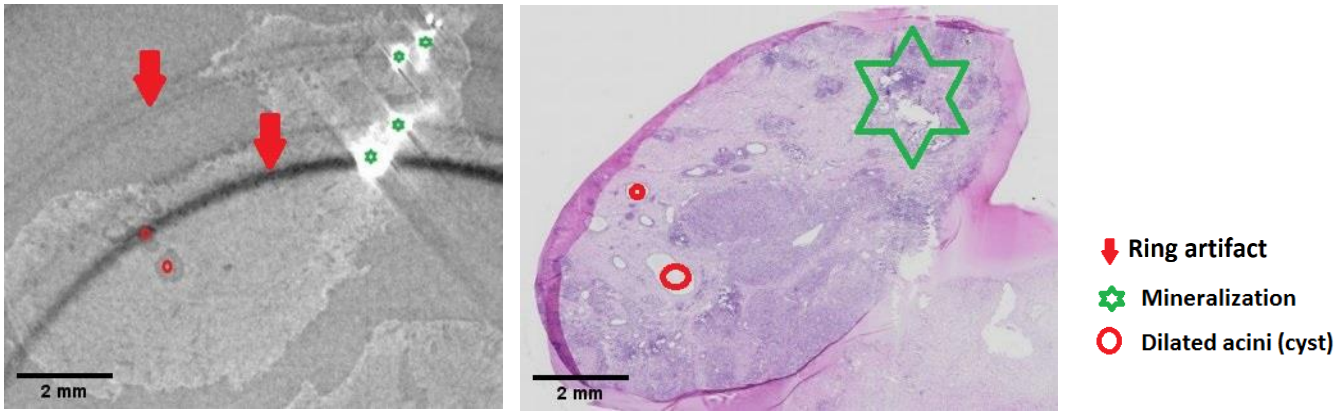

PC-CT Histology

Figure 5.3 PC-CT and histology images of matched samples showing an area of mineralization and dilated acini.

5.2. Results from the experiment for objective 1: to examine the ability of synchrotron-based in-line propagation phase-contrast computerized tomography (PC-CT) to characterize and differentiate various structural features and pathological lesions within human prostatic tissue samples in comparison to US, MRI, and histology.

There were 10 different types of tissue structures identified with histology (Table 5.1). The percentage of agreement of these identifications differed among PC-CT, MRI and US (Figure 5.4; Table 5.2, 5.3, 5.4).

Table 5.1 Number of different structures noted in the histology slides of the 61 tissues**.**

Structures	**Count**
Area of adipose tissue	4
Blood vessel	172
Dilated acini	125
Area of glandular tissue	71
Inflammatory stromal area	10
Inflammatory glandular area	6
Lymphatic	118
Area of mineralization	3
Glandular lobules	36
Area of smooth muscle	9
Grand Total	**554**

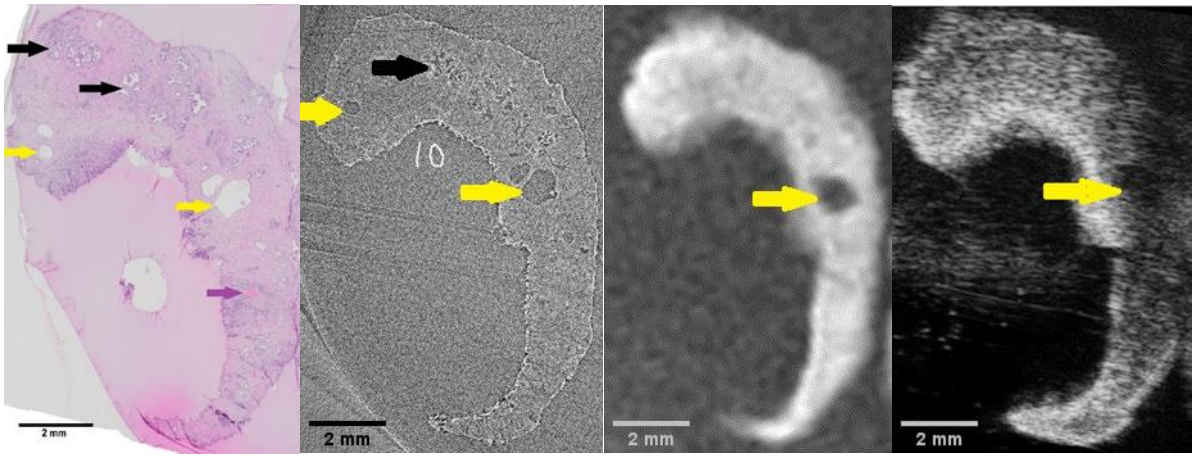

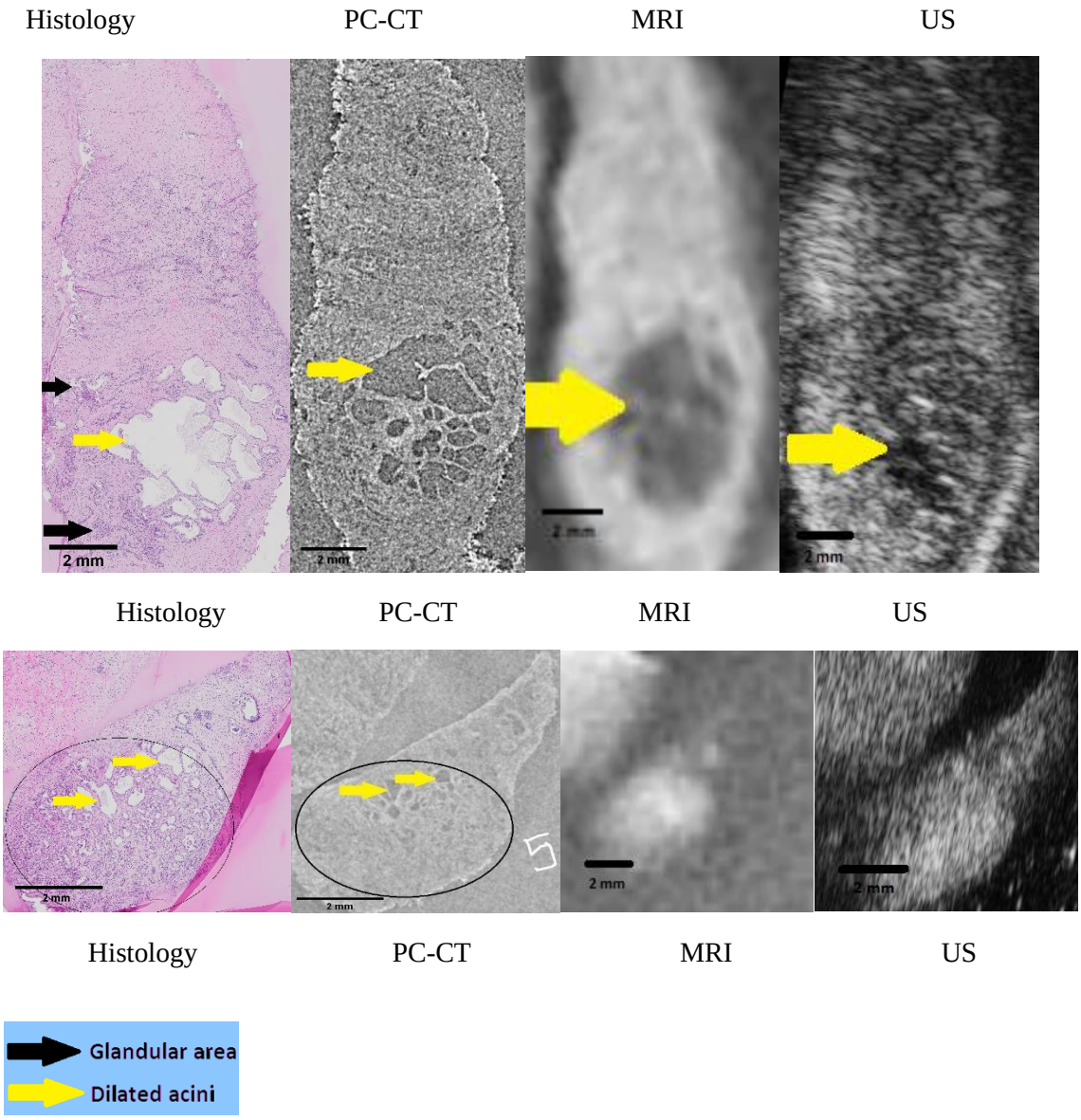

Figure 5.4 Images from different diagnostic modalities of the same plane of the tissues. Black oval outline is indicating area of glandular lobule.

In PC-CT, 5.3% (n=8) of structures that were visible individually in histology appeared combined into just three structures: three glandular lobules appeared as one glandular lobule; two more glandular lobules appeared as one glandular lobule and three glandular areas appeared as one glandular area. In MRI, 38.8% of histologically identifiable individual structures (n=19; all dilated acini, in 3 tissues out of 61 tissues) appeared combined as just seven structures. In US, 30.8% of

histology's visible unique structures (n=4; all dilated acini, in 1 tissue out of 51 tissues) combined to appear as a single structure.

Table 5.2 Structures present and accuracy in identifying them with PC-CT.

	Total observed with histology	**Agreed with histology in PC-CT (n, %)**		**Mis-identified in PC-CT (n, %)**		**Not identified in PC-CT (n, %)**	
Structures		**n**	**%**	**n**	**%**	**n**	**%**
Area of adipose tissue	4	0	0	1	25	3	75
Blood vessel	172	28	16.3	5	2.9	139	80.8
Dilated acini	125	67	53.6	9	7.2	49	39.2
Glandular area	71	15	21.1	3	4.2	53	74.7
Inflamed stromal area	10	0	0	0	0	10	100
Inflamed glandular area	6	0	0	0	0	6	100
Lymphatic	118	14	11.9	10	8.5	94	79.6
Area of mineralization	3	2	66.7	0	0	1	33,.3
Glandular lobule	36	15	41.7	1	2.8	20	5
Area of smooth muscle	9	5	55.6	0	0	4	44.4
Overall	554	146	26.4	29	5.2	379	68.4

With PC-CT, 26.4% of the total structures were identified correctly (Table 5.2). Area of mineralization was the most often correctly identified (2 out of 3 areas), followed by smooth muscle area (5 out of 9 areas) and dilated acini (67 out of 125 dilated acini). None of the adipose tissue areas, inflamed stromal areas, and inflamed glandular areas were correctly identified in PC-CT.

Table 5.3 Structures present and accuracy in identifying them with MRI.

	Total observed with histology	**Agreed with histology in MRI (n, %)**		**Mis-identified in MRI (n, %)**		**Not identified in MRI (n, %)**	
Structures		**n**	**%**	**n**	**%**	**n**	**%**
Area of adipose tissue	4	0	0	0	0	4	100
Blood vessel	172	1	0.6	6	3.5	165	95.9
Dilated acini	125	33	26.4	0	0	92	73.6
Glandular area	71	0	0	0	0	71	100
Inflamed stromal area	10	0	0	0	0	10	100
Inflamed glandular area	6	0	0	0	0	6	100
Lymphatic	118	3	2.5	0	0	115	97.5
Area of mineralization	3	0	0	0	0	3	100
Glandular lobule	36	0	0	0	0	36	100
Area of smooth muscle	9	0, 0	0, 0	0, 0	0, 0	9	100
Overall	554	37	6.7	6	1.1	511	92.2

With MRI 6.7% of the total structures were correctly identified (Table 5.3). The most often correctly diagnosed structure was dilated acini (33 out of 125 dilated acini). Beside dilated acini, only lymphatics (3 out of 118 structures) and blood vessels (1 out of 172 structures) were correctly identified.

Table 5.4 Structures present and accuracy in identifying them with US.

	Total observed with histology	**Agreed with histology in US (n, %)**		**Mis-identified in US (n, %)**		**Not identified in US (n, %)**	
Structures		**n**	**%**	**n**	**%**	**n**	**%**
Area of adipose tissue	3	0	0	0	0	3	100
Blood vessel	167	0	0	4	2.4	163	97.6
Dilated acini	122	10	8.2	0	0	112	91.8
Glandular area	61	0	0	0	0	61	100
Inflamed stromal area	2	0	0	0	0	2	100
Inflamed glandular area	6	0	0	0	0	6	100
Lymphatic	102	0	0	1	1	101	99
Area of mineralization	3	0	0	0	0	3	00
Glandular lobule	34	0	0	0	0	34	100
Area of smooth muscle	8	0	0	0	0	8	100
Overall	508*	10	2	5	1	493	97

* Some missing data for US (n=46)

Only 2% of the total structures were identified correctly in US (Table 5.4), and all of them were dilated acini.

Table 5.5 McNemar $\chi 2$ tests comparing the abilities of different imaging modalities to correctly identify the lesions and structures:

Structure	Modalities compared	4 Box Values		Test statistics	P-Value	Result
		Both modalities+	**Modality 1+, Modality 2-**			
		Modality 1 -, Modality 2+	**Both modalities -**			
Overall	PC-CT Vs MRI	30	116	94.8	<0.05	PC-CT more powerful
		7	401			
Overall	PC-CT Vs US	8	134	126.2	<0.05	PC-CT more powerful
		2	364			
Overall	MRI Vs US	9	28	23.3	<0.05	MRI more powerful
		1	470			
Area of fibrous tissue	PC-CT Vs MRI	90	39	20.9	<0.05	PC-CT more powerful
		7	68			
Area of fibrous tissue	PC-CT Vs US	89	40	20	<0.05	PC-CT more powerful
		8	67			
Area of fibrous tissue	MRI Vs US	94	3	0.16	>0.05	No difference
		3	104			
Dilated acini	PC-CT Vs MRI	28	39	24.8	<0.05	PC-CT more powerful

		5	53			
Dilated acini	PC-CT Vs US	8	59	51.4	<0.05	PC-CT more powerful
		2	53			
Dilated acini	MRI Vs US	9	24	19.4	<0.05	MRI more powerful
		1	88			
Blood vessel	PC-CT Vs MRI	1	27	25	<0.05	PC-CT more powerful
		0	144			
Blood vessel	PC-CT Vs US	0	28	26	<0.05	PC-CT more powerful
		0	139			

"+" represents the "correctly identified" category and "-" represents the "not-identified" category of structures as previously described.

The use of PC-CT images allowed for the correct identification of 146 (26.4%) structures while using MRI and US images only allowed for the correct identification of 37 (6.7%) and 10 (2%) structures respectively (Table 5.2-5.4). PC-CT has been statistically proven significantly more powerful than MRI and US in enabling the correct identification of structures and areas (<0.05) (Table 5.5).

There was no difference among the size of dilated acini measured from histology, PC-CT, MRI and US ($p>0.05$; Table 5.6). There was also no difference between the histology and PC-CT measured sizes for blood vessels, lymphatics, glandular lobules and glandular areas ($p>0.05$). An exception for this pattern was that the size of lymphatics measured from MRI images was bigger than the size measured from histology images ($p<0.05$). We did not have sufficient data for statistical comparisons of MRI and histology measured sizes of remaining structures (blood vessels, glandular lobule, and glandular area). Similarly, we also did not have sufficient data for statistical comparisons of US and histology measured sizes of remaining structures (blood vessels, lymphatics, glandular lobule, and glandular area).

Dilated acini that were visible in an imaging modality (PC-CT, MRI or US) were found to be larger than the dilated acini that were only seen in histology ($p<0.05$) (Table 5.6). There was the same pattern with lymphatics, glandular lobules and glandular areas visible in PC-CT. Blood vessels visible in PC-CT and lymphatic visible in MRI were the exception for this pattern, in which no difference in the size was noticed (>0.05). For other structures, there was insufficient data from those imaging modalities for statistical comparisons. There was also insufficient data to statistically compare of other structures (blood vessels, glandular lobule, and glandular area) that were visible in histology but not in MRI or US.

There was no uniform pattern in the relationship between the histology-measured size of structures that were correctly identified in PC-CT to those that were misidentified in PC-CT (Table 5.6). Sizes of misidentified and correctly identified dilated acini were not found to be significantly different ($p>0.05$). It was the same for glandular areas also. However, misidentified blood vessels were found to be larger in size than the correctly identified blood vessels and misidentified lymphatics were found to be smaller than the correctly identified lymphatics. For other structures (glandular area and glandular lobules) we did not have enough data to statistically compare.

Table 5.6 Comparison of the size of different structures measured by different imaging modalities.

Structure	Comparison between	Sample type	Sample size (former and latter)	Test statistics P-value	Result	Mean (µm) [1](former /latter)	SD (µm) (former/latte)	Median (for non-parametric) or SEM (for parametric) (µm) (former/latte)
Dilated acini	Sizes of structures correctly identified in both Histology and PC-CT	Dependant Non-parametric	67 and 67	Wilcoxon S.R. 0.52	No difference	698/702.6	346.8/357.8	620/590
Dilated acini	Histology measured sizes of structures correctly identified in both Histology and PC-CT Vs structures mis-diagnosed in PC-CT	Independent Non-parametric	67 and 39	Mann Whitney 0.76	No difference	698/667.8	346.8/284.3	620/500
Dilated acini	Histology measured sizes of structures correctly identified in both Histology and PC-CT Vs structures not seen in PC-CT	Independent Non-parametric	67 and 49	Mann Whitney <0.0001	Str. Seen in both modalities are bigger than not seen in PC-CT	698/472.6	346.8/157	620/420
Dilated acini	Sizes of structures correctly identified in both Histology and MRI	Dependant Non-parametric	26 and 26	Wilcoxon S.R. 0.21	No difference	872.5/835.4	470.3/525	765/635
Dilated acini	Histology measured sizes of structures correctly identified in both Histology and MRI Vs structures not seen in MRI	Independent Non-parametric	26 and 80	Mann Whitney <0.0001	Str. Seen in both modalities are bigger than not seen in MRI	872.5/520.8	470.3/193.2	765/465
Dilated acini	Sizes of structures correctly identified in both Histology and US	Dependant Parametric	9 and 9	Paired- t 0.16	No difference	1138/1520	639.1/932.3	213/310.8

[1] Former: modality mentioned first in each row of second column. Latter: modality mentioned second in each row of second column.

Dilated acini	Histology measured sizes of structures correctly identified in both Histology and US Vs structures not seen in US	Independent Non-parametric	9 and 109	Mann Whitney <0.0001	Str. Seen in both modalities are bigger than not seen in US	1138/566.9	639.1/218.9	870/500
Dilated acini	Sizes of structures correctly identified in both PC-CT and MRI	Dependent Non-parametric	22 and 22	Wilcoxon S. R 0.11	No difference	910.6/880	473.6/557.4	730/710
Dilated acini	Sizes of structures correctly identified in both PC-CT and US	Dependent Parametric	7 and 7	Paired- t 0.13	No difference	1225/1659	638.7/984.8	241.4/372.2
Dilated acini	Sizes of structures correctly identified in both MRI and US	Dependent Non-parametric	8 and 8	Wilcoxon S. R. 0.055	No difference	1121/1516	839.5/996.6	925/1282
Blood vessel	Sizes of structures correctly identified in both Histology and PC-CT	Dependent Non-parametric	28 and 28	Wilcoxon S. R. 0.39	No difference	323.3/340.4	191.2/117.6	250/300
Blood vessel	Histology measured sizes of structures correctly identified in both Histology and PC-CT Vs structures misdiagnosed in PC-CT	Independent Non-parametric	28 and 5	Mann Whitney 0.035	Str. Seen in both modalities are smaller than those mis-diagnose in PC-CT	323.3/470.4	191.2/151.9	250/460
Blood vessel	Histology measured sizes of structures correctly identified in both Histology and PC-CT Vs structures not seen in PC-CT	Independent Non-parametric	28 and 139	Mann Whitney 0.5	No difference	323.3/291.5	191.2/143	250/240
Lymphatic	Sizes of structures correctly identified in both Histology and PC-CT	Dependent Parametric	14 and 14	Paired-t 0.08	No difference	411.4/516.1	160.9/229.7	43/61.4

Lymphatic	Histology measured sizes of structures correctly identified in both Histology and PC-CT Vs structures misdiagnosed in PC-CT	Independent Non-parametric	14 and 10	Mann Whitney 0.023	Str. Seen in both modalities are larger than those mis-diagnose in PC-CT	411.4/260	160.9/67.33	…
Lymphatic	Histology measured sizes of structures correctly identified in both Histology and PC-CT Vs structures not seen in PC-CT	Independent Non-parametric	14 and 94	Mann Whitney 0.01	Str. Seen in both modalities are larger than those not seen in PC-CT	411.4/299.2	160.9/17.41	410/230
Lymphatic	Sizes of structures correctly identified in both Histology and MRI	Dependent Parametric	3 and 3	Paired-t 0.013	MRI measure bigger	451.7/910.7	157.8/77.47	91.12/44.73
Lymphatic	Histology measured sizes of structures correctly identified in both Histology and MRI Vs structures not seen in MRI	Independent Non-parametric	3 and 115	Mann Whitney 0.067	No difference	451.7/305.5	157.8/164.7	440/250
Glandular lobule	Sizes of structures correctly identified in both Histology and PC-CT	Dependent Parametric	13 and 13	Paired-t 0.064	No difference	3848/4454	925.3/1087	256.6/301.6
Glandular lobule	Histology measured sizes of structures correctly identified in both Histology and PC-CT Vs structures not seen in PC-CT	Independent Parametric	…	Unpaired-t 0.019	Str. Seen in both modalities are larger than those not seen in PC-CT	3848/2967	925.3/980.2	256.6/237.7
Glandular area	Sizes of structures correctly identified in both Histology and PC-CT	Dependent Non-parametric	14 and 14	Wilcoxon S.R. 0.33	No difference	3461/2976	1471/1512	3425/2875
Glandular area	Histology measured sizes of structures correctly identified in both Histology and PC-CT Vs structures misdiagnosed in PC-CT	Independent Parametric	…	Unpaired-t 0.99	No difference	3461/3447	1471/1608	291.2/928.3

Glandular area	Histology measured sizes of structures correctly identified in both Histology and PC-CT Vs structures not seen in PC-CT	Independent Non-parametric	14 and 51	Mann Whitney 0.033	Str. Seen in both modalities are larger than those not seen in PC-CT	3461/2640	1471/1352	3425/2230

Fibrous tissue area: There was a total of 204 fibrous tissue area locations (4 locations in each tissue) in 51 tissues whose images from all diagnostic modalities were available and tested as indicated (Section 4.5). Of these, 98 spots in US were correctly identified, 106 were not; in MRI, 97 were correctly identified and 107 were not: in PC-CT, 129 were correctly identified, 75 were not. Comparing power in identifying the fibrous tissue area, PC-CT > MRI = US ($p<0.05$).

5.3. Results from the experiment for objective 2: to evaluate the usefulness of a sparse view image reconstruction technique (reconstruction with 50% and 25% of the total number of the projections) to determine if similar quality images can be obtained compared to reconstructions using 100 % of the projections.

Histology identified a total of 312 structures in the 37 tissues used to assess accuracy of sparse view PC-CT imaging technique (Table 5.7).

Table 5.7 Number of structures noted in the histology slides from 37 tissues.

Structures	**Count**
Area of adipose tissue	3
Blood vessel	83
Dilated acini	79
Area of glandular tissue	41
Inflammatory stromal area	8
Inflammatory glandular area	2
Lymphatic	71
Area of mineralization	2
Glandular lobules	18
Area of smooth muscle	5
Grand Total	**312**

During the evaluation a total of five structures combined to appear as two structures in 100% PC-CT (two glandular lobules combined and appeared as one glandular lobule and three glandular areas combined and appeared as one glandular area). The same was found for the 50% projection PC-CT images. In 25% projection PC-CT, none of the three glandular areas were visible andanew combined dilated acinus representing three different dilated acini appeared in 25% projection PC-CT (Figure 5.5). This indicates that the power of resolving two nearby structures is low in 25% projection PC-CT, while it is better for 100% and 50% projection PC-CT images. For the sake of ease in the statistical analysis ahead, it was decided to handle such a scenario in the same way followed for objective one as explained just before table 5.2.

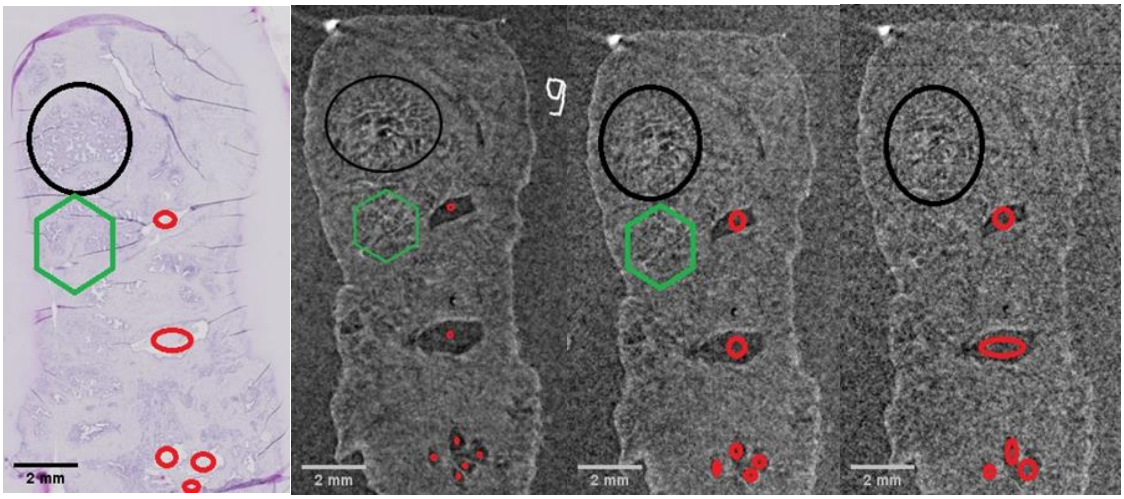

Histology 100% projection 50% projection 25% projection

Figure 5.5 PC-CT images reconstructed from a different number of projections along with the histology image of the same plane.

Table 5.8 Structures present and diagnostic accuracy with 100% projection PC-CT.

	Total	**Agreed with histology in 100% PC-CT (n, %)**		**Mis-diagnosed in 100% PC-CT (n, %)**		**Not identified in 100% PC-CT (n, %)**	
Structures		**n**	**%**	**n**	**%**	**n**	**%**
Area of adipose tissue	3	0	0	0	0	3	100
Blood vessel	83	11	13.3	3	3.6	69	83.1
Dilated acini	79	35	44.3	3	3.8	41	51. 9
Glandular area	41	5	12.2	1	2.4	35	85.4
Inflamed stromal area	8	0	0	0	0	8	100
Inflamed glandular area	2	0	0	0	0	2	100
Lymphatic	71	7	9.9	7	9.9	57	80.2
Area of mineralization	2	1	50	0	0	1	50
Glandular lobule	18	7	38. 9	0	0	11	61.1
Area of smooth muscle	5	4	80	0	0	1	20
Overall	312	70	22.4	14	4.5	228	73.1

In 100 % projection PC-CT, 22.4% of the total structures were correctly identified (Table 5.8). Area of smooth muscle was most often correctly identified (four out of five areas), while the area of mineralization (one out of two areas) and dilated acini (35 out of 79 dilated acini) were correctly identified less frequently. None of the adipose tissue areas, inflamed stromal areas, and inflamed glandular areas were correctly identified.

Table 5.9 Structures present and diagnostic accuracy with 50% projection PC-CT.

	Total	**Agreed with histology in 50% PC-CT (n, %)**		**Mis-diagnosed in 50% PC-CT (n, %)**		**Not identified in 50% PC-CT (n, %)**	
Structures		**n**	**%**	**n**	**%**	**n**	**%**
Area of adipose tissue	3	0	0	0	0	3	100
Blood vessel	83	9	10.8	2	2.4	72	86.8
Dilated acini	79	34	43	6	7.6	39	49.4
Glandular area	41	1	2.4	0	0	40	97.6
Inflamed stromal area	8	0	0	0	0	8	100
Inflamed glandular area	2	0	0	0	0	2	100
Lymphatic	71	7	9.9	4	5.6	60	84.5
Area of mineralization	2	1	50	0	0	1	50
Glandular lobule	18	4	22.2	0	0	14	77.8
Area of smooth muscle	5	3	60	0	0	2	40
Overall	312	59	18.9	12	3.9	241	77.2

In 50 % projection PC-CT, 18.9% of the total structures were correctly identified (Table 5.9). Area of smooth muscle was the most often correctly identified structure (three out of five areas), while the area of mineralization (one out of two areas) and dilated acini (34 out of 79 dilated acini) were correctly identified less frequently. As in 100% projection PC-CT, none of the adipose tissue areas, inflamed stromal areas, and inflamed glandular areas were correctly identified.

Table 5.10 Structures present and diagnostic accuracy with 25% projection PC-CT.

	Total	**Agreed with histology in 25% PC-CT (n, %)**		**Mis-diagnosed in 25% PC-CT (n, %)**		**Not identified in 25% PC-CT (n, %)**	
Structures		**n**	**%**	**n**	**%**	**n**	**%**
Area of adipose tissue	3	0	0	0	0	3	100
Blood vessel	83	5	6	1	1.2	77	92.8
Dilated acini	79	19	24.1	0	0	60	75.9
Glandular area	41	0	0	0	0	41	100
Inflamed stromal area	8	0	0	0	0	8	100
Inflamed glandular area	2	0	0	0	0	2	100
Lymphatic	71	4	5.6	1	1.4	66	93
Area of mineralization	2	1	50	0	0	1	50
Glandular lobule	18	1, 5.6	1, 5.6	0, 0	0, 0	17	94.4
Area of smooth muscle	5	2, 40	2, 40	0, 0	0, 0	3	60
Overall	312	32	10.3	2	0.6	278	89.1

In 25 % projection PC-CT, 10.3% of the total structures were correctly identified (Table 5.10). Area of mineralization was the most often correctly identified structure (one out of two areas), while the area of smooth muscle (two out of five areas) and dilated acini (19 out of 79 dilated acini) were correctly identified less frequently. As in 100% and 50% projection PC-CT, none of the adipose tissue areas, inflamed stromal areas, and inflamed glandular areas were correctly identified. Additionally, glandular areas could not be detected when evaluating 25% projection PC-CT images.

Table 5.11 McNemar $\chi 2$ tests to compare the abilities of different % projection PC-CT to correctly identify the lesions and structures.

Structure	Sparse view PC-CT techniques compared	4 Box Values		Test statistics	P-Value	Result
		Both techniques +	Technique 1 +, Technique 2 -			
		Technique 1 -, Technique 2 +	Both techniques -			
Overall	100% PC-CT Vs 50% PC-CT	53	17	4.3	<0.05	100% PC-CT more Powerful
		6	236			
Overall	100% PC-CT Vs 25% PC-CT	31	39	34.2	<0.05	100% PC-CT more Powerful
		1	241			
Overall	50% PC-CT Vs 25% PC-CT	31	28	23.3	<0.05	50% PC-CT more Powerful
		1	252			

"+" represents the "correctly identified" category and "-" represents the "not-identified" category of structures as previously described.

In 100% projection PC-CT, 22.4% structures were correctly identified while in 50% and 25% projection PC-CT, only 18.9% and 32 10.3% of the total structures were correctly identified, respectively (Tables 5.8-5.10). Comparing power in identifying structures, 100% PC-CT > 50% PC-CT > 25% PC-CT ($P<0.05$) (Table 5.11). There was insufficient data to statistically compare each kind of structures separately.

There was no difference found among the 100% PC-CT, 50% PC-CT and 25% PC-CT measured sizes for dilated acini, blood vessels and lymphatics ($p<0.05$; Table 5.12). It was the same for the size of glandular lobules measured in 100% and 50% projection PC-CT. There was insufficient data regarding glandular lobules from 25% projection PC-CT to statistically compare with others. The glandular area also had insufficient data to statistically compare their sizes in between different projection PC-CT.

Table 5.12 Comparison of the size of different structures measured by different % projection PC-CT techniques.

Structure	**Comparison between**	**Data type**	**Sample size (pair)**	**Test statistics P-value**	**Result**	**Mean (μm) [2](former/latter)**	**SD (μm) (former/ latter)**	**Median (for non-parametric) or SEM (for parametric) (μm) (former/latter)**
Dilated acini	Sizes of structures correctly identified in both 100% PC-CT and 50% PC-CT	Non-parametric	32	Wilcoxon S. R 0.23	No difference	637.8/625.6	216.4/214.4	580/577
Dilated acini	Sizes of structures correctly identified in both 100% PC-CT and 25% PC-CT	Non-parametric	17	Wilcoxon S. R 0.54	No difference	678.3/689.5	275.8/327	550/580
Dilated acini	Sizes of structures correctly identified in both 50% PC-CT and 25% PC-CT	Non-parametric	17	Wilcoxon S. R 0.97	No difference	690.9/689.5	250.2/327	660/580
Blood vessel	Sizes of structures correctly identified in both 100% PC-CT and 50% PC-CT	Parametric	7	Paired-t 0.065	No difference	315.3/291.4	53.75/70.69	20.32/26.72
Blood vessel	Sizes of structures correctly identified in	Parametric	5	Paired-t 0.87	No difference	308.4/304.6	64.19/101.8	28.71/45.5

[2] Former: Technique mentioned first in each row of second column. Latter: modality mentioned second in each row of second column.

	both 100% PC-CT and 25% PC-CT							
Blood vessel	Sizes of structures correctly identified in both 50% PC-CT and 25% PC-CT	Parametric	5	Paired-t 0.065	No difference	275.4/304.6	79.75/101.8	35.67/45.5
Lymphatic	Sizes of structures correctly identified in both 100% PC-CT and 50% PC-CT	Parametric	5	Paired-t 0.77	No difference	441.4/434.8	187/189.7	83.62/84.85
Lymphatic	Sizes of structures correctly identified in both 100% PC-CT and 25% PC-CT	Parametric	4	Paired-t 0.46	No difference	439.3/468.5	215.8/206.6	107.9/103.3
Lymphatic	Sizes of structures correctly identified in both 50% PC-CT and 25% PC-CT	Parametric	4	Paired-t 0.43	No difference	449.8/468.5	215.7/206.6	107.8/103.3
Glandular lobule	Sizes of structures correctly identified in both 100% PC-CT and 50% PC-CT	Parametric	3	Paired-t 0.14	No difference	4768/3916	345.2/864.1	199.3/498.9

5.4. Results from the experiment for objective 3: to quantify the radiation dose received by the patient (canine cadavers) during PC-CT imaging and to analyze the corresponding dose with a sparse view technique. The goal is to reduce the radiation to the patient during PC-CT imaging.

Table 5.13 provides radiation measurements from the ionization chamber and the radiation dosimeters.

Table 5.13 Radiation data generated during PC-CT imaging of canine cadavers in the BMIT-ID beamline of the CLS. Dosimeters were located directly in the beam (centre) or 50 mm above or below to determine beam scatter.

Dog Number	Dosimeter location (Centre ones were in the beam)	Number of projections with the dosimeter present in the beam (detector side/beam side = total)	Dosimeter reading (equivalent total dose (mSv)	Corrected ionization chamber reading (equivalent total dose (mSv)
1	Top		3.4	22398.7
1	Centre	500/0 = 500	82.45	22398.7
1	Bottom		4.88	22398.7
2	Top		8.02	26379.7
2	Centre	480/80 = 560	280.15	26379.7
2	Bottom		10.34	26379.7
3	Top		4.49	19268.9
3	Centre	220/160 = 380	184.57	19268.9
3	Bottom		5.31	19268.9
4	Top		8.74	24826.9
4	Centre	225/400 = 625	592.11	24826.9
4	Bottom		8.86	24826.9
5	Centre	530/0 = 530	86.77	34221.4

Mean and SEM for corrected ionization chamber reading are 25419 mSv and 2507 mSv respectively.

The dosimeters were exposed to 500 projections for dog 1 and 530 projections for dog 5. They recorded 82.45mSv and 86.77mSv equivalent doses respectively (Table 5.13). As these values are very close the average of both the doses divided by the projections (84.61mSv, 515 projections) indicates the dose is 84.61mSv/515 = 0.1643mSv/projection when a dosimeter is placed behind a dog of that size and facing towards the detector, away from the x-ray source.

Dog 2, dog 3 and dog 4 had been exposed to 480, 220 and 225 projections when facing towards the detector and 80, 160 and 400 projections when facing towards the beam and directly exposed to the beam. The dose the dosimeters received when facing toward the detector was calculated separately from the dose received when facing toward the beam.

For dog 2 the number of detector-facing projections = 480. Estimated indirect dose (from transmission exposure) for taking 480 projections = 480 x 0.1643 mSv/projection (from above) = 78.86mSv. Deducting this from the total dose measured by the dosimeter = 280.15mSv – 78.86mSv = 201.29mSv due to direct exposure of the dosimeter for 80 projections.

Adjusting exposure of the dosimeter to 2000 projections equivalent, the dose would be 201.29/80x2000 = 532.25mSv. Similarly, for 2000 projections direct exposure, the doses for dog#3 and dog#4 would be 1855.30mSv and 2775.71mSv. The distance corrected ionization chamber reading during 2000 projections for dogs 2-4 were 26379.7mGy, 19268.9mGy and 24826.9mGy respectively. The ionization chambers show readings are approximately five to ten times higher than the chip dosimeter reading (Table 5.14).

Table 5.14 Comparison of radiation data from the Luxel+ dosimeter (central) and the Ionization chamber generated during PC-CT imaging of canine cadavers in the BMIT-ID beamline of the CLS.

Dog Number (only those dogs with dosimeter being exposed directly on beam)	Dosimeter location	Calculated reading for central dosimeter when exposed for all 2000 projections directly on the beam (equivalent total dose in mSv)	Corrected ionization chamber reading (equivalent total dose in mSv)
2	Centre	5032.3	26379.7
3	Centre	1855.3	19268.9
4	Centre	2775.7	24826.9

The calculated equivalent radiation dose that would be delivered to the cadaver during sparse view imaging, differs if the dose is calculated based on the luxel+ dosimeter dose calculations for 2000 projections, or the ionization chamber reading for 2000 projections (Table 5.15).

Table 5.15 Calculated radiation dose delivered to the cadaver during sparse view imaging.

	Based on the luxel+ dosimeter dose calculation		Based on the ionization chamber reading	
	50% Projection PC-CT	25% Projection PC-CT	50% Projection PC-CT	25% Projection PC-CT
Dog 2	2516.13mSv	1258.10mSv	13189.85mSv	6594.93mSv
Dog 3	927.56mSv	463.83mSv	9634.45mSv	4817.23mSv
Dog 4	1387.85mSv	693.92mSv	12413.45mSv	6206.73mSv

5.5. Results from the experiment for objective 4: to develop a human positioning device for PC-CT imaging of human prostate in situ.

The final device is designed of x-ray friendly polycarbonate or polyethylene and lightweight aluminum (Figure 5.6). The hardware has not currently been constructed as the application for CLS shifts to test the hardware during PC-CT imaging was unsuccessful. However, the design is finalized and ready for construction. Once constructed, it has the capacity of keeping a phantom pelvis up to 50 kg in a stable upright position with less than 6.5 um vertical displacement while being rotated for taking projections. It keeps the pelvis tightly positioned in the vertical axis with the help of two sets of screws (4 screws/set) and will keep it in the same horizontal plane by allowing the pelvis to rest on the bottom surface of the holder.

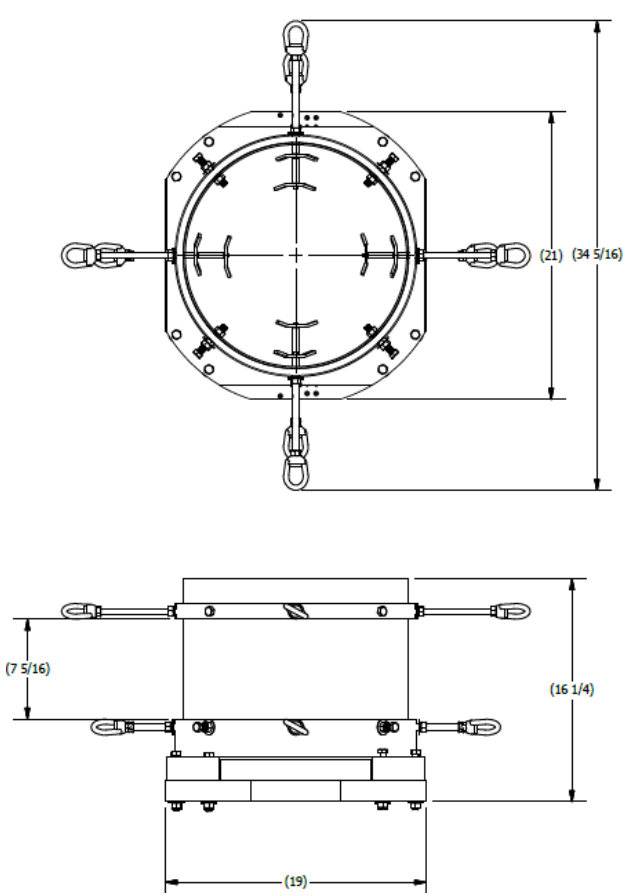

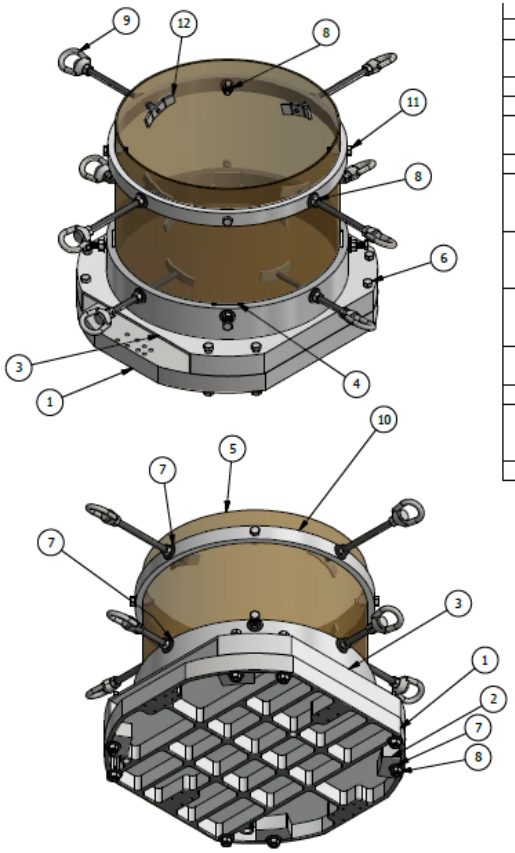

PARTS LIST

ITEM	QTY	PART NUMBER	DESCRIPTION
1	1	4410-02-0004	Pre-Base with additional 8 holes drilled on it
2	4	4410-02-1001	Additional slab for pre-base
3	1	4410-02-1002	Base
4	4	4410-02-1007	Push Clamp to keep plastic bucket in position from bottom
5	1	4410-02-1003	Plastic bucket
6	8	92198A685	Bolt for base and pre-base: 18-8 Stainless Steel Hex Head Screw 7/16"-14 Thread Size, 4" Long
7	24	90107A032	316 Stainless Steel Washer for 7/16" Screw Size, 0.5" ID, 1.125" OD
8	28	94895A817	High-Strength Steel Hex Nut Grade 8, Zinc Yellow-Chromate Plated, 7/16"-14 Thread Size
9	8	4410-02-0002	Assembly of long rod for holding sample
10	1	4410-02-1004	Upper rim
11	8	92240A365	Bolt for upper rim and lower rim: 18-8 Stainless Steel Hex Head Screw 7/16"-14 Thread Size, 1-1/2" Long
12	8	4410-02-1008	Tongue to hold sample

Figure 5.6 Picture showing the 2D and 3D images of the final assembly of the pelvic holder (measurement units in inch).

6. Discussion

Overall

Although the cellular details and visibility of micro-structures required to distinguish the clinical conditions of prostate disease such as nuclear and nucleolar enlargement and broaching of basal layer, presence of a small gland or group of glands around any nerve bundle and absence of a rim of connective tissue between the adjacent glands indicating prostate cancer (Brawer, 2005; Humphrey, 2007; Brustmann, 2015), or budding and branching of the duct-acini system and bi-layered epithelial lining with outer cuboidal cells and inner tall columnar cells indicating BPH (McNeal, 1965, 1988), were not achieved with any of the tested imaging modalities, results here support synchrotron in-line PC-CT as an imaging modality with high potential for non-invasive diagnosis of prostate conditions. MRI and US provided overall less reliable assessments, although none of these three modalities appeared to be equal to histology in identifying different structures and areas in prostate tissues. Some of the potential sources of errors couldn't be neglected in discussing the results. One of the potential sources could be the tissue processing techniques and handling of the samples throughout the different imaging experiments, e.g. radiation damage of the tissue during PC-CT (though noticeable changes were not observed), imperfect parallel slicing of gelatin blocks for histological processing, unavoidable probability of minute misalignment and/or mismatching of the images from the various methodologies for comparison. The remainder of the potential errors have been explained throughout the discussion section in the appropriate places. Though histology was considered as a reference modality in this study as considered by others (Liu et al., 2009; He et al., 2012; Isebaert et al., 2013) for comparison, it is also not a perfect modality itself. Physical alterations such as shearing effect as well as the biochemical effect due to fixation, embedding and staining necessary in histology might have potentially hindered the correct diagnosis of structures and lesions and their correct size measurement (Taqi et al., 2018).

In our study, it was found that PC-CT correctly identified 26.4% of the structures while MRI and US only identified 6.7% and 2%, respectively. PC-CT was significantly closer, than MRI and US, to histology in ability to identify structures and areas correctly. Comparing MRI and US to each other, MRI was closer to histology in ability to identify structures and areas correctly. A study on

canine prostates at the CLS BMIT-BM beamline had given similar results. In that study, US had given very poor structural visualizations, and while MRI produced comparatively better soft-tissue contrast, neither modality was able to provide as detailed information as PC-CT could for different tissues like urothelial lining, ducts, acini, adipose tissue, muscular structure, fibromuscular stroma, etc. (Barboza et al., 2012; Montgomery et al., 2013; Montgomery et al., 2016). In addition, our study found that a total of 5.3% of the visible structures appeared combined in PC-CT while in MRI and US, it was 38.8% and 30.8% of the total visible structures, respectively indicating higher spatial resolution (power of resolving two nearby structures) with PC-CT.

Possible reasons behind the superiority of PC-CT: In conventional CT, usually, the contrast resolution is not considered to be intrinsically good as the attenuation properties of different soft tissues are not so different from each other (Lin & Alessio, 2009). However, the total contrast achieved here in PC-CT images was improved likely from the additional (phase) contrast generated due to the phase shift of the beam as the X-rays pass through the soft tissue and the long-distance propagation (1.5 m) of the X-rays between the sample and the detector (Chapman et al., 1997; Lewis, 2004a) i.e. through the edge enhancement of different tissues. This phase-based imaging is, therefore, more sensitive to even a small difference in densities making it more useful and more informative in imaging soft tissue (Chapman et al., 1997; Lewis, 2004b). The spatial resolution we measured was 12.49 µm in PC-CT, which is superior to the 1.2 mm resolution usually measured with most MRI images (Lin & Alessio, 2009). One of the reasons for the higher spatial resolution in PC-CT images was the smaller source size (focal spot) of the beam, because smaller source size reduce the penumbral blurring in an X-ray image (Nagesh et al., 2016), giving better image quality and higher resolution. The highly collimated and brilliant X-rays also contribute to higher spatial resolution (Giuliani et al., 2017). A synchrotron facility is the only place where we can meet all these criteria (Izadifar et al., 2017b). Similarly, the smaller pixel size (higher spatial sampling) and direct detection system (less blurring) of the CMOS detector (Scott et al., 2012) to capture the variation in x-ray intensity due to the refraction and interaction of the beam could contribute to the higher spatial resolution and better-quality images in our study.

Possible reasons behind the differences with MRI: Compared to PC-CT, MRI resulted in decreased resolution of the fine structures. The different soft tissue structures were not well differentiated in MRI, enabling correct identification of only one quarter of the structures

identifiable in PC-CT. Similarly, it was difficult to discern closely located, similar structures, which was likely because of decreased spatial resolution (Reddy, 2005; Reeth et al., 2012) and larger voxel size resulting in a poorer signal to noise ratio. Almost seven times more structures appeared combined in the MRI images compared to PC-CT images. But just the image resolution might not be the reasons behind the results with MRI compared to PC-CT. In MRI, the interpretation can vary depending on the type of software and machine being used as well as the experience of the examiner. We had access to a 1.5 Tesla machine for our imaging but the use of a MRI machine with a stronger magnetic field would have given a greater signal to noise ratio and so the better spatial resolution and soft-tissue contrast (Lawrentschuk & Fleshner, 2009; Thompson et al., 2013; Pedler, et al., 2015). If we were performing in-vivo physiological imaging there would be an option to use spin-echo/anatomical sequences along with advanced functional sequences such as diffusion-weighted imaging and dynamic contrast-enhanced imaging for better visualization and interpretation of the pathological condition. However, our study was on excised tissue therefore we were limited to using only spin-echo/anatomical sequences (T1 ad T2) which could also be one of the reasons our results were inferior to PC-CT. The T1 and T2 weighted sequences are able to identify mostly the anatomic abnormalities rather than the physiologically altered pathology. Underlying diffusivity (with blood, water, or any kind of fluid) would be more appreciated in diffusion weighted MRI sequences than the anatomical sequences. Moreover, the spin-echo/anatomical MRI sequences are not good in differentiation of benign and malignant neoplastic conditions, mainly because of being poor in distinguishing lymphatic tissue (which is usually the first tissue to be metastasized) from tumors due to similar relaxation times and proton densities. It is also challenging to differentiate the cystic lesions from solid lesions without the adequate fat suppression possible with the spin-echo/anatomical sequences MRI. (Beets-Tan, 2010; Ha et al., 2017; Hamm et al., 2007).

Possible reasons behind the differences of US: The use of US resulted in the most reduced image quality in terms of identifying different structure and pathological lesions inside prostate tissues. As indicated earlier, US only identified 2% of the total structures correctly and out of those correctly identified structures, 30.8% structures appeared combined with similar other structures. One of the reasons behind this result from US, as compared to PC-CT and MRI, could be a small difference (less than 10%) of the speed of the ultrasound in the different soft tissues (Hayward, 2012). The small difference in ultrasound velocity accounts for only a small difference in acoustic

properties (echos) of the tissues that results in poor contrast in an image to differentiate different structures (Tole et al., 2005). Similarly, too many inherent artifacts in US images could be other reasons for the weaker diagnostic quality images in our study. Some of these artifacts are beam width artifact (where the highly refractive object located within the wide beam but outside of the transducer margin at the depth below the focal point will be displayed as if the object is located within the narrow imaging plane of transducer), reverberation artifact (where the US image is formed assuming an echo returned from multiple bouncing in between multiple parallel layers of tissues as an echo reflected from a single reflection) and speed displacement artifact (where the US imaging system processes an image assuming the same constant speed of the ultrasound waves (1540 m/sec) even though the ultrasound has different velocities in different tissue) (Feldman et al., 2009). Moreover, there is an unavoidable probability that the chosen US images might be a non-exact match to the histology images because of the step size limitation of US machine used. It could only capture images 40 µm apart from each other, missing the areas in between. Similarly, image resolution does not stay the same throughout the region between the surface and depth of the tissue. Axial resolution (ability to discern two adjacent structures that are longitudinally parallel to the ultrasound wave) deteriorates for the deeper parts in the image (Ng & Swanevelder, 2011). Also, the interpretation can vary depending on the type of software and machine being used as well as the experience of the examiner. Placing the probe in a slightly different position and slightly different angle will give a different view. Similarly, the different adjustment of gain, contrast, focal points affects the images produced (Chu et al., 2014; Tole et al., 2005; Wiafe & Badu-Peprah, 2019). All of these factors might have played in making US images less efficient in identifying and characterizing the different structures and pathological lesions in our study. Beside the unavoidable inherent artifacts, the whole experiment and images evaluation were done by a single person, with same machine and setting to lessen the errors as much as possible.

The possible error from all the modalities could be reduced to some extent if whole prostate glands could have been used instead of the TURP tissues. A single bigger tissue mass would have had a firmer integrity than the gelatin, and so possibly would have resulted in less misalignment during sample processing for the different modalities, especially histology. Also, for the histological examination, a larger area of the prostate to evaluate may have made the diagnosis of different pathological lesions easier by evaluating focal as well as surrounding areas.

Structures and their size measurement: In PC-CT, the area of mineralization was the most often correctly identified (in agreement with histology) structure but none of the mineralization was identified in MRI and US. This finding is in agreement with what we expect from clinical X-ray imaging (regular radiographs or CT), MRI and US. We can expect very distinct high-density spots from mineralized structures even in regular radiographs. CT is sensitive to the mineralized structures (Freire et al., 2018) such that it is almost impossible to miss any such structures in the examination of an image. We found the same pattern here in PC-CT. This result might be because of the high absorption coefficient of the mineralized tissue along with the X-ray phase shift that propagates during PC-CT imaging. On the contrary, we didn't identify any of the mineralization in the MRI or US imaging. The variation in the signal intensities in the anatomical sequences, especially for calcifications, can give misleading appearances in MRI such as inflammatory spots or fluid signals around them resulting in the calcifications remaining unnoticed. Similarly, the acoustic shadowing (the dark area just behind a highly sound-reflective or absorbing object hinders the US in making the correct interpretation for mineralized structures and their surroundings (Freire et al., 2018; Nörenberg et al., 2016; Rupp, Seil, & Kohn, 1998). These factors could contribute to the poor outcomes with MRI and US in our study. With the MRI, only cysts, lymphatics, and blood vessels were correctly identified. These structures most of the time, are hollow, and if not, the inner cavity is occupied with fluid and is not a solid structure. This implies that the anatomical sequence MRI we used was able to identify only those structures which have a very drastic difference in physical nature between the outer tunic and the inside portion. In the US, cysts were the only kind of structure correctly identified.

Comparison of the sizes of different structures from different imaging modalities was one of the goals of the study. Reliability in giving the accurate measurement of different structures and lesions is important for clinical purposes, if PC-CT is to be made clinically applicable in future. There was no difference in the size of cysts measured from histology, PC-CT, MRI, and US, which signifies that the size measurements of detectable cysts do not differ in different modalities. These cysts that were visible in histology and in any of the imaging modalities (PC-CT, MRI, US) are larger than the cysts detectable only in histology. The visible histological presence of these small cysts which were undetectable in the other imaging modality but were in the histology suggests that smaller structures are less likely to be visible in these imaging modalities than in histology, and so would be missed in a non-histological assessment.

Sparse view PC-CT: One method to image with a low dose of radiation and in a short timeframe is to decrease the projection numbers while imaging, i.e. sparse view technique. We had imaged our samples with 2250 projections but also reconstructed the PC-CT images with equally spaced 1125 and 562 projections. With 100% projection PC-CT, we correctly identified 22.4% of the total structures while in 50% and 25% projection PC-CT, it was only 18.9% and 32 10.3% respectively. The 100% projection PC-CT was found significantly more powerful than 50% and 25% projection PC-CT and 50% projection PC-CT was found powerful than 25% Projection PC-CT in correctly diagnosing structures and areas. Some of the reasons might be the serious streak artifacts and blurring that were evident in the PC-CT images reconstructed from a lesser number of projections (Barrett & Keat, 2004; Melli et al., 2016). Low signal to noise ratio might be another reason (Lin et al., 2018). Moreover, in our study, a total of 6.8% and 8.1% of the visible structures appeared combined in 100% and 50% PC-CT respectively while in 25% PC-CT, 14.3% of the visible structures appeared combined. This indicates the power of resolving two nearby structures is almost the same in 100% and 50% PC-CT but is almost half in 25% PC-CT. This suggests that the100% and 50% projection PC-CT resulted in a similar amount of phase-contrast while the 50% projection PC-CT was providing a comparatively low amount of phase-contrast, not sufficient enough to discern two closely placed, similar structures as with the 100% and 50% projection PC-CT (Izadifar et al., 2017a). Additionally, with 25% projection PC-CT, we could not detect any of the glandular areas which were otherwise detected in 100% and 50% projection PC-CT. All of these findings are in agreement with the findings from a previous study conducted at the CLS Biomedical Imaging and Therapy bending-magnet (BMIT-BM) beam-line accessing the implanted cardiac patches on a rat heart (Izadifar et al., 2017a). In that study, CT reconstructions were separately done with 3000, 1500, 1000 and 750 projections. They observed that the anatomical features in tomographic images were well visualized even in the image from low projection numbers, i.e. 1500, but it was difficult to identify the microstructure with 1000 and 750 projections.

Radiation dose: Our findings support that the PC-CT is closer-to-histology imaging technique than the other conventional medical imaging techniques for imaging prostate tissues. However, that doesn't solely define the usefulness of the technique in clinical use. Another important factor

that needs to be considered before thinking to implement the imaging technique for clinical use is the dose imparted while imaging. Though the image contrast developed in phase contrast imaging is not due to the radiation absorption by the tissue that is imaged, the amount of radiation absorbed is definitely an issue of concern. If the technique is depositing a harmful radiation dose while imaging, then it will be a significant limitation of PC-CT and it is not useful beyond ex-vivo imaging. While we did not measure the radiation imparted in our TURP tissue samples while imaging, we did collect dose data while imaging canine prostates in-situ in the BMIT-ID beamline.

A dose the dosimeter would record when placed behind a medium sized dog (~28 kg) such that the x-rays struck the dosimeter only after they pass through the cadaver is 0.16mSv/projection (from the calculation done in the methodology section). The delivered dose would be 1.11mSv/projection (averaged all the values of the third column of Table 5.14 and divided by 2000) when the dosimeter is placed directly in the beam. This indicates that a dosimeter would be radiated 6.9 times more whenever it was directly exposed to the beam compared to when the beam passed through the cadaver prior to hitting the dosimeter.

It was found that the Luxel+ dosimeter recorded an average equivalent radiation dose imparted in a medium-sized dog during PC-CT imaging of one view of 7.8 mm height with 2000 projections in the CLS BMIT-ID beamline of 3,221.1 mSv. This is equal to an effective dose of 1,481.7 mSv (taking into account the compartment factors (wc) of 0.460 for the abdomen/pelvis out of 1.000 for the whole body (ICRP, 2007). However, in human medicine, standard clinical x-ray examinations of various body parts usually deposit a radiation dose ranging from 0.01-10 mSv, while a standard clinical CT examination deposits a dose ranging between 2-20 mSv (Mettler et al., 2008). In a study performed in 1,119 adult human patients, it was found that the median effective dose for a routine abdomen-pelvis CT was 15 mSv (Smith-Bindman et al., 2009). Compared to these values, the doses delivered in the synchrotron PC-CT imaging has been found to be very high. Even higher doses were recorded by the ionization chambers simultaneously used with Luxel+ dosimeters. Average reading of the iodination chambers was 10.9Sv effective dose (23.5 Gy absorbed dose) which is approximately seven times higher than the chip dosimeter reading. The reason behind the higher reading by ionisation chambers has been difficult to find and is yet unknown. Similar high doses had been recorded in another related study of canine imaging with synchrotron PC-CT. The imaging was conducted in live dogs of an average weight

of 28kg at the CLS. The average effective radiation dose of 10120 mSv (22 Gy absorbed dose) was recorded by an ion chamber for 2000 projections over 180° (Cavalca Cardoso, 2019).

In our study, it was found that the effective dose would be reduced to half i.e., 740.9 mSv and one fourth i.e. 370.4 mSv if we performed sparse view imaging i.e. 50% projection PC-CT and 25% projection PC-CT, respectively. This is somewhat close in agreement with the finding of a study of accessing the implanted cardiac patches on a rat heart (Izadifar et al., 2017a). In this study, different 3000, 1500, 1000 and 750 projections images were collected throughout the 180-degree rotation. The absorbed X-ray dose (measured by ionization chamber) imparted while imaging with 3000 projections with 25 KeV monochromatic beam in the BMIT-BM beamline was 256mSv. With 50% projection PC-CT and 25% projection PC-CT, it was reduced to 128 mSv and 64 mSv respectively. But even after reducing the dose to one fourth, the doses recorded in these studies are still hazardous with the potential to induce cancer later in life in approximately 0.5 % of the patients if the imaging was done in humans (CCOHS, 2019). These findings indicate that synchrotron PC-CT imaging, though superior in providing high-resolution image quality, needs to be further studied to make it clinically applicable. Besides the extremely high radiation dose there are other major difficulties and limitations in transforming the synchrotron inline PC-CT technique into a clinical diagnostic tool for live human imaging. These include a small field of view resulting in longer imaging times for a larger area, difficulties in keeping the human body in an upright position, associated vertical movement and motion artifact and the interference caused by the denser structures such as vertebra and other bones.

Pelvic holder: We designed a pelvis holder made up of polycarbonate/polyethylene containers of 41.2 cm internal diameter and the rest of the parts were designed to be made up of aluminum. It was designed to use for the simulation of the in-vivo imaging of the human prostate as a next step research of this ex-vivo prostate tissue imaging. Due to additional imaging shifts not being available at the CLS (due to the long shut down of the CLS facility from the technical problem, and due to the high numbers of research proposal applicants for next imaging cycle after the facility came into operation), we didn't construct the hardware. But this design is complete and ready to be constructed and tested to determine if it will perform as designed during PC-CT imaging of a human pelvis/phantom at the CLS.

7. Conclusion

7.1.Overview

Since the advent of synchrotron X-ray imaging, there has not been one study done on human prostate research tissue. The main objective of this thesis was to examine the ability of synchrotron-based in-line propagation phase-contrast computerized tomography (PC-CT) to characterize and differentiate various structural features and pathological lesions within human prostatic tissue samples in comparison to US, MRI, and histology. PC-CT is proven to be a significantly powerful (closer-to-histology) imaging technique compared to MRI and US in identifying mini-structures and areas within human prostate tissue samples. PC-CT identified almost four times and 15 times more structures than MRI and US respectively. Power to resolve nearby similar structures was also higher in PC-CT indicating higher spatial resolution and edge enhancement. Area of mineralization and cystic acini were the most often correctly identified pathological structures in PC-CT. It was also found that the size of a structure matters whether it will be visualized in PC-CT, MRI, and US. Smaller sized structures are less likely to appear in these imaging modalities.

PC-CT images from a 2250 projections (100%) are superior in image quality than images from 1125 (50%) and 562 (25%) projection PC-CT, with 50% projection PC-CT more powerful than 25% PC-CT, in terms of visualizing the different structures and areas. There was a drastic difference in image quality between 50% projection PC-CT and 25% projection PC-CT than between 100% projection PC-CT and 50% projection PC-CT. The pattern was same in terms of power of resolving nearby similar structures too. This indicates we could reduce to a lower number of projections to decrease the radiation dose imparted in specimens but at the same time, but there will be a trade-off with image quality.

Though the image quality achieved with the synchrotron PC-CT imaging seems promising for future development for clinical use, the radiation dose imparted during the imaging was very high compared to a standard clinical CT examination. Even the less powerful 50% or 25% projection PC-CT were calculated to provide doses above the acceptable limit and considered hazardous.

7.2.Future directions

The results (images, corresponding data and their analysis) from this work indicate that synchrotron radiation-based inline PC-CT is a promising technique that offers improved non-invasive diagnostic imaging of prostate tissue. Our results give more confidence for future researchers to conduct studies into in-vivo prostate imaging along with the evaluation of the corresponding radiation dose to evaluate the usefulness of the PC-CT technique and also with the attempt to reduce the radiation doses for clinical application in future.

8. Works Cited

Adams, B. (2013). PSA Screening. *AJN, American Journal of Nursing*, *113*(8), 13-13. https://doi.org/10.1097/01.NAJ.0000432943.11972.49

Akin, O., & Hricak, H. (2007). Imaging of Prostate Cancer. In *Radiologic Clinics of North America* 45(1), 207–222. https://doi.org/10.1016/j.rcl.2006.10.008

Anand, P., Kunnumakkara, A. B., Kunnumakara, A. B., Sundaram, C., Harikumar, K. B., Tharakan, S. T., Lai, O. S., Sung, B., & Aggarwal, B. B. (2008). Cancer is a preventable disease that requires major lifestyle changes. *Pharmaceutical Research*, *25*(9), 2097–2116. https://doi.org/10.1007/s11095-008-9661-9

Arfelli, F., Assante, M., Bonvicini, V., Bravin, A., Cantatore, G., Castelli, E., Dalla Palma, L., Di Michiel, M., Longo, R., Olivo, A., Pani, S., Pontoni, D., Poropat, P., Prest, M., Rashevsky, A., Tromba, G., Vacchi, A., Vallazza, E., & Zanconati, F. (1998). Low-dose phase contrast x-ray medical imaging. *Physics in Medicine and Biology, 43, 2845-2852*. https://doi.org/10.1088/0031-9155/43/10/013

Arfelli, Fulvia, Bonvicini, V., Bravin, A., Cantatore, G., Castelli, E., Palma, L. D., Michiel, M. Di, Fabrizioli, M., Longo, R., Menk, R. H., Olivo, A., Pani, S., Pontoni, D., Poropat, P., Prest, M., Rashevsky, A., Ratti, M., Rigon, L., Tromba, G., … Zanconati, F. (2000). Mammography with Synchrotron Radiation: Phase-Detection Techniques. *Radiology*, 215(1), 286-93. https://doi.org/10.1148/radiology.215.1.r00ap10286

Ayala, A. G., Ro, J. Y., Babaian, R., Troncoso, P., & Grignon, D. J. (1989). The prostatic capsule: Does it exist? Its importance in the staging and treatment of prostatic carcinoma. In *American Journal of Surgical Pathology*, 13 (1), 21–27.

Balk, S. P., Ko, Y.-J., & Bubley, G. J. (2003). Biology of prostate-specific antigen. *Journal of Clinical Oncology : Official Journal of the American Society of Clinical Oncology*, *21*(2), 383–391. https://doi.org/10.1200/JCO.2003.02.083

Banerjee, P. P., Banerjee, S., Brown, T. R., & Zirkin, B. R. (2018). Androgen action in prostate function and disease. *American Journal of Clinical and Experimental Urology*, *6*(2), 62–77.

Barboza, T., Pettitt, M., Snead, E., Singh, J., Montgomery, J., Belev, G., Wei, Z., Chibbar, R., Visvanathan, K., Pierson, R., Boire, S., El-Gayed, A., Buhr, M., & Adams, G. (2012,

September 4). *Comparative Analysis of Ultrasound, CT and Phase Contrast CT of Canine and Human Prostatic Tissue.* Undergraduate Student Poster Day, Western College of Veterinary Medicine, University of Saskatchewan, Saskatoon, SK.

Barentsz, J. O., Richenberg, J., Clements, R., Choyke, P., Verma, S., Villeirs, G., Rouviere, O., Logager, V., & Fütterer, J. J. (2012). ESUR prostate MR guidelines 2012. *European Radiology*, *22*(4), 746–757. https://doi.org/10.1007/s00330-011-2377-y

Barrett, J. F., & Keat, N. (2004). Artifacts in CT: Recognition and Avoidance. *RadioGraphics*, 24(6), 1679-91. https://doi.org/10.1148/rg.246045065

Beets-Tan, R. G. H. (2010). *MRI of the gastrointestinal tract* (J. Stoker & A. L. Baert, Eds.). Berlin, Springer. Retrieved on Jan. 22, 2020 from https://link-springer-com.cyber.usask.ca/content/pdf/10.1007%2F978-3-540-85532-3.pdf

Berger, A. (2002). Magnetic resonance imaging. *BMJ : British Medical Journal*, *324*(7328), 35.

Berry, S. J., Coffey, D. S., Walsh, P. C., & Ewing, L. L. (1984). The development of human benign prostatic hyperplasia with age. *The Journal of Urology*, *132*(3), 474–479. https://doi.org/10.1016/s0022-5347(17)49698-4

Bhavsar, A., & Verma, S. (2014). Anatomic imaging of the prostate. *BioMed Research International*, *2014*, 1-9. https://doi.org/10.1155/2014/728539

Bisby, M., & Maitland, P. (2005). CIHR Research: Re-Inventing the Microscope: The Canadian Light Source (CLS). *Healthcare Quarterly*, *8*(2), 22–23. https://doi.org/10.12927/hcq..17051

Bonekamp, D., Jacobs, M. A., El-Khouli, R., Stoianovici, D., & Macura, K. J. (2011). Advancements in MR Imaging of the Prostate: From Diagnosis to Interventions. *RadioGraphics*, *31*(3), 677–703. https://doi.org/10.1148/rg.313105139

Brawer, M. K. (2005). Prostatic intraepithelial neoplasia: An overview. *Reviews in Urology*, *7 (*3), S11–8. https://www.ncbi.nlm.nih.gov/pmc/articles/PMC1477603

Bray, F., Ferlay, J., Soerjomataram, I., Siegel, R. L., Torre, L. A., & Jemal, A. (2018). Global cancer statistics 2018: GLOBOCAN estimates of incidence and mortality worldwide for 36 cancers in 185 countries. *CA: A Cancer Journal for Clinicians*, *68*(6), 394–424. https://doi.org/10.3322/caac.21492

Brustmann, H. (2015). p40 as a Basal Cell Marker in the Diagnosis of Prostate Glandular Proliferations: A Comparative Immunohistochemical Study with 34betaE12. *Pathology Research International*, *2015*, 897927. https://doi.org/10.1155/2015/897927

Burattini, E., Cossu, E., Di Maggio, C., Gambaccini, M., Indovina, P. L., Marziani, M., Pocek, M., Simeoni, S., & Simonetti, G. (1995). Mammography with synchrotron radiation. *Radiology*, 195(1), 239 -244. https://doi.org/10.1148/radiology.195.1.7892478

Calle, E. E., Rodriguez, C., Walker-Thurmond, K., & Thun, M. J. (2003). Overweight, Obesity, and Mortality from Cancer in a Prospectively Studied Cohort of U.S. Adults. *New England Journal of Medicine*, *348*(17), 1625–1638. https://doi.org/10.1056/NEJMoa021423

Cavalca Cardoso, N. (2019). *Development of Synchrotron Based Imaging Tools for Benign Prostatic Hyperplasia Using an Induced Canine Model* [Thesis, University of Saskatchewan]. Retrieved on Jan. 22, 2020 from https://harvest.usask.ca/handle/10388/12354

CCOHS. (2019, December 18). *Radiation - Quantities and Units of Ionizing Radiation: OSH Answers*. http://www.ccohs.ca/

Chapman, D., Thomlinson, W., Johnston, R. E., Washburn, D., Pisano, E., Gmür, N., Zhong, Z., Menk, R., Arfelli, F., & Sayers, D. (1997). Diffraction enhanced x-ray imaging. *Physics in Medicine and Biology 42(11), 2015-2025*. https://doi.org/10.1088/0031-9155/42/11/001

Chu, D., Chen, R.-C., Hung, S.-T., & Chou, P. (2014). Physician and patient characteristics affecting repeat use of abdominal ultrasound: A nationwide population-based study. *Journal of the Chinese Medical Association*, *77*(2), 89–94. https://doi.org/10.1016/j.jcma.2013.10.010

COLLINS, M. M., STAFFORD, R. S., O'LEARY, M. P., & BARRY, M. J. (1998). HOW COMMON IS PROSTATITIS? A NATIONAL SURVEY OF PHYSICIAN VISITS. *The Journal of Urology*, *159*(4), 1224–1228. https://doi.org/10.1016/S0022-5347(01)63564-X

Cooner, W. H., Mosley, B. R., Rutherford, C. L., Beard, J. H., Pond, H. S., Terry, W. J., Igel, T. C., & Kidd, D. D. (1990). Prostate cancer detection in a clinical urological practice by ultrasonography, digital rectal examination and prostate specific antigen. *The Journal of Urology*, *143*(6), 1146–1152.

Das, M. (2017). Androgen deprivation therapy for prostate cancer. *The Lancet Oncology*, *18*(10), 567. https://doi.org/10.1016/S1470-2045(17)30670-8

Djavan, B., Zlotta, A., Kratzik, C., Remzi, M., Seitz, C., Schulman, C. C., & Marberger, M. (1999). PSA, PSA density, PSA density of transition zone, free/total PSA ratio, and PSA velocity for early detection of prostate cancer in men with serum PSA 2.5 to 4.0 ng/mL. *Urology*, *54*(3), 517–522. https://doi.org/10.1016/S0090-4295(99)00153-3

Eichler, K., Hempel, S., Wilby, J., Myers, L., Bachmann, L. M., & Kleijnen, J. (2006). Diagnostic Value of Systematic Biopsy Methods in the Investigation of Prostate Cancer: A Systematic Review. *The Journal of Urology*, *175*(5), 1605–1612. https://doi.org/10.1016/S0022-5347(05)00957-2

Elfarnawany, M., Rohani, S. A., Ghomashchi, S., Allen, D. G., Zhu, N., Agrawal, S. K., & Ladak, H. M. (2017). Improved middle-ear soft-tissue visualization using synchrotron radiation phase-contrast imaging, 354, 1-8. *Hearing Research*. https://doi.org/10.1016/j.heares.2017.08.001

ElShafei, A., Li, Y.-H., Hatem, A., Moussa, A. S., Ethan, V., Krishnan, N., Li, J., & Jones, J. S. (2013). The utility of PSA velocity in prediction of prostate cancer and high grade cancer after an initially negative prostate biopsy. *The Prostate*, *73*(16), 1796–1802. https://doi.org/10.1002/pros.22718

Epstein, J. I., Egevad, L., Amin, M. B., Delahunt, B., Srigley, J. R., & Humphrey, P. A. (2015). The 2014 International Society of Urological Pathology (ISUP) Consensus Conference on Gleason Grading of Prostatic Carcinoma. *The American Journal of Surgical Pathology*, 41(4), e1-e7. https://doi.org/10.1097/PAS.0000000000000530

Feldman, M. K., Katyal, S., & Blackwood, M. S. (2009). US Artifacts. *RadioGraphics*, *29*(4), 1179–1189. https://doi.org/10.1148/rg.294085199

Franklin, R. B., Feng, P., Milon, B., Desouki, M. M., Singh, K. K., Kajdacsy-Balla, A., Bagasra, O., & Costello, L. C. (2005a). HZIP1 zinc uptake transporter down regulation and zinc depletion in prostate cancer. *Molecular Cancer*, *4*, 32-32. https://doi.org/10.1186/1476-4598-4-32

Franklin, R. B., Milon, B., Feng, P., & Costello, L. C. (2005). Zinc and zinc transporters in normal prostate and the pathogenesis of prostate cancer. *Frontiers in Bioscience : A*

Journal and Virtual Library, *10*, 2230–2239. https://doi.org/10.1016/j.ygyno.2014.12.035.Pharmacologic

Franz, M.-C., Anderle, P., Bürzle, M., Suzuki, Y., Freeman, M. R., Hediger, M. A., & Kovacs, G. (2013). Zinc transporters in prostate cancer. *Molecular Aspects of Medicine*, *34*(2–3), 735–741. https://doi.org/10.1016/j.mam.2012.11.007

Frauscher, F., Klauser, A., Volgger, H., Halpern, E. J., Pallwein, L., Steiner, H., Schuster, A., Horninger, W., Rogatsch, H., & Bartsch, G. (2002). Comparison of contrast enhanced color Doppler targeted biopsy with conventional systematic biopsy: Impact on prostate cancer detection. *The Journal of Urology*, *167*(4), 1648–1652.

Freire, V., Moser, T. P., & Lepage-Saucier, M. (2018). Radiological identification and analysis of soft tissue musculoskeletal calcifications. *Insights into Imaging*, *9*(4), 477–492. https://doi.org/10.1007/s13244-018-0619-0

Giuliani, A., Mazzoni, S., Mele, L., Liccardo, D., Tromba, G., & Langer, M. (2017). Synchrotron Phase Tomography: An Emerging Imaging Method for Microvessel Detection in Engineered Bone of Craniofacial Districts. *Frontiers in Physiology*, *8, 769-769.* https://doi.org/10.3389/fphys.2017.00769

Goldman, L. W. (2007). Principles of CT and CT technology. *Journal of Nuclear Medicine Technology*, *35*(3), 115–128. https://doi.org/10.2967/jnmt.107.042978

Gossner, J. (2012). Computed Tomography of The Prostate-A Review, *Internet scientific publications. Retrieved on Jan. 22, 2020 from http://ispub.com/IJRA/14/1/14086*

Government of Canada, S. C. (2019, April 17). *Recent trends in prostate cancer in Canada*. Retrieved on Jan. 22, 2020 from https://www150.statcan.gc.ca/n1/pub/82-003-x/2019004/article/00002-eng.htm

Grochulski, P., Fodje, M., Labiuk, S., Wysokinski, T. W., Belev, G., Korbas, M., & Rosendahl, S. M. (2017). Review of Canadian Light Source facilities for biological applications. *Nuclear Instruments and Methods in Physics Research Section B: Beam Interactions with Materials and Atoms*, *411*, 17–21. https://doi.org/10.1016/J.NIMB.2017.01.065

Gui, J., Zou, J., Rong, J., Hu, Z., Zhang, Q., Zheng, H., & Xia, D. (2012). Investigation of the effect of tube voltage and imaging geometry on phase contrast imaging for a micro-CT system. *Nuclear Instruments and Methods in Physics Research, Section A: Accelerators,*

Spectrometers, Detectors and Associated Equipment, 669, 97-102. https://doi.org/10.1016/j.nima.2011.10.050

Ha, R., Comstock, C. E., & Morris, E. (2017). *Breast MRI teaching atlas*. Retrieved on Jan. 22, 2020 from https://link-springer-com.cyber.usask.ca/content/pdf/10.1007%2F978-1-4939-6409-3.pdf

Hallin, E., de Jong, M., Ellis, T., Thomlinson, W., & Dalzell, M. (2006). Synchrotron Radiation News Technical Report: Canadian Light Source Facility Update. *Synchrotron Radiation News*, *19*(6), 7–12. https://doi.org/10.1080/08940880601064950org/10.1080/08940880601064950

Hamilton, W., & Sharp, D. (2004). Symptomatic diagnosis of prostate cancer in primary care: A structured review. *The British Journal of General Practice : The Journal of the Royal College of General Practitioners*, *54*(505), 617–621.

Hamm, B., Forstner, R., & Beinder, E. (Eds.). (2007). *MRI and CT of the female pelvis*. Berlin, Springer.

Harris, W. P., Mostaghel, E. A., Nelson, P. S., & Montgomery, B. (2009). Androgen deprivation therapy: Progress in understanding mechanisms of resistance and optimizing androgen depletion. In *Nature Clinical Practice Urology*, 6(2), 76–85. https://doi.org/10.1038/ncpuro1296

Hartwig, V., Giovannetti, G., Vanello, N., Lombardi, M., Landini, L., & Simi, S. (2009). Biological effects and safety in magnetic resonance imaging: A review. *International Journal of Environmental Research and Public Health*, *6*(6), 1778–1798. https://doi.org/10.3390/ijerph6061778

Harvey, C. J., Pilcher, J., Richenberg, J., Patel, U., & Frauscher, F. (2012a). Applications of transrectal ultrasound in prostate cancer. *British Journal of Radiology*, *85*(SPEC. ISSUE 1), S3-S17. https://doi.org/10.1259/bjr/56357549

Hayward, N. (2012). BSAVA Manual of Canine and Feline Ultrasonography. *Journal of Small Animal Practice*, *53*(2), 3–3. https://doi.org/10.1111/j.1748-5827.2012.01183.x

Heijmink, S. W. T. P. J., van Moerkerk, H., Kiemeney, L. A. L. M., Witjes, J. A., Frauscher, F., & Barentsz, J. O. (2006). A comparison of the diagnostic performance of systematic versus ultrasound-guided biopsies of prostate cancer. *European Radiology*, *16*(4), 927–938. https://doi.org/10.1007/s00330-005-0035-y

He, L., Long, L. R., Antani, S., & Thoma, G. R. (2012). Histology image analysis for carcinoma detection and grading. *Computer Methods and Programs in Biomedicine*, *107*(3), 538–556. https://doi.org/10.1016/j.cmpb.2011.12.007

Herschman, J. D., Smith, D. S., & Catalona, W. J. (1997). Effect of ejaculation on serum toal and free prostate-specific antigen concentrations. *Urology*, *50*(2), 239–243. https://doi.org/10.1016/S0090-4295(97)00209-4

Ho, C. K. M., & Habib, F. K. (2011). Estrogen and androgen signaling in the pathogenesis of BPH. *Nature Reviews Urology*, *8*(1), 29–41. https://doi.org/10.1038/nrurol.2010.207

Huggins, C., & Hodges, C. V. (1941). Studies on prostatic cancer i. The effect of castration, of estrogen and of androgen injection on serum phosphatases in metastatic carcinoma of the prostate. *Cancer Research*, *1*(4), 293–297. https://doi.org/10.1111/j.1743-6109.2009.01680.x

Humphrey, P. A. (2007). Diagnosis of adenocarcinoma in prostate needle biopsy tissue. *Journal of Clinical Pathology*, *60*(1), 35–42. https://doi.org/10.1136/jcp.2005.036442

Hunter, D. T. (1968). Musculature of the prostate gland. *British Journal of Urology*, *40*(3), 278–287.

Ichael, M., & Arry, J. B. (2001). Clinical Practice P ROSTATE -S PECIFIC –A NTIGEN T ESTING FOR E ARLY D IAGNOSIS OF P ROSTATE C ANCER. *N Engl J Med*, *344*(18), 1373-1377. https://doi.org/10.1056/NEJM200105033441806

ICRP. (2007). The 2007 Recommendations of the International Commission on Radiological Protection. *ICRP Publication*, *103*(ICRP 37), 2–4.

Isebaert, S., Van den Bergh, L., Haustermans, K., Joniau, S., Lerut, E., De Wever, L., De Keyzer, F., Budiharto, T., Slagmolen, P., Van Poppel, H., & Oyen, R. (2013). Multiparametric MRI for prostate cancer localization in correlation to whole-mount histopathology. *Journal of Magnetic Resonance Imaging: JMRI*, *37*(6), 1392–1401. https://doi.org/10.1002/jmri.23938

Izadifar, M., Babyn, P., Chapman, D., Kelly, M. E., & Chen, X. (2017a). Potential of propagation-based synchrotron X-ray phase-contrast computed tomography for cardiac tissue engineering. *Journal of Synchrotron Radiation*, *24*(4), 842–853. https://doi.org/10.1107/S1600577517006208

Izadifar, M., Babyn, P., Chapman, D., Kelly, M. E., & Chen, X. (2017b). Potential of propagation-based synchrotron X-ray phase-contrast computed tomography for cardiac tissue engineering. *Journal of Synchrotron Radiation*, *24*(4), 842–853. https://doi.org/10.1107/S1600577517006208

J., A., A.R., H., & P., D. (1998). Urinary and bowel symptoms in men with and without prostate cancer: Results from an observational study in the Stockholm area. In *European Urology*, 33(1), 11–16.

J. Jagan Mohan. Reddy. (2005). *Step by step MRI*. London, New York, Taylor & Francis.

Jarvis, T. R., Chughtai, B., & Kaplan, S. A. (2014). Bladder Outlet Obstruction and BPH. *Current Bladder Dysfunction Reports*, *9*(4), 372–378. https://doi.org/10.1007/s11884-014-0263-6

Jia, Q. J., Chen, Y., Li, G., & Jiang, X. M. (2012). Optimization of the in-line X-ray phase-contrast imaging setup considering edge-contrast enhancement and spatial resolution. *Chinese Physics C, 36(3), 267-274*. https://doi.org/10.1088/1674-1137/36/3/014

Jung, K., Lein, M., Butz, H., Stephan, C., Loening, S. A., & Keller, T. (2006). New insights into the diagnostic accuracy of complexed and total prostate specific antigen using discordance analysis characteristics. *Journal of Urology*, *175*(4), 1275–1280. https://doi.org/10.1016/S0022-5347(05)00707-X

Kim, E. H., Larson, J. A., & Andriole, G. L. (2015). *Management of Benign Prostatic Hyperplasia*, *67, 137-151*. https://doi.org/10.1146/annurev-med-063014-123902

Krieger, J. N., Nyberg, L., & Nickel, J. C. (1999). NIH consensus definition and classification of prostatitis. *JAMA : The Journal of the American Medical Association*, *282*(3), 236–237. https://doi.org/10.1001/jama.282.3.236

Kumar, V. L., & Majumder, P. K. (1995). Prostate gland: Structure, functions and regulation. *International Urology and Nephrology*, *27*(3), 231–243. https://doi.org/10.1007/BF02564756

Lawrentschuk, N., & Fleshner, N. (2009). The role of magnetic resonance imaging in targeting prostate cancer in patients with previous negative biopsies and elevated prostate-specific antigen levels. *BJU International*, *103*(6), 730–733. https://doi.org/10.1111/j.1464-410X.2008.08205.x

Lee, A. G., Choi, Y. H., Cho, S. Y., & Cho, I. R. (2012). A prospective study of reducing unnecessary prostate biopsy in patients with high serum prostate-specific antigen with consideration of prostatic inflammation. *Korean Journal of Urology*, *53*(1), 50–53. https://doi.org/10.4111/kju.2012.53.1.50

Lee, C. H., Akin-Olugbade, O., & Kirschenbaum, A. (2011). Overview of Prostate Anatomy, Histology, and Pathology. *Endocrinology and Metabolism Clinics of NA*, *40*, 565–575. https://doi.org/10.1016/j.ecl.2011.05.012

Leissner, K. H., & Tisell, L. E. (1979). The weight of the human prostate. *Scandinavian Journal of Urology and Nephrology*, *13*(2), 137–142. https://doi.org/10.3109/00365597909181168

Lewis, R. A. (2004a). Medical phase contrast x-ray imaging: Current status and future prospects. *Physics in Medicine and Biology*, *49*(16), 3573–3583. https://doi.org/10.1088/0031-9155/49/16/005

Lewis, R. A. (2004b). Medical phase contrast x-ray imaging: Current status and future prospects. *Physics in Medicine and Biology*, *49*(16), 3573–3583. https://doi.org/10.1088/0031-9155/49/16/005

Lin, E., & Alessio, A. (2009). What are the basic concepts of temporal, contrast, and spatial resolution in cardiac CT? *Journal of Cardiovascular Computed Tomography*, *3*(6), 403–408. https://doi.org/10.1016/j.jcct.2009.07.003

Liu, T., Mansukhani, M. M., Benson, M. C., Ennis, R., Yoshida, E., Schiff, P. B., Zhang, P., Zhou, J., & Kutcher, G. J. (2009). A feasibility study of novel ultrasonic tissue characterization for prostate-cancer diagnosis: 2D spectrum analysis of in vivo data with histology as gold standard. *Medical Physics*, *36*(8), 3504–3511. https://doi.org/10.1118/1.3166360

Loch, T. (2007). Urologic imaging for localized prostate cancer in 2007. In *World Journal of Urology* 25(2), 121–129. https://doi.org/10.1007/s00345-007-0155-x

Madej, A., Wilkosz, J., Rózański, W., & Lipiński, M. (2012). Complication rates after prostate biopsy according to the number of sampled cores. *Central European Journal of Urology*, *65*(3), 116–118. https://doi.org/10.5173/ceju.2012.03.art3

McNeal, J. E. (1968). Regional morphology and pathology of the prostate. *American Journal of Clinical Pathology*, *49*(3), 347–357. https://doi.org/10.1093/ajcp/49.3.347

McNeal, J E. (1988). Normal histology of the prostate. *The American Journal of Surgical Pathology*, *12*(8), 619–633.

McNeal, John E. (1965). Morphogenesis of prostatic carcinoma. *Cancer, 18(12), 1659-1666*. https://doi.org/10.1002/1097-0142(196512)18:12<1659::AID-CNCR2820181223>3.0.CO;2-I

McVary, K. T. (2006). BPH: epidemiology and comorbidities. *The American Journal of Managed Care*, *12*(5), S122-S128.

Melli, S. A., Wahid, K. A., Babyn, P., Montgomery, J., Snead, E., El-Gayed, A., Pettitt, M., Wolkowski, B., & Wesolowski, M. (2016). A compressed sensing based reconstruction algorithm for synchrotron source propagation-based X-ray phase contrast computed tomography. *Nuclear Instruments and Methods in Physics Research Section A: Accelerators, Spectrometers, Detectors and Associated Equipment*, *806*, 307–317. https://doi.org/10.1016/j.nima.2015.10.013

Mettler, F. A., Huda, W., Yoshizumi, T. T., & Mahesh, M. (2008). Effective doses in radiology and diagnostic nuclear medicine: A catalog. *Radiology*, *248*(1), 254–263. https://doi.org/10.1148/radiol.2481071451

Michaelson, M. D., Cotter, S. E., Gargollo, P. C., Zietman, A. L., Dahl, D. M., & Smith, M. R. (2008). Management of complications of prostate cancer treatment. *CA: A Cancer Journal for Clinicians*, *58*(4), 196–213. https://doi.org/10.3322/CA.2008.0002

Mistry, K., & Cable, G. (2003). Meta-analysis of prostate-specific antigen and digital rectal examination as screening tests for prostate carcinoma. *The Journal of the American Board of Family Practice*, *16*(2), 95–101. https://doi.org/10.3122/JABFM.16.2.95

Mitterberger, M., Horninger, W., Aigner, F., Pinggera, G. M., Steppan, I., Rehder, P., & Frauscher, F. (2010). Ultrasound of the prostate. *Cancer Imaging*, *10*(1), 40–48. https://doi.org/10.1102/1470-7330.2010.0004

Mobilio, S., Boscherini, F., & Meneghini, C. (Eds.). (2015). *Synchrotron Radiation*, 3-28, Berlin, Springer https://doi.org/10.1007/978-3-642-55315-8

Montgomery, J., Barboza, T., Pettitt, M., Singh, J., Snead, E., Babyn, P., Belev, G., Wei, Z., Chibbar, R., Visvanathan, K., Boire, S., Chapman, D., El-Gayed, A., Buhr, M., & Adams, G. (2013, February 12). *Comparison of synchrotron phase contrast computed tomography with 3T magnetic resonance imaging, computed tomography, diagnostic*

ultrasound and histopathology of normal and diseased ex vivo canine and human prostates. The Royal Society, London, UK.

Montgomery, J. E., Wesolowski, M. J., Wolkowski, B., Chibbar, R., Snead, E. C. R., Singh, J., Pettitt, M., Malhi, P. S., Barboza, T., & Adams, G. (2016). Demonstration of synchrotron x-ray phase contrast imaging computed tomography of infiltrative transitional cell carcinoma of the prostatic urethra in a dog. *Journal of Medical Imaging (Bellingham, Wash.)*, *3*(1), 015504-015504. https://doi.org/10.1117/1.JMI.3.1.015504

Moyer, V. A. (2012). Screening for prostate cancer: U.S. preventive services task force recommendation statement. In *Annals of Internal Medicine* 157(2), 120–134. https://doi.org/10.7326/0003-4819-157-2-201207170-00459

Murphy, G., Haider, M., Ghai, S., & Sreeharsha, B. (2013). The expanding role of MRI in prostate cancer. *AJR. American Journal of Roentgenology*, *201*(6), 1229–1238. https://doi.org/10.2214/AJR.12.10178

Nagesh, S. V. S., Rana, R., Russ, M., Ionita, C. N., Bednarek, D. R., & Rudin, S. (2016). Focal Spot Deblurring for High Resolution Direct Conversion X-ray Detectors. *Proceedings of SPIE--the International Society for Optical Engineering*, *9783*. Retrieved on Jan. 22, 2020 from https://doi.org/10.1117/12.2216916

Nesterets, Y. I., Gureyev, T. E., Mayo, S. C., Stevenson, A. W., Thompson, D., Brown, J. M. C., Kitchen, M. J., Pavlov, K. M., Lockie, D., Brun, F., & Tromba, G. (2015). A feasibility study of X-ray phase-contrast mammographic tomography at the Imaging and Medical beamline of the Australian Synchrotron. *Journal of Synchrotron Radiation*, *22*(6), 1509–1523. https://doi.org/10.1107/S160057751501766X

Ng, A., & Swanevelder, J. (2011). Resolution in ultrasound imaging. *Continuing Education in Anaesthesia Critical Care & Pain*, *11*(5), 186–192. https://doi.org/10.1093/bjaceaccp/mkr030

Oh, W. K., Hurwitz, M., D'Amico, A. V., Richie, J. P., & Kantoff, P. W. (2003). *Biology of Prostate Cancer*. Holland-Frei Cancer Medicine-6th edition. Retrieved on Jan. 22, 2020 from https://www.ncbi.nlm.nih.gov/books/NBK13217/

Olivo, A., Rigon, L., Vinnicombe, S. J., Cheung, K. C., Ibison, M., & Speller, R. D. (2009). Phase contrast imaging of breast tumours with synchrotron radiation. *Applied Radiation and Isotopes, 67(6), 1033-1041*. https://doi.org/10.1016/j.apradiso.2009.01.075

Pagot, E., Fiedler, S., Cloetens, P., Bravin, A., Coan, P., Fezzaa, K., Baruchel, J., & Härtwig, J. (2005b). Quantitative comparison between two phase contrast techniques: Diffraction enhanced imaging and phase propagation imaging. *Physics in Medicine and Biology*, *50*(4), 709–724. https://doi.org/10.1088/0031-9155/50/4/010

Patel, N. D., & Parsons, J. K. (2014). Epidemiology and etiology of benign prostatic hyperplasia and bladder outlet obstruction. *Indian Journal of Urology : IJU : Journal of the Urological Society of India*, *30*(2), 170–176. https://doi.org/10.4103/0970-1591.126900

Pedler, K., Kitzing, Y. X. uan, Varol, C., & Arianayagam, M. (2015). The current status of MRI in prostate cancer. In *Australian family physician*, 44(4), 225–230.

Pisano, E. D., Johnston, R. E., Chapman, D., Geradts, J., Iacocca, M. V., Livasy, C. A., Washburn, D. B., Sayers, D. E., Zhong, Z., Kiss, M. Z., & Thomlinson, W. C. (2000). Human Breast Cancer Specimens: Diffraction-enhanced Imaging with Histologic Correlation—Improved Conspicuity of Lesion Detail Compared with Digital Radiography. *Radiology, 214(3), 895-901*. https://doi.org/10.1148/radiology.214.3.r00mr26895

Potts, J. M. (2001). The four categories of prostatitis: A practical approach to treatment. *Cleveland Clinic Journal of Medicine*, *68*(5), 389-390. https://doi.org/10.3949/ccjm.68.5.389

Rajaei, M., Momeni, A., Kheiri, S., & Ghaheri, H. (2013). Effect of ejaculation on serum prostate specific antigen level in screening and non-screening population. *Journal of Research in Medical Sciences : The Official Journal of Isfahan University of Medical Sciences*, *18*(5), 387–390.

Rasband, W. (2018). ImageJ (2018). Bethesda: NIH. Downloaded from https://imagej.nih.gov/ij/index.html

Reeth, E. V., Tham, I. W. K., Tan, C. H., & Poh, C. L. (2012). Super-resolution in magnetic resonance imaging: A review. *Concepts in Magnetic Resonance Part A*, *40A*(6), 307–308. https://doi.org/10.1002/cmr.a.21249

Roehrborn, C. G. (2008). Pathology of benign prostatic hyperplasia. *International Journal of Impotence Research*, *20*(S3), S11–S18. https://doi.org/10.1038/ijir.2008.55

Sala, E., Eberhardt, S. C., Akin, O., Moskowitz, C. S., Onyebuchi, C. N., Kuroiwa, K., Ishill, N., Zelefsky, M. J., Eastham, J. A., & Hricak, H. (2006). Endorectal MR Imaging before

Salvage Prostatectomy: Tumor Localization and Staging. *Radiology*, *238*(1), 176–183. https://doi.org/10.1148/radiol.2381052345

Sardana, G., & Diamandis, E. P. (2012). Biomarkers for the diagnosis of new and recurrent prostate cancer. *Biomarkers in Medicine*, *6*(5), 587–596. https://doi.org/10.2217/bmm.12.72

Schroder, F. H., Kruger, A. B., Rietbergen, J., Kranse, R., Maas, P. v. d., Beemsterboer, P., & Hoedemaeker, R. (1998). Evaluation of the Digital Rectal Examination as a Screening Test for Prostate Cancer. *JNCI Journal of the National Cancer Institute*, *90*(23), 1817–1823. https://doi.org/10.1093/jnci/90.23.1817

Scott, C., Allec, N., & Karim, K. (2012). A study of factors limiting spatial resolution using a 25 micron pixel pitch direct-detection amorphous selenium imaging system. *Proceedings of SPIE - The International Society for Optical Engineering*, *8313*, 83135Y-83135Y – 12. https://doi.org/10.1117/12.912429

Sershon, P. D., Barry, M. J., & Oesterling, J. E. (1994). Serum prostate-specific antigen discriminates weakly between men with benign prostatic hyperplasia and patients with organ-confined prostate cancer. *European Urology*, *25*(4), 281–287.

Sharifi, N., Gulley, J. L., & Dahut, W. L. (2005). Androgen Deprivation Therapy for Prostate Cancer. *JAMA*, *294*(2), 238-238. https://doi.org/10.1001/jama.294.2.238

Shenoy, G. (2003). Basic Characteristics of Synchrotron Radiation. *Structural Chemistry*, *14*(1), 3–14. https://doi.org/10.1023/A:1021656723964

Silzer, R. M., Berg, R., Bergstrom, J. C., Dallin, L., Shen, X., & Vogt, J. M. (2004). *Injection System for the Canadian Light Source*. EPAC Proceedings 2004, 2272-2274.

Slaoui, M., & Fiette, L. (2011). Histopathology Procedures: From Tissue Sampling to Histopathological Evaluation. *Methods in Molecular Biology (Clifton, N.J.)*, *691*, 69–82. https://doi.org/10.1007/978-1-60761-849-2_4

Smith, D. S., Catalona, W. J., & Herschman, J. D. (1996). Longitudinal screening for prostate cancer with prostate-specific antigen. *JAMA*, *276*(16), 1309–1315.

Smith-Bindman, R., Lipson, J., Marcus, R., Kim, K. P., Mahesh, M., Gould, R., de Gonzalez, A. B., & Miglioretti, D. L. (2009). Radiation Dose Associated with Common Computed Tomography Examinations and the Associated Lifetime Attributable Risk of Cancer.

Archives of Internal Medicine, *169*(22), 2078–2086. https://doi.org/10.1001/archinternmed.2009.427

Spajic, B., Eupic, H., Tomas, D., Stimac, G., Kruslin, B., & Kraus, O. (2007). The incidence of hyperechoic prostate cancer in transrectal ultrasound-guided biopsy specimens. *Urology*, *70*(4), 734–737. https://doi.org/10.1016/j.urology.2007.06.1092

Steinberg, G. D., Carter, B. S., Beaty, T. H., Childs, B., & Walsh, P. C. (1990). Family history and the risk of prostate cancer. *The Prostate*, *17*(4), 337–347. https://doi.org/10.1002/pros.2990170409

Stewart, B. W., & Wild, C. P. (n.d.). *World cancer report 2014*.

Taneja, S. S. (2004). Imaging in the diagnosis and management of prostate cancer. *Reviews in Urology*, *6*(3), 101–113.

Taqi, S. A., Sami, S. A., Sami, L. B., & Zaki, S. A. (2018). A review of artifacts in histopathology. *Journal of Oral and Maxillofacial Pathology : JOMFP*, *22*(2), 279-279. https://doi.org/10.4103/jomfp.JOMFP_125_15

Terasawa, M., & Kihara, M. (1996). Chapter 1 Basic characteristics of synchrotron radiation and its related facilities and instrumentation. *Analytical Spectroscopy Library*, *7*, 1–78. https://doi.org/10.1016/S0926-4345(96)80002-2

Thompson, I. M., Pauler, D. K., Goodman, P. J., Tangen, C. M., Lucia, M. S., Parnes, H. L., Minasian, L. M., Ford, L. G., Lippman, S. M., Crawford, E. D., Crowley, J. J., & Coltman, C. A. (2004). Prevalence of Prostate Cancer among Men with a Prostate-Specific Antigen Level ≤4.0 ng per Milliliter. *New England Journal of Medicine*, *350*(22), 2239–2246. https://doi.org/10.1056/NEJMoa031918

Thompson, J., Lawrentschuk, N., Frydenberg, M., Thompson, L., & Stricker, P. (2013). The role of magnetic resonance imaging in the diagnosis and management of prostate cancer. In *BJU International* 112(2), 6–20. https://doi.org/10.1111/bju.12381

Tole, N. M., Ostensen, H., World Health Organization, Department of Blood Safety and Clinical Technology, Team of Diagnostic Imaging and Laboratory Technology, World Health Organization, Department of Essential Health Technologies, World Health Organization, & Health Technology and Pharmaceuticals. (2005). *Basic physics of ultrasonographic imaging*. World Health Organization. Retrieved on Jan. 22, 2020 from " https://apps.who.int/iris/handle/10665/43179".

Truzzi, J. C. I., Almeida, F. M. R., Nunes, E. C., & Sadi, M. V. (2008). Residual Urinary Volume and Urinary Tract Infection—When are They Linked? *The Journal of Urology*, *180*(1), 182–185. https://doi.org/10.1016/j.juro.2008.03.044

Udeh, F. N. (1982). Structure and Architecture of the Prostatic Capsule. *International Urology and Nephrology*, *14*(1), 35–43.

Wasserman, N. F. (2006). Benign prostatic hyperplasia: A review and ultrasound classification. *Radiologic Clinics of North America*, *44*(5), 689–710, viii. https://doi.org/10.1016/j.rcl.2006.07.005

White, J. W. (1895). I. The Results of Double Castration in Hypertrophy of the Prostate. *Annals of Surgery*, *22*(1), 1–80.

Wiafe, Y. A., & Badu-Peprah, A. (2019). The Influence of Ultrasound Equipment Knobology in Abdominal Sonography. *Essentials of Abdominal Ultrasound*. Retrieved on Jan. 22, 2020 from https://doi.org/10.5772/intechopen.83713

Wiebe, S., Wysokinski, T. W., Belev, G., Miller, D., Webb, A., Zhu, N., Cooper, D., Izadifar, Z., Panahifar, A., Samadi, N., Martinson, M., Ford, N. L., Deman, P., Luan, X., Ianowski, J. P., Chen, D., & Chapman, D. (2015). Biomedical Imaging Using Synchrotron Radiation: Experience at the Biomedical Imaging and Therapy (BMIT) Facility at the Canadian Light Source. *Synchrotron Radiation News*, *28*(5), 16–23. https://doi.org/10.1080/08940886.2015.1080065

Wigle, D. T., Turner, M. C., Gomes, J., & Parent, M.-E. (2008). Role of hormonal and other factors in human prostate cancer. *Journal of Toxicology and Environmental Health. Part B, Critical Reviews*, *11*(3–4), 242–259. https://doi.org/10.1080/10937400701873548

Wolff, J. M., Borchers, H., Rohde, D., & Jakse, G. (1999). Age related changes of free and total prostate specific antigen in serum. *Anticancer Research*, *19*(4A), 2629–2632.

Wolkowski, B., Snead, E., Wesolowski, M., Singh, J., Pettitt, M., Chibbar, R., Melli, S., & Montgomery, J. (2015). Assessment of freeware programs for the reconstruction of tomography datasets obtained with a monochromatic synchrotron-based X-ray source. *Journal of Synchrotron Radiation*, *22*(4), 1130–1138. https://doi.org/10.1107/S1600577515008437

Zeller, J. L., Lynm, C., & Glass, R. M. (2007). Grading of Prostate Cancer. *JAMA*, *298*(13), 1596-1596. https://doi.org/10.1001/jama.298.13.1596

Zhang, K. Q., Salzman, S. A., Reding, D. J., Suarez, B. K., Catalona, W. J., & Burmester, J. K. (2003). Genetics of prostate cancer. *Clinical Medicine & Research, 1*(1), 21–28.

Zhao, Y., Brun, E., Coan, P., Huang, Z., Sztrokay, A., Diemoz, P. C., Liebhardt, S., Mittone, A., Gasilov, S., Miao, J., & Bravin, A. (2012). High-resolution, low-dose phase contrast X-ray tomography for 3D diagnosis of human breast cancers. *Proceedings of the National Academy of Sciences, 109(45), 18290-18294*. https://doi.org/10.1073/pnas.1204460109

9. Appendices

9.1.Appendix 1: Sample preparation and histology:

Before starting the histological preparations for our samples, the gelatin cylinder containing the TURP samples had to be taken out of each jar and sliced into small slices of approximately 3 mm thick (room temperature). It was critical to slice them exactly perpendicular to the length of the jar so that the slices would be in the same plane as the PC-CT and MRI images previously collected. For that, a metal slicing holder was specially designed and constructed (Figure 9.1; RMD Engineering Inc., Saskatoon, SK). It used metal fins to create slicing slits approximately 3 mm apart from one another that were used to guide the R35 type, microtome blades (Feather Safety Razor Co., Ltd Osaka, Japan) during slicing. Temporary plastic spacers were placed in each of those slits and the inner part of the slicer was wrapped with parafilm to prevent the liquid gelatin leaking out from the slicer once the liquid gelatin would be poured over the gelatin cylinder in the slicer (to positioning the gelatin cylinder firmly in the slicer cavity). The gelatin cylinder was placed inside the slicer with its length perpendicular to the slicing slits. At that time, the top and bottom ends of the gelatin cylinder in the slicer were noted down on outer surface of the slicer so that the top-bottom orientation of the gelatin cylinder wouldn't be missed.

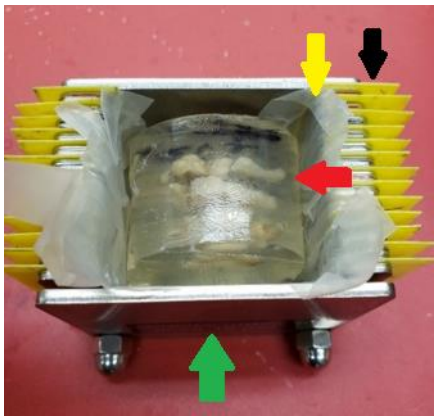

Figure 9.1 Metal slicer (green arrow) with yellow plastic spacers (black arrow), parafilm (yellow arrow) and the gelatin cylinder (red arrow) containing the TURP samples.

Fresh liquid gelatin was then poured into the slicer covering the whole gelatin cylinder. After solidifying, the entire gelatin block within the slicer and with the tissues at the centre was firm

enough for slicing. The plastic spacers were removed, and the microtome blade was used to cut the gelatin block into slices of ~3 mm (Figure 9.2).

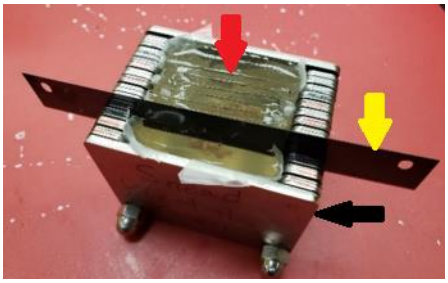

Figure 9.2 Slicing a gelatin block (red arrow) with microtome blade (yellow arrow) in metal slicer (black arrow)

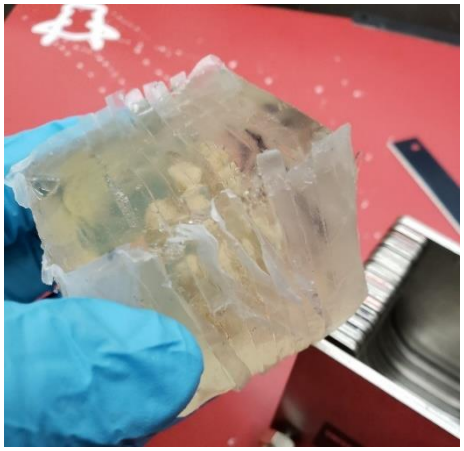

Figure 9.3 Sliced gelatin block taken out from the slicer.

The whole sliced block was taken out of the slicer as a single unit and each of the slices were kept in a row from top to bottom serially (Figure 9.4). The same procedure was followed for the rest of the gelatin blocks. Thirteen samples were cut into the ~ 3 mm slices and the remaining four (T1a, T3a, T6a, T9a; Table 4.1) were heavily lacerated and turned into useless pieces due to the liquefaction from the bacterial contamination. In this way, 36 slices were made from 13 samples.

Figure 9.4 Slices of a sample in a row from top to bottom serially.

The excess gelatin from all sides was trimmed as much as possible to allow the samples to fit into M490 – HISTOSETTE® I Tissue cassettes (Simport Scientific, Bernard-Pilon Beloeil, Quebec, Canada). Blue ink (Mrs. Stewart's® Liquid Laundry Bluing, Mrs. Stewart's Bluing Corp, Bloomington, Minnesota, USA) marking was done on the same surface and the same direction in all slices to keep the relative orientation of slices with each other and the original gelatin bock. The thickness of each slice was then measured with a Vernier scale (product name: Vernier Caliper, Plastic, # 1216Y22 by Thomas Scientific, Swedesboro, New Jersey, USA) by averaging the four thicknesses from four sides (Figure 9.5).

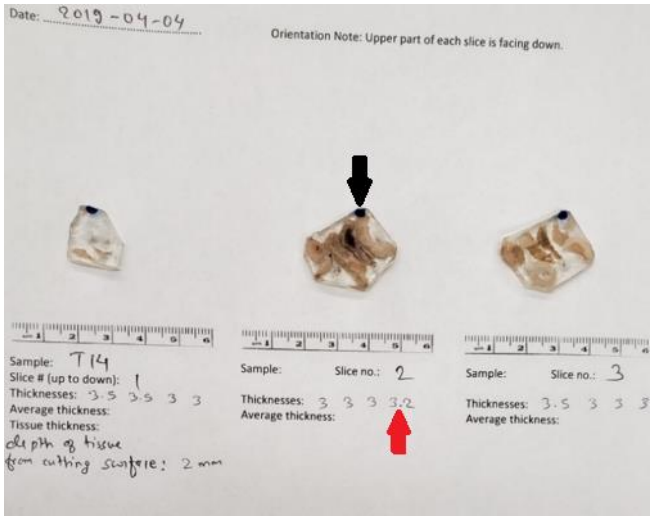

Figure 9.5 Ink marked slices (black arrow) in a serial order with their thicknesses in millimetres (red arrow).

After that, each slice was transferred into a separate histology cassette (M490 – HISTOSETTE® I, Simport Scientific, Bernard-Pilon Beloeil, Quebec, Canada) and each of them were labeled with

the sample number and slice number. The same procedure was applied for all samples. All the cassettes were kept in 10% buffered formalin and submitted to Prairie Diagnostic Services (PDS), University of Saskatchewan for paraffin embedding and creation of the blocks. Clear instructions to ensure the proper orientation of each slice into the paraffin block was also submitted in a written form to the PSD. Surgipath Paraplast® (Leica Biosystems, Wetzlar, Germany) was used for paraffin embedding/block creation which has a melting temperature of 56°C.

After receiving all 36 paraffin blocks from the 13 samples back from PDS, the rest of the procedures were conducted in the histology laboratory of the Department of Veterinary Biomedical Sciences in WCVM. It was decided to do serial microtome sectioning of the paraffin blocks and collect one section every 20 sections; each section was 5µm thick.

Sectioning was done with the a Microm® Microtome (ThermoFisher Scientific, Waltham, Massachusetts, U.S.). The gelatin in the paraffin blocks became very hard after all the histological processing and it was a challenge to section the blocks as the hard gelatin was cracking while sectioning. After multiple practices on trial samples a solution was found to overcome the problem. The blocks were cooled by placing into crushed ice and water (5-6 minutes) for cutting every 20 sections (i.e. to get one section as it was decided to collect one section out of every 20 sections cut). Another challenge was the wrinkles in the sections even after making the sections float in a warm water bath as usually adapted in regular histology procedure to prevent wrinkles. This was because of the difference in the rate of expansion of the tissue (at the center), gelatin (in between tissue and paraffin) and paraffin (outermost layer). After multiple trials, it was determined that using about a 15% ethanol solution at room temperature for floating the sections prior to floating them into a warm water bath of ~47°C reduces the wrinkles. After placing the sections onto glass slides and labeling them, they were kept on a warm plate (37°C) horizontally for at least 20 minutes to fix the tissues onto the slides. Then the slides were transferred to the slide rack, incubated (60°C, 60 min), and then removed and cooled to a room temperature for at least 30 minutes before staining. Different steps followed are summarized as follow:

1) Paraffin blocks were cooled by placing into crushed ice and water for cutting every 20 sections,

2) Sections were floated into 15% ethanol solution,

3) Floated again into a warm water bath of ~47°C,

4) Scooped the sections into glass slides,

5) Slides kept on a warm plate (37°C) horizontally for at least 20 minutes,

6) Slides were transferred to the slide rack and incubated at 60°C for 60 min,

7) Slides were removed form incubator and cooled to a room temperature.

Tissues were stained in hematoxylin and eosin (H&E; modified from Slaoui & Fiette, 2011) at room temperature with steps mentioned as below (Figure 9.6). A vertical slide rack (M90512DGY, Simport™ Scientific, Bernard-Pilon Beloeil, Quebec) was used to move slides containing the tissues from one solution to another.

Xylene 1 (Fisher Scientific, Fair Lawn, New Jersey, USA): 2 minutes

Xylene 2: 2 minutes

100% Ethanol (Greenfield Global Inc., Toronto, Canada): 2 minutes

100% Ethanol: 2 minutes

95% Ethanol: 2 minutes

95% Ethanol: 2 minutes

Running deionized water: 3 Minutes

Hematoxylin (SH26-4D, LOT 153233, Harris Modified, Fisher Chemical, Ottawa): 4 minutes

Running deionized water: 3 minutes

0.3% Acid alcohol (1 ml conc. HCL (Fisher Chemical) in 333.33 ml 70% alcohol): 30 seconds

Running deionized Water: 3 minutes

Eosin Y 1% Solution in water (SE23-500D, LOT 183228, Fisher Chemical, Ottawa): 4 minutes

Running deionized water: 30 seconds

95% Ethanol: 1 minute

95% Ethanol: 1 minute

100% Ethanol: 1 minute

Xylene 1: 1 minute

Xylene 2: 2 minutes

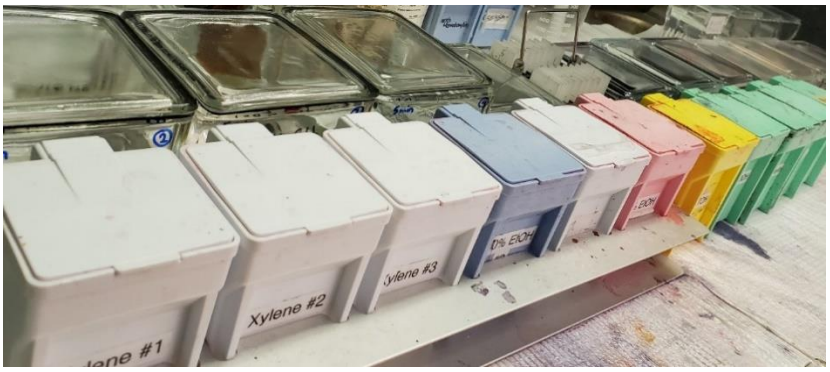

Figure 9.6. Staining jars in serial order.

Wet slides were then permanently mounted with Permount™ mounting medium (Fisher Chemical™, Pittsburgh, USA) by placing coverslip over it and stored horizontally to dry (Figure 9.7).

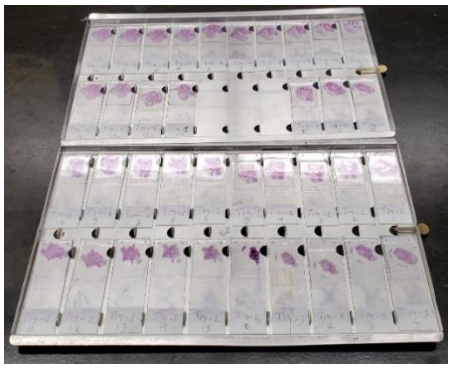

Figure 9.7 Mounted slides on a rack for drying.